4-2019

Scale Interactions within a Perturbed Plane Wall Jet

Shibani Bhatt

SCALE INTERACTIONS WITHIN A PERTURBED PLANE WALL JET

A Dissertation

Submitted to the Faculty

of

Embry-Riddle Aeronautical University

by

Shibani Bhatt

In Partial Fulfillment of the

Requirements for the Degree

of

Doctor of Philosophy in Aerospace Engineering

April 2019

Embry-Riddle Aeronautical University

Daytona Beach, Florida

“અસત્યો માંહે થી, પ્રભુ પરમ સત્યે તું લઈ જા,

ઊંડા અંધારે થી, પ્રભુ પરમ તેજે તું લઈ જા”

asatyō mānhē thī, prabhu parama satyē tuṁ laī jā,

ūṇḍā andhārē thī, prabhu parama tējē tuṁ laī jā

“From the heart of untruths, bring me to the absolute truth,

From the depths of darkness, bring me to the absolute light”

***

To my mother, father, sister and brother,

without whom this would not have been possible.

SCALE INTERACTIONS WITHIN A PERTURBED PLANE WALL JET

by

Shibani Bhatt

This dissertation was prepared under the direction of the candidate's committee chairman, Dr. Ebenezer Gnanamanickam, Department of Aerospace Engineering, and has been approved by the members of the dissertation committee. It was submitted to the College of Engineering and was accepted in partial fulfillment of the requirements for the

Degree of

Doctor of Philosophy in Aerospace Engineering

DISSERTATION COMMITTEE

Chairman, Dr. Ebenezer Gnanamanickam

Member, Dr. William Engblom

Member, Dr. J. Gordon Leishman

Member, Dr. Reda Mankbadi

Department Chair, Dr. Anastasios Lyrintzis
or Graduate Program Coordinator, Dr. Marwan Al-Haik

04/16/2019
Date

Dean of College of Engineering, Dr. Maj Mirmirani
or Associate Dean, Dr. Yi Zhao

04/16/2019
Date

Senior Vice President for Academic Affairs
and Provost, Lon D. Moeller, J.D.

4/17/19
Date

ACKNOWLEDGMENTS

It has been a long journey reaching this point and I wouldn't have accomplished it without a lot of people. I would like to acknowledge the role they have played in helping me finish my PhD. First, I would like to thank my advisor, Dr. Ebenezer Gnanamanickam, for his guidance and support throughout my graduate studies. I greatly appreciate the time and effort he has taken to enhance my caliber. I would like to thank my committee member, Dr. J. Gordon Leishman, for his guidance and comments on my dissertation. I'm grateful to Dr. Reda Mankbadi for his assistance throughout my stay at Embry-Riddle. I would like to thank Dr. William Engblom for his feedback on my work. I appreciate the direction and comments the department chair, Dr. Tasos Lyrintzis, gave me at every step along the way. I would like to thank Dr. Tej Gupta for believing in me. His encouragement enabled me to push through difficult situations throughout the course of my PhD.

I would like to thank Dr. Zheng Zhang for his help with the flow visualization of the plane wall jet. I want to express my gratitude to Mr. Mike Potash, Mr. William Russo and Mr. Darrel Stevens for their help and technical support at various aspects of this project. I would like to thank Ms. Cynethia Goodwyn and Dr. Pamela Daniels for taking care of all the administrative work that went behind this project. I would like to recognize my colleagues Sravan Artham, Adam Thames and Pratik Deshpande for having critical discussions on the project and sharing ideas with me.

I would like to acknowledge my roommate Bharvi Chhaya for providing her help and support during the course of my stay here. I would like to thank my friend Dr. Purvi Zaveri for her support and guidance during my PhD. I am grateful to all my friends who listened to my venting and provided a shoulder for me during difficult times.

Lastly, I would like to thank my family for their immense love and support without which I wouldn't be the person that I am today.

TABLE OF CONTENTS

LIST OF TABLES

LIST OF FIGURES

Figure Page

Figure Page

Figure Page

Figure Page

Figure Page

Figure Page

Figure Page

Figure Page

SYMBOLS

C_{f_j}	Skin friction coefficient based on the PWJ exit velocity
E_L	Large-scale component of the Hilbert transform of the small-scale velocity component
M_j	PWJ momentum
M_0	PWJ total momentum
M_r	PWJ momentum at some reference upstream location
M_τ	Momentum loss due to friction
Re_τ	Friction Reynolds number
Re_j	Reynolds number based on the PWJ exit conditions
Re_m	Reynolds number based on outer scales
Re_θ	Reynolds number based on momentum thickness
R_{AM}	Amplitude modulation correlation coefficient
St	Strouhal number
T	Sampling time
$\overline{U}$	Mean effective velocity
U_f	Phase averaged velocity per forcing cycle
U_L	Large-scale component of the effective velocity
U_m	Maximum mean velocity
U_s	Small-scale component of the effective velocity
U_τ	Mean friction velocity
V_j	PWJ exit velocity
V_{pp}	Peak to peak voltage
b	PWJ exit height
d	Hot-wire diameter
f	Frequency of the effective fluctuations in the flow
f_f	Forcing frequency
f_s	Sampling frequency

f_{HW}	Hot-wire resonance frequency
f_c	Estimate of the highest frequency present in the flow
k_x	Streamwise wave-number
l	Length of the hot-wire sensing element
u	Streamwise velocity component
u_L	Large-scale component of the streamwise velocity
u_s	Small-scale component of the streamwise velocity
w	Wall-normal velocity component
x	Streamwise distance
z	Wall-normal distance
z_m	Wall-normal location where $\overline{U} = U_m$
$z_{m/2}$	Outer length scale of the PWJ (also denoted as δ)
z_0	Measurement location closest to the wall considered for U_τ calculation
ΔU_τ	Reduction in U_τ upon forcing
γ	Inclination angle of the ramp-like structures in boundary layers
δ	Boundary layer thickness/Outer length scale
θ_f	Periodic phase of the forcing signal
λ_j	Forcing wavelength non-dimensionalized with respect to PWJ exit conditions
λ_x	Streamwise wavelength
λ_{xi}	Streamwise wavelengths of the naturally energetic large-scales in the inner region
λ_{xo}	Streamwise wavelengths of the naturally energetic large-scales in the outer region
μ	Dynamic viscosity
ν	Kinematic viscosity
τ_w	Wall shear-stress
τ_{uw}	Reynolds stress

ϕ_{uu}	Energy spectrum

Supercripts

$+$	Non-dimensionalization with respect to the viscous quantities
$\prime$	Corresponding fluctuating component of the velocity
0	Unforced quantities
$*$	Forced quantities
n	Naturally existing energetic scales of the flow
f	Scales corresponding to the forcing scales
r	Recipient scales of the forcing energy

ABSTRACT

Bhatt, Shibani, Ph.D., Embry-Riddle Aeronautical University, April 2019. Scale interactions within a perturbed plane wall jet.

The current work focuses on exploiting this behavior to manipulate wall turbulence by targeting the large-scales of the flow. In wall turbulence the large-scales of the flow interact with the smaller scales in a non-linear manner including through a process of amplitude and frequency modulation. A plane wall jet (PWJ) is chosen as the model flow field for this work as its unique geometry allows for the controlled introduction of large-scale perturbations through acoustic forcing. The corresponding interactions because of forcing are characterized using single hot-wire measurements. The near-wall response of the PWJ over a range of large-scale forcing showed that the friction velocity U_τ decreased for all forcing wavelengths considered. The scaling behavior of this reduction in U_τ with respect to inner, outer and global (PWJ exit conditions) variables suggested that the responsible underlying mechanism was an inner-outer interaction with a dependence on the PWJ Reynolds number. Based on this near-wall study, a more detailed study of the interactions caused by forcing was carried out focusing on three specific wavelengths. The forcing was observed to increase the spreading rate of the PWJ while reducing the maximum streamwise mean velocity. Together, this resulted in an increase in the friction Reynolds number Re_τ upon forcing, as well as a transfer of momentum away from the inner (wall) region to the outer free-shear region. The linear response of the flow to the forcing resulted in the introduction of distinct periodic structures into the inner and outer regions of the flow that appear to convect at different velocities. Considering the non-linear response, an increase in the turbulence intensity in the wall region of the PWJ was observed. The forcing altered the energy of the large-scales of the flow as well as its distribution across wavelengths. This redistribution of energy was seen to occur in the manner of a forward cascade as well as an inverse cascade. The direction of transfer depends on

the size of the forcing scales relative to the naturally energetic large-scales of the flow. It was observed the that primary recipient scales of the flow were flow structures that matched the energetic outer free-shear layer structures. However, it was also observed that these structures are transported closer to the wall, increasing the energy in the wall region. This effect is accompanied by the reduction of small-scale energy in the wall region, which is inferred to be tied to the reduction of friction velocity upon forcing. The increase in energy of the large-scales of the flow was also accompanied by the increased amplitude modulation of the small-scales by the large-scales. It is concluded that the forcing successfully targets the large-scales of the PWJ, which changes the non-linear interaction between the scales in a manner that reduces the skin-friction.

1. Introduction

Turbulent flows are ubiquitous in nature as well as in engineering applications. They are encountered in a comforting sense when creamer mixes with coffee, or in a discomforting sense when 'turbulence' occurs during flight, or in an outright obnoxious form as in hurricanes. Turbulent flows are often seen in the vicinity of a solid boundary and are referred to as turbulent boundary layers. Within a turbulent boundary layer, turbulence arises as a consequence of the viscosity and the shear stress in the fluid. The shear stress at the wall is defined as

$$\tau_w = \mu \left(\frac{d\overline{U}}{dz} \right)_{z=0} . \tag{1.1}$$

Where, μ is the dynamic viscosity, $\overline{U}$ is mean velocity and z is wall-normal distance. The integration of the wall shear stress over the wetted surface area results in the friction drag of the body. Hence, the viscosity is also responsible for the production of skin friction drag on a surface over which the boundary layer flows. Skin friction drag is an important quantity with significant economic impact. For example, commercial aircraft expend significant engine power in overcoming skin friction drag as it accounts for about 50% of the total drag at cruise (Ganapathisubramani et al., 2005; Stenzel et al., 2011; Filippone, 2000). In 2018, commercial air carriers consumed over 17,000 million gallons of fuel at $2.15 per gallon (BTS, 2019). If fuel consumption

was reduced even by 1%, more than \$384M per year can be saved in fuel cost for commercial carriers alone.

A majority of flows, whether they be naturally occurring or consciously engineered, comprise turbulent boundary layers at high Reynolds numbers. A commonly used Reynolds number in turbulent boundary layer studies is

$$Re_\tau = \frac{U_\tau \delta}{\nu} \tag{1.2}$$

where, $U_\tau = \sqrt{\tau_w/\rho}$ is the friction velocity, τ_w is the wall shear stress, ρ is the fluid density, δ is the outer length scale and ν is the kinematic viscosity. Within a turbulent boundary layer, the small-scales of the flow are of the order $\mathcal{O}(\nu/U_\tau)$ (where ν/U_τ is known as the viscous length scale) and the large-scales of the flow are of the order $\mathcal{O}(\delta)$ (Adrian, 2007). Hence, Re_τ can also be written as

$$Re_\tau = \frac{\delta}{\nu/U_\tau} = \delta^+ \equiv \frac{\text{largest scales}}{\text{smallest scales}}. \tag{1.3}$$

In this dissertation, the '+' superscript indicates non-dimensionalization with respect to viscous scales.

In general, an increase in Re_τ causes the viscous scales to become smaller while the large-scales get larger. As a vast majority of flows of interest are at higher Reynolds numbers this trend in relative scale size with increasing Re_τ, creates engineering challenges from a flow control perspective. Traditionally, the target scales of flow control have been the smaller scales of the near-wall cycle. Hence, with increasing Re_τ

the physical dimensions of sensors and actuator required for controlling the smaller scales become smaller while the required frequency response increases.

For example considering an aircraft flying at cruise conditions, the viscous scale is of the order $\mathcal{O}(1\mu m)$ (Talluru, 2014). This scale requires sensors and actuators with dimensions of the order $\mathcal{O}(50\mu m)$ (Talluru, 2014). Practically this would require 2×10^5 sensors (or actuators) on a Boeing 737 flying at Mach 0.77 (Wilkinson, 1990) with frequency response of the order $\mathcal{O}(100kHz)$ (Kasagi et al., 2009).

Recent studies have shown that the outer large-scales are not independent of the near-wall small-scales (Hutchins and Marusic, 2007b; Marusic et al., 2010; Klewicki, 2010; Smits et al., 2011; Hutchins et al., 2011; Ganapathisubramani et al., 2012; Hutchins et al., 2012; Jacobi and McKeon, 2013; Duvvuri and McKeon, 2014; Vallikivi et al., 2015; Dogan et al., 2016; McKeon, 2017; Marusic et al., 2017; McKeon et al., 2018; Jiménez, 2018). They interact in two ways:

1. The large-scales away from the wall superimpose themselves on the near-wall small-scales of the near-wall cycle and

2. The outer large-scales amplitude modulate (AM) and frequency modulate (FM) the near-wall small-scales.

This non-linear interaction (AM and FM) provides a mechanism to target the small-scales using the large-scales of the flow. This mechanism is the focus of the present work. The advantage of targeting the large-scales of the flow is that it requires sensors and actuators of a physical size that is technologically feasible ($\mathcal{O}(\delta)$) from

an engineering standpoint. The required frequency response of such sensors is also lower.

Due to the increasing energy of the large-scales with increasing Reynolds number, the large-scales significantly contribute towards the turbulent production at high Re_τ (Smits et al., 2011; Jiménez, 2018). This outcome has significance with respect to the current model flow field–the plane wall jet (PWJ). A plane wall jet (PWJ) is a laboratory shear layer which has energetic large-scale structures at short development lengths. In addition, the structures of the PWJ allows for the controlled introduction of large-scale perturbations into the flow. This approach allows for the systematic characterization of the non-linear energy transfer mechanism within a PWJ and the associated scale interactions. For these reasons, a PWJ has been chosen as the model flow field for the present work.

1.1 Plane Wall Jet

A plane wall jet (PWJ) is a shear flow driven by a high momentum flow stream exiting from a slot and developing in the vicinity of a wall (see Figure 1.1 and 1.2). A PWJ resembles a free-shear flow in the outer region and a conventional boundary layer in the near-wall region. These two shear layers interact with each other as they develop downstream resulting in a single interacting flow (see Figure 1.1).

Figure 1.2 shows a schematic of the PWJ shear layer. The mean streamwise velocity $\overline{U}$ within a typical wall jet reaches a maximum U_m at some wall-normal location z_m, and asymptotically approaches zero in the quiescent environment away

from the wall. The outer shear layer thickness for a PWJ is defined as the wall-normal distance δ (also denoted by $z_{m/2}$), in the outer free shear layer, at which the mean velocity is half that of U_m. The outer velocity scale of the PWJ is U_m and the outer length scale is δ. For the remainder of the present work, the PWJ exit velocity V_j and height b are referred to as the global variables. As per boundary layer convention, the friction velocity U_τ and the viscous length scale ν/U_τ are the inner scales.

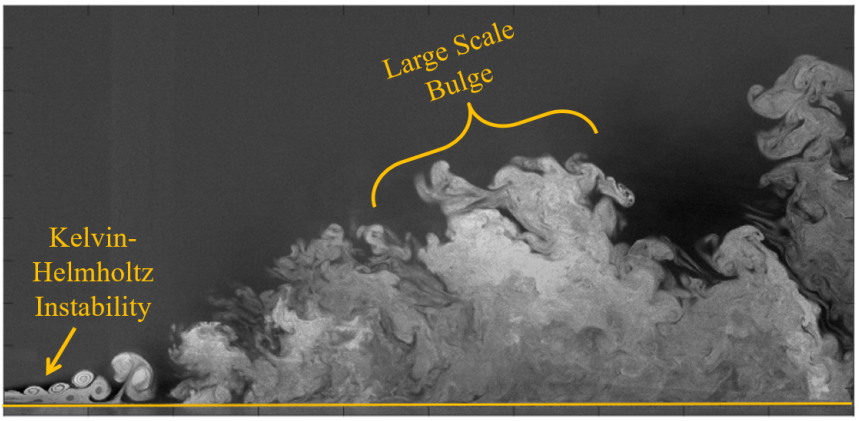

Figure 1.1. A still shot of a PWJ shear layer showing the formation and evolution of the Kelvin-Helmholtz instability (Gnanamanickam et al., 2017).

1.2 Objective

The objectives of the current work are to introduce energetic large-scale perturbations into a PWJ and study the resulting non-linear interactions. These interactions are characterized in terms of the relevant scales of the problem and the friction velocity. The spectra of the forced and unforced flow are then used to describe the energy transfer mechanism within the PWJ and the associated scale interactions.

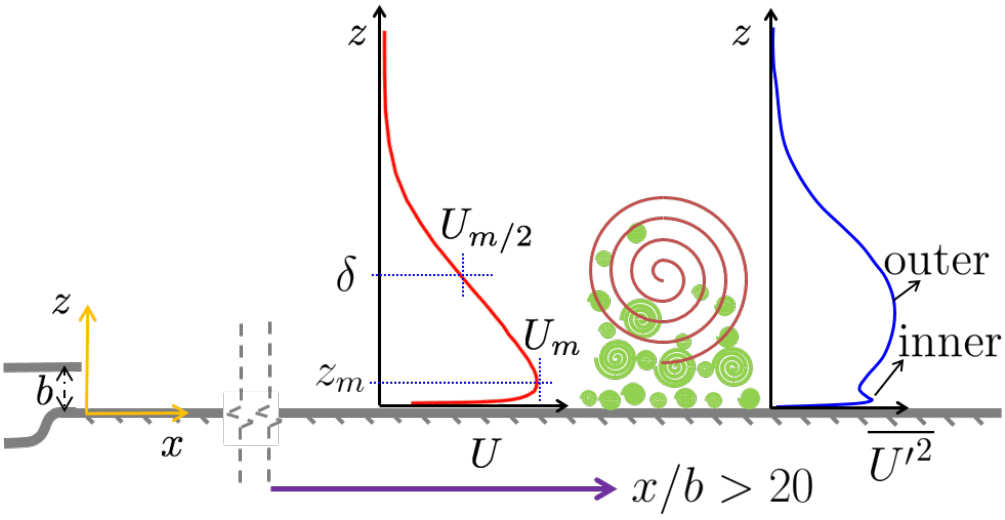

Figure 1.2. Schematic of a PWJ shear layer. Here, x and z denote streamwise and wall-normal directions respectively, b the jet exit height, $\overline{U}$ the mean total velocity and U' the velocity perturbation.

1.3 Dissertation Outline

Following this chapter (Chapter 2) is a summary of relevant literature pertinent to the proposed work. Chapter 2 provides a synopsis of studies related to coherent structures in canonical boundary layers highlighting the types of coherent structures present in high Reynolds number flows and the embedded non-linear interactions. A brief discussion on prior studies of the PWJ, as well as the relevance of the PWJ to canonical boundary layers, are also provided. Chapter 3 documents the details of the PWJ experimental facility and discusses the instruments and sensors used to conduct experiments. The approach followed for calculating the friction velocity U_τ is also discussed in this chapter.

Chapter 4 discusses the near-wall response of the PWJ to a range of forcing wavelengths. The reduction of friction velocity ΔU_τ as a function of forcing wavelength

is analyzed. Scaling of ΔU_τ with respect to inner, outer and global variables is also presented here. This chapter forms the basis for the forcing wavelengths chosen for a more detailed analyses of the forced PWJ presented in subsequent chapters. Chapter 5 compares the mean turbulence statistics for the unforced and forced flows at the three chosen wavelengths. In this chapter, the mean velocity and turbulence intensity profiles for the unforced and forced flows are compared. The reduction in skin friction coefficient C_{f_j} and the change in momentum of the flow due to forcing is discussed. The linear response of the PWJ to the forcing is also presented.

Chapter 6 compares the spectral analysis of the unforced and forced flows. The presence of an energy transfer mechanism in the manner of a forward and an inverse cascade is discussed in this chapter. A detailed discussion regarding the energy transfer between scales is presented. Chapter 7 discusses the non-linear interactions between the large-scales and the small-scales of the flow as quantified using the amplitude modulation coefficient.

Chapter 8 concludes the present study summarizing key conclusions from Chapters 4 to 7. This chapter also includes suggestions for future work.

2. Background and Literature Review

This chapter provides a review of the scales of motion within a turbulent boundary layer and the embedded interactions between the large-scales and small-scales therein. This review is followed by a further review of the model flow field PWJ, along with its relevance to conventional boundary layers. The review is organized into the following these sections:

1. Coherent structures within turbulent boundary layers.
2. High Reynolds number effects.
3. Plane wall jet.

It is noted that the work presented here only cites prior observations pertinent to the current research. Much of the cited work also contains a comprehensive summary of wall-bounded flows.

2.1 Coherent Structures in Turbulent Boundary Layers

Coherent structures in a turbulent flow are recurrent structures that continue to exist over large eddy-turn-over times (Davidson, 2015). Within turbulent wall-bounded flows, these coherent motions are responsible for transporting momentum and producing turbulent kinetic energy. Understanding the characteristics and behavior of these structures, despite significant progress, is still a focus of current research. The coherent motions in a turbulent boundary layer are often characterized based

on their wall normal location. Figure 2.1 shows the different regions of a turbulent

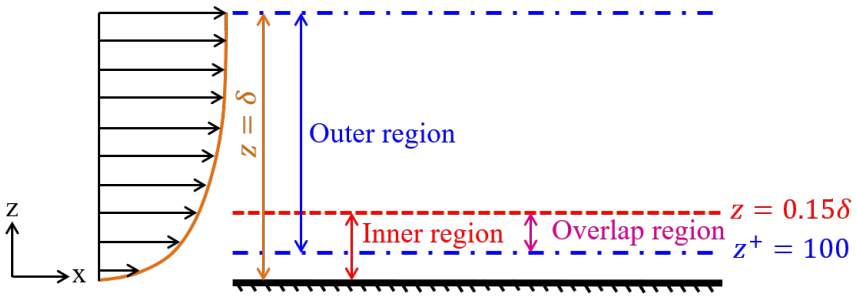

Figure 2.1. Illustration of different regions within a zero pressure gradient turbulent boundary layer (ZPGTBL) adapted from Kline et al. (1967); Gad-el Hak and Bandyopadhyay (1994). Here, δ is the boundary layer thickness.

boundary layer. The inner layer is broadly referred to as the near-wall region where $z^+ \lessapprox 100$ (Hutchins and Marusic, 2007b). The outer region (also known as the wake region) is defined as the wall-normal distance where $0.15\delta^+ < z^+ < \delta^+$ (Hutchins and Marusic, 2007b). The overlap region is the region $100 < z^+ < 0.15\delta^+$ (Hutchins and Marusic, 2007b), which is where the inner and the outer region profile is matched in the limit of infinite Reynolds number (Francis, 1954). The velocity profile within a turbulent boundary layer follows a linear equation in this region when plotted in log coordinates. Hence, this region is also called the logarithmic region of the boundary layer. Hutchins and Marusic (2007b) have shown that for the existence of a clear overlap region, the Reynolds number must be $Re_\tau \gtrsim 1700$. In other words, only sufficiently large scale separation would lead to a distinct logarithmic region in the boundary layer.

A more useful characterization of flow structures is summarized in the reviews by Smits et al. (2011) and Klewicki (2010), which broadly characterizes the flow structures within a turbulent boundary layer as:

(a) The near-wall small-scale structures part of the near-wall cycle $\left(\lambda_x^+ < 1000\right)$ (Lee and Moser, 2019)

(b) Large scale motions (LSM) $(\lambda_x = \mathcal{O}(\delta))$ and Very Large Scale Motions (VLSM) $(\lambda_x = \mathcal{O}(10\delta))$ (Klewicki, 2010)

Notice that, λ_x is the streamwise wavelength of the streamwise fluctuations.

2.1.1 Near-Wall Cycle

The near-wall cycle is a self-sustaining process (SSP) that comprises of three key events (Panton, 2001). First is the formation of streamwise low velocity streaks through streamwise rolls, which are structures that are responsible for the creation of streamwise vorticity. Second is the instability of the streaky structures which leads to breakdown of the streamwise rolls. Finally, there is regeneration of the streamwise rolls by receiving energy from the instabilities in the previous events. This cycle is illustrated in Figure 2.2(a), which shows each intermediate stage of the near-wall structures and the process that leads to their breakdown and regeneration.

This type of cycle was first visualized by Kline et al. (1967) in the form of streamwise velocity streaks. These streaks were found to reorganize in the streamwise direction as a collection of low speed fluid. Kline et al. (1967) observed that these

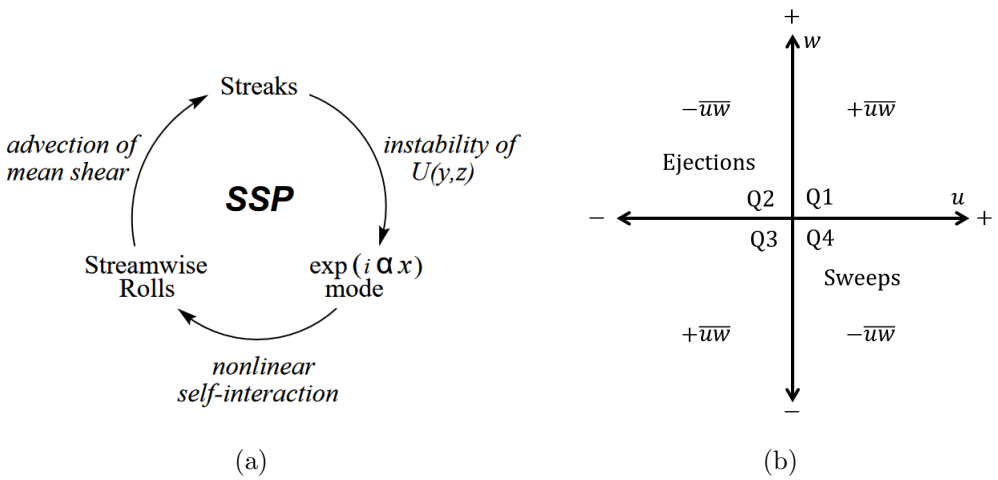

(a) (b)

Figure 2.2. (a) Schematic of the self-sustaining process (SSP) of the near-wall cycle. Taken from Waleffe and Kim (1998). (b) Illustration of the quadrant events based on streamwise velocity fluctuation u and wall-normal velocity fluctuation w as given by Lu and Willmarth (1973).

low-speed structures would then move away from the wall and oscillate before breaking up. Similarly, Rao et al. (1971) observed periodically increased turbulence activity through hot-wire measurements, which they then identified as ''bursts". They related this phenomenon to Batchelor et al.'s (1949) small-scale intermittency and Landau & Kolmogorov's (1962) "spottiness".

Wallace et al. (1972) and Lu and Willmarth (1973) identified insightful information associated with the signs of the velocity components, which led to the quadrant-based analyses in the Reynolds shear stress plane. Wallace et al. (1972) analyzed streamwise and wall-normal velocity fluctuations through an array of hot films in the near-wall region. Wallace et al. observed the variation in the Reynolds stress ($\tau_{uw} = -\overline{uw}$ here, u and w are streamwise and wall-normal velocity components respectively) and found that negative u and positive w ($-\overline{uw}$) events caused slower fluid to move away

from the wall, referred to as an "ejection" event. The component of Reynolds stress resulting from the positive u and negative w ($-\overline{uw}$) event was called a "sweep" event, where high speed fluid moved towards the wall. Wallace et al. observed that as a part of the near-wall cycle, several different ejection events group together to form a "burst", which forms the low velocity streak depicted in Figure 2.2(a). The "bursting process" then ends with a sweep. Wallace et al. observed that at $z^+ = 15$, both sweeps and ejections contributed equally towards the Reynolds stresses. Below that, sweeps were dominant, whereas above that, ejections were dominant.

Lu and Willmarth (1973) used an x-wire probe to analyze the Reynolds stress near the wall and reached a similar conclusion. They also interpreted the results in terms of quadrant (Q) events. Figure 2.2(b) shows a schematic describing these quadrant events. They observed that both ejection (Q2) and sweep (Q4) events had identical convection velocities and occurred at approximately equal time intervals. They concluded that the highest contribution towards τ_{uw} came from ejections followed by sweeps. Following this, a number of studies have concluded that ejection and sweep events dominate momentum transport and turbulent kinetic energy dissipation in wall-bounded flows (Lozano-Durán et al., 2012; Adrian et al., 2000; Panton, 2001).

A significant amount of understanding of coherent motions within turbulent boundary layers has been derived from relatively low Reynolds number studies, because of either challenges in conducting high Reynolds number measurements and computations, or the desire to specifically study the near-wall cycle. At low Reynolds numbers over large development lengths, the boundary layer has a physically thick inner layer,

which makes it an ideal candidate for studying the near-wall region and the embedded viscous effects. In-depth reviews focusing on the near-wall cycle can be found in the works of Jiménez (1991; 1994; 1999), Schoppa (1997; 1997; 2002) and Waleffe (1998; 1995; 2001). A comprehensive summary of their work is given by Panton (2001).

An important observation as summarized by Panton (2001), particularly relevant to the current work, should be noted here. Panton concluded that at low Reynolds numbers, near-wall instabilities can exist without an outer layer. However, the influence of the outer layer on the periodically appearing instability mechanism in the near-wall cycle was an open ended question. In this regard, a majority of researchers favored confinement within the inner layer or in other words, an autonomous near-wall cycle. In particular, the work of Jiménez and Pinelli (1999) presents the view that the near-wall cycle is autonomous and does not require any triggers from the outer larger scales. The behavior of the near-wall cycle at high Reynolds number, however, was mostly speculative.

In the last two decades, advances through higher Reynolds number studies have indicated an influence of the large-scales on the near-wall scales, which will be elaborated upon in §2.2. This research has led to a refined view of the near-wall cycle. While perhaps not being dependent on external triggers, it at least coexists with the substantial superimposed energy from the outer large-scales as Reynolds number increases (Marusic et al., 2017).

Studies during the 1990s focusing on the near-wall cycle started establishing the relationship between the near-wall cycle and outer structures. In particular, the work

of Zhou et al. (1999), Kim and Adrian (1999) and Adrian et al. (2000) proposed a composite view of the vortical structures associated with the aforementioned quadrant events. These vortical structures are broadly referred to as "hairpin" vortices.

2.1.2 Hairpin Vortices

A hairpin vortex is a hairpin shaped vortex typically attached to the wall. Shown in Figure 2.3 is the most common form of the hairpin structure visualized in a turbulent boundary layer (Klewicki, 2010). Many earlier experimental studies observed these structures at different phases of their life cycle, and these structures were described using different shapes and terminology. A comprehensive summary of these earlier observations can be found in the work of Robinson et al. (1989).

A detailed characterization of hairpin vortices is shown in Figure 2.3 (as proposed by Adrian et al. (2000)). The figure illustrates the characteristics of a typical hairpin vortex attached to the wall. This distinct characteristics of a hairpin vortex include (Adrian et al., 2000):

(a) A head of a spanwise vortex core.

(b) Necks that are wall-normal extensions upstream of the head at an angle with the streamwise direction.

(c) Streamwise oriented legs attached to the wall.

Figure 2.3 also highlights the occurrence of quadrant based events and the relative velocities within the hairpin vortex.

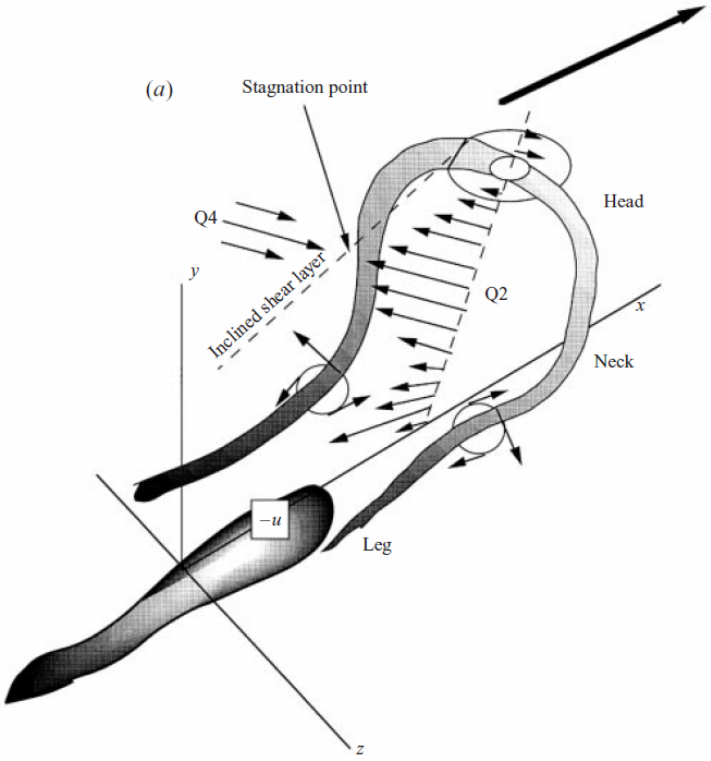

Figure 2.3. Illustration of a single hairpin vortex attached to the wall. Arrows represent the velocity direction and the color gradient represents velocity magnitude within the vortex (velocity increases towards the lighter shade). Taken from Adrian et al. (2000).

One of the key observations from earlier studies has by Head and Bandyopadhyay (1981). They observed a zero pressure gradient boundary layer over a range of Reynolds numbers ($500 < Re_\theta < 17500$, Re_θ is the Reynolds number based on momentum thickness) by illuminating smoke using a sheet of light. They observed that for $Re_\theta < 500$, there was no clear distinction between the small-scales and large-scales. The hairpin vortices were shaped like a single vortex loop or a horseshoe. At higher Reynolds numbers ($Re_\theta > 2000$), the flow structures became stretched in the streamwise direction and formed elongated hairpin vortices inclined at a 45°

angle to the wall. They observed that the spanwise dimension of the vortex scaled with inner variables while extending all the way to the outer region of the boundary layer. This outcome suggested that the physical dimension of coherent structures in the boundary layer depended on the Reynolds number. They proposed that at high Reynolds number, the heads of the hairpin vortices align together to form a smaller angle (about 20°) with the streamwise direction than the characteristic angle of the hairpins (i.e. 45°).

Adrian et al. (2000) analyzed a zero pressure gradient boundary layer across a range of Reynolds numbers ($930 < Re_{\theta} < 6845$) using high resolution Particle Image Velocimetry (PIV). It was observed that the instantaneous velocity fields were densely populated with hairpin vortices, and identified hairpin vortex heads above strong ejection events. The neck of these vortices were inclined at an angle that varied from $30 - 60^{\circ}$ to the wall. They observed that the individual hairpins aligned in the streamwise directions to form packets. These packets extended up to 0.8δ in the wall-normal direction and 2δ in the streamwise direction. They noticed that the hairpin packets formed a growing ramp-like structure which became more frequent at high Reynolds numbers. They also observed that the new hairpin packets formed within the primary (or oldest) hairpin packet, creating a hierarchy of scales. Such a nested flow structure caused zones of uniform momentum inclined at an angle to the streamwise direction.

Based on their observations and Zhou et al.'s (1999) direct numerical simulations (DNS), Adrian et al. (2000) proposed a structural model to represent the coherent mo-

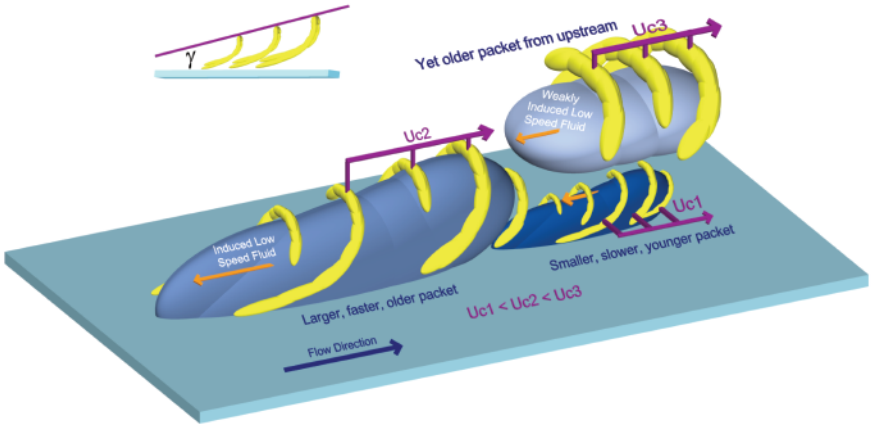

Figure 2.4. Structural model highlighting the hierarchy of hairpin packets attached to the wall, proposed by Adrian et al. (2000). Taken from Adrian (2007).

tions within the turbulent boundary layers at high Reynolds number. The schematic of this hairpin packet paradigm is shown in Figure 2.4. They identified the inclination angle of the ramp-like structures as γ and found it to vary between $3 - 35^{\circ}$ with a mean angle of 12°. They proposed a model of nested hairpin packets with older, faster and larger packets over the smaller and younger packets. They concluded that the heads of the larger hairpins span all the way to the edge of the boundary layer and are responsible for causing large-scale bulging. This large-scale bulging is indicative of large scale motions (LSMs) in the boundary layer (Falco, 1977; Smits et al., 2011).

Concluding this section on the features of the coherent motions in the wall-bounded flows, three key observations should be reiterated. First, coherent structures are inclined at an angle to the streamwise direction. Second, they form nested packets of vortices with a range of scales. Finally, they convect creating uniform zones

of low and high momentum, which are also inclined to the wall. Using these key observations, large scale motions within a turbulent boundary layer can be identified.

2.1.3 Large Scale Motions (LSMs) and Very Large Scale Motions (VLSMs)

Studies over the last two decades have revealed universally the existence of LSMs ($2-3\delta$), VLSMs ($>10\delta$) and superstructures ($\sim 6\delta$) in canonical boundary layers (Monty et al., 2009; Klewicki, 2010; Smits et al., 2011; Baars et al., 2017b; Jiménez, 2018). Superstructures are typically seen in zero pressure gradient boundary layer, whereas VLSMs are seen in internal flows.

At high Reynolds numbers, these structures are particularly found to populate the logarithmic region, with LSMs and VLSMs extending up to the wake region of boundary layers (Baars et al., 2017a; Hutchins and Marusic, 2007a; Monty et al., 2009; Vallikivi et al., 2015; Dogan et al., 2016; Jiménez, 2018). These large-scale structures make significant contributions towards the turbulent kinetic energy and Reynolds stress production at high Reynolds number, (Ganapathisubramani et al., 2003; Guala et al., 2006; Balakumar and Adrian, 2007; Klewicki, 2010; Lozano-Durán et al., 2012; Marusic et al., 2010) as well as becoming dynamically more important (Smits et al., 2011; Baars et al., 2017a; Jiménez, 2018).

LSMs were first identified in turbulent boundary layers half a century ago. Falco (1977) characterized LSM in the outer region of the turbulent boundary layer through simultaneous hot-wire measurements and flow visualization. Falco identified LSM of the order of 1.6δ as high concentrations of smoke in the bulges of fluid in the outer

region of the boundary layer. Falco also observed a rare event in the log region between two LSMs which he referred to as "superbursts". Falco observed that the "superbursts" grew into new LSMs downstream. Inclined hairpin vortices aligned with the heads of the vortices at an angle to the wall was distinctly observed by Head and Bandyopadhyay (1981). They proposed that at high Reynolds number, hairpin vortices could group together to form larger structures, as was subsequently confirmed by Kim and Adrian (1999).

LSMs are believed to be clusters of hairpin vortices aligning themselves in a ramp-like pattern inclined at an angle to the wall (Head and Bandyopadhyay, 1981; Kim and Adrian, 1999; Zhou et al., 1999; Guala et al., 2006; Adrian, 2007; Balakumar and Adrian, 2007). These LSMs are then observed to align coherently to form VLSMs (Kim and Adrian, 1999). The existence of VLSMs has been confirmed by a number of studies in pipe and channel flows (Guala et al., 2006; Monty et al., 2007; Balakumar and Adrian, 2007; Abe et al., 2004). VLSMs are up to $12-14\delta$ long in the streamwise direction.

Hutchins and Marusic (2007a) analyzed zero pressure gradient boundary layer over wide range of Reynolds numbers using a spanwise rake of hot-wires. They found very long meandering streamwise fluctuations as long as 20δ. They called them "superstructures" and compared them to the VLSMs observed by Kim and Adrian (1999) in the pipe flow. They also observed superstructures in the logarithmic region of the atmospheric boundary layer at $Re_\tau \approx 6.6 \times 10^5$.

LSMs, VLSMs and superstructures are characterized by streaks of low streamwise momentum. In case of LSMs, this streak is caused between the two legs of the hairpin vortices within the hairpin packets (Brown and Thomas, 1977; Meinhart and Adrian, 1995; Adrian et al., 2000; Ganapathisubramani et al., 2003; Tomkins and Adrian, 2003; Adrian, 2007; Hutchins et al., 2011; de Silva et al., 2017). These low momentum streaks are observed to be accompanied by high momentum regions on either side (Hutchins et al., 2011). These features of coherent motions are analogous to the near-wall cycle but at a larger scale (Lozano-Durán et al., 2012; Klewicki, 2010; Falco, 1977; Baars et al., 2017b; McKeon, 2017).

In summary, the presence of large-scale structures is universally observed in canonical turbulent boundary layers. While studying large-scale structures in the turbulent boundary layers, researchers have also observed the effect they exert on the near-wall small-scale structures and the wall-shear stress fluctuations. The large-scale influence on the near-wall small-scales is observed to be a function of Reynolds number. A summary of these scale interactions, particularly at high Reynolds numbers, is presented in the following section after a more general summary on higher Reynolds number effects.

2.2 High Reynolds Number Effects

This section discusses the effects of high Reynolds number on flow structures, the turbulence intensity and turbulent kinetic energy. In the current discussion, the cut-off wavelength separating the large-scales and the small-scales will be assumed

to be δ (boundary layer thickness, half-width of channel or pipe radius) based on Ganapathisubramani et al.'s (2012) work unless noted otherwise, i.e., the large-scales are structures with $\lambda_x \geqslant \delta$ and small-scales are structures with $\lambda_x < \delta$.

It is well established that the streamwise turbulence intensity peaks near the wall at $z^+ \approx 15$ in all canonical boundary layers (Smits et al., 2011). This peak is referred to as the inner peak or near-wall peak. The location of the near-wall peak is independent of the Reynolds number when normalized using viscous units (Marusic and Kunkel, 2003; Monty et al., 2009; Marusic et al., 2010; Hutchins et al., 2012; Vallikivi et al., 2015).

Figure 2.5 shows a variation of the turbulence intensity in zero pressure gradient boundary layers including the atmospheric boundary layer over a range of Reynolds numbers. As seen in the figure, the inner peak is constant for all Reynolds numbers at $z^+ \approx 15$. As the Reynolds number increases, a peak appears in the outer region of the boundary layer. Spectral analyses of the boundary layer reveals that the near-wall peak in turbulence intensity are primarily caused by small-scale structures, while the outer peak is associated with the large-scale structures (Klewicki, 2010; Marusic et al., 2010; Smits et al., 2011; Hutchins et al., 2012; Vallikivi et al., 2015; Dogan et al., 2016).

Hutchins and Marusic (2007a) analyzed zero pressure gradient boundary layers spanning over a decade of Reynolds numbers. As discussed, Hutchins and Marusic observed an outer peak emerging in energy spectra with increase in Reynolds number.

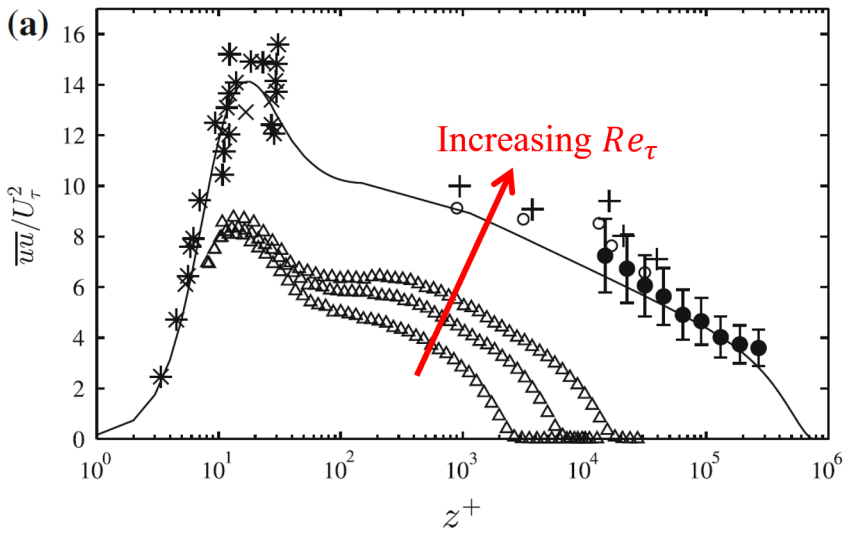

Figure 2.5. Turbulence intensity variation in zero pressure gradient boundary layers with increasing Reynolds numbers. The symbols △ represent data from laboratory experiments and the other are from the atmospheric boundary layer. Taken from Hutchins et al. (2012).

Figure 2.6 shows a pre-multiplied energy spectra from a low ($Re_\tau \approx 1000$) and a high ($Re_\tau \approx 7300$) Reynolds number zero pressure gradient boundary layer (Hutchins and Marusic, 2007a). As seen in this figure, there is a clear inner peak in the near-wall region associated with small-scale structures ($\lambda_x < \delta$) for both the Reynolds numbers. At higher Reynolds number, an energy peak appears in the outer region associated with the large-scale structures ($\lambda_x > \delta$).

Along with the increase in the energy of the large-scales at high Reynolds numbers, these large-scales were observed to interact with the near-wall small-scale structures (Hutchins and Marusic, 2007b). A summary of this inner-outer interaction is provided in the following section.

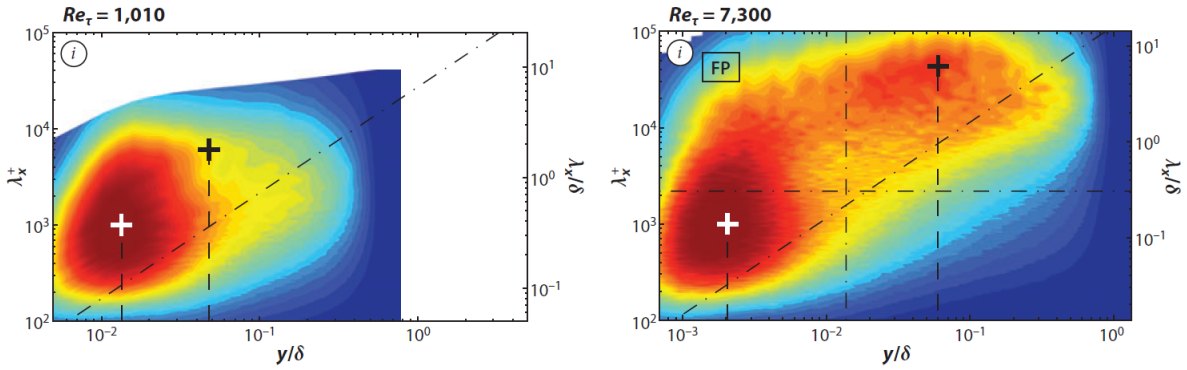

Figure 2.6. Pre-multiplied energy spectra of a zero pressure gradient boundary layer at Re_τ = 1010 (left) and Re_τ = 7300 (right) showing the outer energy peak associated with the large-scale structures ($\lambda_x > \delta$) with increase in Reynolds number as observed by Hutchins and Marusic (2007a). The symbols + represent inner (white) and outer (black) peaks in the energy spectra. 'FP' indicates footprint of the outer large-scale at the wall. Taken from Smits et al. (2011).

2.2.1 Scale Interactions in Canonical Boundary Layers

The interaction between scales has been the focus of several research efforts over the last decade (Hutchins and Marusic, 2007a,b; Abe et al., 2004; Hoyas and Jiménez, 2006; Marusic et al., 010a; Jacobi and McKeon, 2013; McKeon et al., 2018). It has been established that the scales within a wall bounded flow interact in a complex manner (Klewicki, 2010). The consensus opinion regarding this interaction is that it has two aspects: 1). A linear superposition of the outer large-scales on the near-wall small-scales. 2), A non-linear amplitude and frequency modulation of the small-scales by the larger scales (Smits et al., 2011; Hutchins et al., 2009; Marusic et al., 010a).

2.2.1.1 Superposition of large-scales

Superposition is the phenomenon where the outer large-scale structures impose energy onto the near-wall small-scales. This phenomenon is believed to be responsible for the increase in the near-wall TI peak. This superposition is observed in the energy spectra of Figure 2.6 where the energetic large-scales in the outer region are seen to leave a "footprint" at the wall at $Re_\tau = 7300$ (indicated by 'FP' in the figure). This effect causes an increase in the inner TI peak. This characteristic of the flow is known as superposition of large-scales on near-wall small-scales.

The increase in magnitude of the inner peak was initially observed by De Graaff and Eaton (2000). They found the magnitude of the inner peak to be a strong function of Reynolds number. A similar observation was made by Metzger and Klewicki (2001). They not only observed the increase in the inner peak but also showed that it was because of the low-frequency (large-scale) motion in the outer region.

Abe et al. (2004) analyzed DNS channel flow data and observed the existence of very large-scales in the skin friction fluctuations. Hutchins and Marusic (2007b) used Abe et al.'s (2004) DNS data and a simple Gaussian filter and compared it with their own observations. They were able to show a similar footprint in the DNS data.

Recently, Samie et al. (2018) studied zero pressure gradient boundary layers at $Re_\tau = 6000 - 20000$ using hot-wire sensors one magnitude smaller than conventional sensors to fully resolve the inner TI peak and also observed an increase in the inner TI peak with increase in Re_τ.

2.2.1.2 Amplitude and Frequency Modulation

Amplitude and frequency modulation (AM and FM) is a significant characteristic of the outer large-scale influence on the inner small-scales of the flow in the scope of the current work. An illustration of the AM and FM effect on the near-wall small-scales is shown in Figure 2.7, as proposed by Ganapathisubramani et al. (2012). In this figure, the blue regions are zones of low momentum and the red regions are zones of high momentum, as seen in a typical turbulent boundary layer. The purple line is the large-scale component of the streamwise velocity, whereas the green line is the small-scale component of the streamwise velocity at a near-wall location. As seen in Figure 2.7, within a high-speed region the amplitude and frequency of the near-wall small-scales are increased. Conversely, within a low-speed region the amplitude and frequency of the near-wall small-scales are reduced.

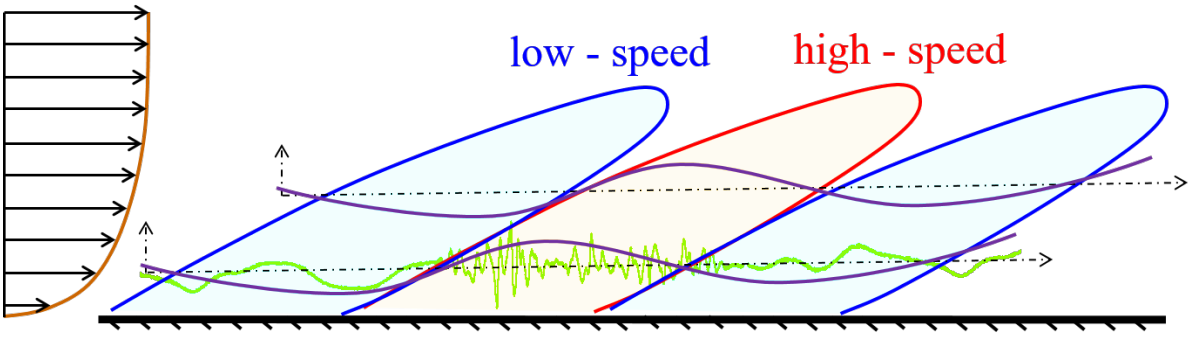

Figure 2.7. Illustration of amplitude and frequency modulation of the near-wall small-scale structures by the outer large-scales within a turbulent boundary layer. Adapted from Ganapathisubramani et al. (2012).

Evidence of this modulation type influence of the large-scales was first established in 1970s. Initially, when Rao et al. (1971) observed the "bursting" phenomena, they

also observed a coupling between the inner and the outer scales. They noticed that the proper scaling parameters for the burst period $\overline{T}$ in the inner region were the outer variables δ/U_∞. Similar observations were made by Falco (1977) and Brown and Thomas (1977). Brown and Thomas observed that the organized coherent motion in the boundary layer caused slow fluctuations in wall shear stress τ_w as well as increased amplitude of the fluctuation of bursts i.e. the small-scale structures. Falco (1977) referred to the bursting phenomena as "typical eddies" and found that the time period $\overline{T}$ for the typical eddies was in agreement with that of the bursts observed by Rao et al. (1971).

Bandyopadhyay and Hussain (1984) studied a number of flows to characterize the relationship between the large-scales and small-scales. They decomposed the velocity signal to obtain a correlation between the large-scale velocity component and the envelope of the small-scale component.

Hutchins and Marusic (2007b) decomposed the velocity signal into its large-scale and the small-scale components, using $\lambda_x^+ = 7300$ as the wavelength discriminator, and observed that the large-scales caused amplification or attenuation of the small-scale fluctuations. Mathis et al. (2009) further explored this interaction using a correlation coefficient between the large-scale components of the velocity signal and the large-scale envelop of the small-scale signal (obtained using a Hilbert transform). This coefficient is defined as the amplitude modulation correlation coefficient, i.e.,

$$R_{AM} = \frac{\overline{u_L E_L(u_s)}}{\sqrt{\overline{u_L^2}}\sqrt{\overline{E_L(u_s)^2}}}. \tag{2.1}$$

Where, u_L is the large-scale component of the velocity signal, u_s is the small-scale component of the velocity signal and E_L is the large-scale component of the envelope of u_s.

Chung and McKeon (2010) investigated large-eddy simulations (LES) of a channel flow at very high Reynolds number (Re_τ =200,000) and observed that the amplitude modulation coefficient between the large-scales and the envelope of the small-scales can also be interpreted as a measure of the phase difference between the same. A similar modulation effect was observed by Guala et al. (2011) in the very high Reynolds number atmospheric boundary layer ($Re_\tau \approx 5\times10^5$). They also observed a correlation between the envelope of the instantaneous dissipation and the large-scale component of the velocity at several wall-normal locations.

Ganapathisubramani et al. (2012) studied the effects of the LSMs on both the amplitude and frequency of the small-scales in zero pressure gradient boundary layers at high Reynolds numbers (Re_τ = 14,150). Along with the amplitude modulation, they noticed frequency modulation of the small-scale structures which was confined to the inner region ($z^+ < 100$). They proposed a structural schematics, which was used in Figure 2.7 to illustrate the near-wall scale modulation.

In a zero pressure gradient boundary layer, Jacobi and McKeon (2013) used the cospectral density to identify the dominant large-scale structure responsible for the amplitude modulation of the small-scale structures. They showed that this dominant structure was the VLSMs by comparing its size and gradient.

Following Mathis et al.'s (2009) work, and associated work (Marusic and Kunkel, 2003, 2004), Marusic et al. (2010) developed the "inner-outer-interaction model" (IOIM) that predicted velocity fluctuations in the near-wall region using only the large-scale information from the outer region of a given flow field. A similar model was proposed for predicting the streamwise near-wall turbulence statistics based on this inner-outer interaction (Mathis et al., 2011). Further development of this work led to a model to predict the wall-shear stress fluctuations in the zero pressure gradient boundary layer given an input from the outer region (Mathis et al., 2013). Baars et al. (2016) refined this IOIM model to eliminate a user-defined scale separation input.

In summary, based on prior work it is clear that the large-scale structures interact with near-wall small-scale structures and so also influence the near-wall turbulence.

2.3 Plane Wall Jet

Launder and Rodi (1983) defined a PWJ as "a boundary layer in which, by virtue of the initially supplied momentum, the velocity over some region in the shear layer exceeds that in the free stream." It is a unique shear layer in which the highly energetic large-scales of the outer free-shear layer transition to turbulence through an inviscid process while the wall-bounded layer becomes turbulent through a viscous mechanism.

The PWJ is also encountered in engineering applications such as in separation control on airfoils (Dunham, 1968), film cooling of turbine blades (Launder and Rodi, 1983) as well as a rotorcraft flying in ground effect (Rauleder and Leishman, 2014).

The present work focuses on the PWJ developing in quiescent conditions. In a PWJ, the evolution of the outer large-scale structures is analogous to a free-shear layer constrained only by inertia away from the wall (Wygnanski et al., 1992). In the vicinity of the wall, it is constrained by the viscous wall (Wygnanski et al., 1992). As a result, a PWJ mean velocity profile resembles a canonical turbulent boundary layers in the very near-wall region ($z^+ \lessapprox 10$) (George et al., 2000; Tachie et al., 2002; Banyassady and Piomelli, 2015), and manifests self-similarity when scaled using the outer variables (Glauert, 1956; Launder and Rodi, 1981).

A vast majority of the prior work focuses on the turbulent statistics and the self-similarity of the PWJ. A comprehensive review summarizing earlier studies of PWJs is given by Launder and Rodi (1981, 1983). A review of recent studies is given by Banyassady and Piomelli (2015). A fair amount of scatter in terms of the mean statistical properties has been reported in the prior studies. However, the PWJ exhibits certain universal similarities with canonical boundary layers.

The PWJ velocity profile in the very near-wall region ($z^+ < 10$) when plotted in viscous units collapses with the canonical boundary layers. Using the asymptotic invariance principle, George et al. (2000) derived a power law to describe the zero pressure gradient boundary layer in the near-wall region. They then assumed complete similarity in the inner and the outer region in the limit of infinite Reynolds

number to compare this power law to the PWJ. They proposed a composite velocity profile of the wall region for the PWJ, i.e.,

$$\begin{aligned} U^+ &= \left(z^+ + c_4 z^{+4} + c_5 z^{+5}\right)\exp\left(-dz^{+6}\right) \\ &+ C_i z^{+\gamma}\left(1 + \gamma a^+ z^{+-1} + \frac{1}{2}\gamma(\gamma-1)a^{+2} z^{+-2}\right)\left(1 - \exp\left(-dz^{+6}\right)\right). \end{aligned} \tag{2.2}$$

Where, $c_4 = -0.0003 \pm 0.0001$ and $c_5 = 13.5 \times 10^{-6}$ are the coefficients that may nominally vary with Reynolds number, C_i and γ are the local Reynolds number $Re_m = z_m U_m/\nu$ dependent constants determined based on the parameters George et al. (2000) determined, $d = 8\times10^{-8}$ is the damping parameter used for transitioning from the near-wall to the overlap region, and $a^+ = -16$ is an offset parameter treated as a constant.

George et al. (2000) and Tachie et al. (2002) compared this profile with a PWJ with good agreement. Chauhan et al. (2009) used a similar composite profile for a zero pressure gradient boundary layer, which is shown to have good agreement for flows up to $Re_\tau = 22884$ (Kulandaivelu, 2011). Figure 2.8 shows a comparison of the composite velocity profiles in the very near-wall region as proposed by George et al. (2000) and Chauhan et al. (2009), along with the zero pressure gradient boundary layer DNS data from Sillero et al. (2013) ($Re_\tau = 1307$), the channel flow DNS data from Lee and Moser (2015) ($Re_\tau = 2000$) and the PWJ DNS data from Ahlman et al. (2009) ($Re_\tau = 2000$). As seen in the figure, the profiles are in excellent agreement for $z^+ \lessapprox 10$.

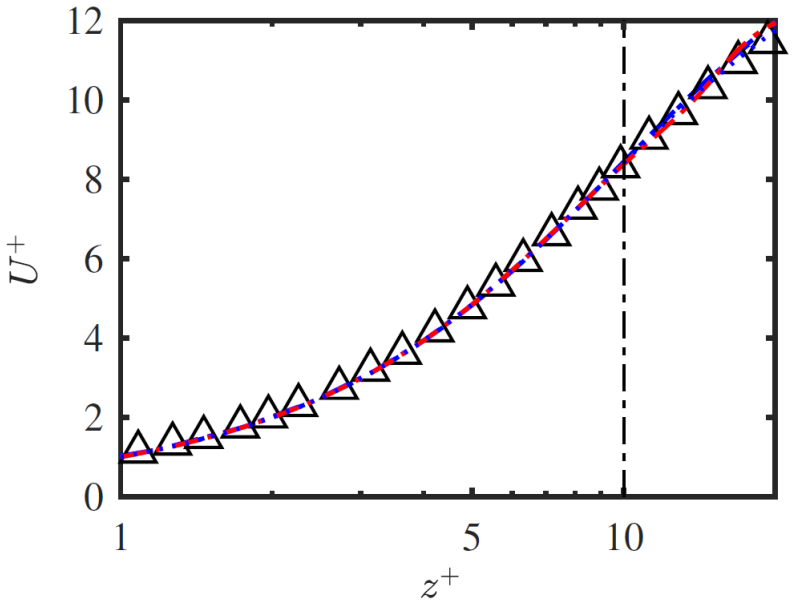

Figure 2.8. Comparison of the composite velocity profiles of George et al. (2000) (- - - -) and Chauhan et al. (2009) (·····). Also shown are the zero pressure gradient boundary layer DNS data of Sillero et al. (2013) at Re_τ = 1307 (- - - -), channel flow DNS data of Lee and Moser (2015) Re_τ = 2000 (- - - -) and PWJ DNS data of Ahlman et al. (2009) at Re_τ = 2000 (△). Figure taken from Gnanamanickam et al. (2019).

Despite this agreement of the velocity profiles in the near-wall region, the log-law constants ($U^+ = Az^+ + B$, where A = 2.44 and B = 5.0 for a zero pressure gradient boundary layer) are not well established for the PWJ. Significant scatter has been reported in the log-law constants A and B. Some studies suggests its universality and confirms the values to be the same as the zero pressure gradient boundary layer log-law constants (Eriksson et al., 1998; Dejoan and Leschziner, 2005) while a wide range of values have been reported by others.

Some studies report that the log-law constants are depended on the inlet Reynolds number $Re_j = V_j b/\nu$ (Guerra et al., 2005) or the local flow characteristics such as

U_m/U_τ (Wygnanski et al., 1992; Guerra et al., 2005; Naseem et al., 2009). A summary of different values reported in the literature is given by Banyassady and Piomelli (2015).

A typical PWJ turbulence intensity exhibits two peaks as illustrated in Figure 1.2. Similar to the zero pressure gradient boundary layer, the inner turbulence intensity peak in the PWJ occurs at $z^+ \approx 15$ (Zhou et al., 1996) and remains the lower in magnitude than the outer peak. The outer peak can be thought to be analogous to the outer turbulence intensity peak seen in the adverse pressure gradient boundary layers (Harun et al., 2013), and the zero pressure gradient boundary layer developing under the influence of high free stream turbulence (Sharp et al., 2009; Dogan et al., 2016). Spectral analyses reveals that this outer peak in the PWJ turbulence intensity corresponds to extremely energetic large-scale structures when compared to the zero pressure gradient boundary layer at similar Reynolds numbers.

There are very few prior studies discussing the coherent structures within a PWJ. In a flow visualization of a fully turbulent PWJ, Katz et al. (1992) observed coherent structures associated with the outer free-shear layer as well as the inner boundary layer. They also observed that these structures extend form the wall to the outer jet region suggesting that PWJ cannot be treated as two independent superimposed shear layers. Dejoan and Leschziner (2005) concluded through their large-eddy simulation (LES) analyses that these outer large-scales move to the wall-layer by turbulent diffusion. Using instantaneous snapshots from this study Dejoan et al. (2006) showed

streaky streamwise structures in the near-wall region of the PWJ that are similar to those seen in the canonical boundary layers.

Banyassady and Piomelli (2014) used LES based two point correlations to show that the PWJ contains forward leaning structures in near-wall region similar to those seen in the canonical boundary layers. Figure 2.9(a) shows the instantaneous velocity fields from the particle image velocimitry (PIV) measurements of the current PWJ (Gnanamanickam et al., 2019). Hairpin packets, similar to those seen in zero pressure gradient boundary layer, are observed in the wall-normal-streamwise plane in the wall region ($z < z_m$). Furthermore, these structures are observed to be inclined at 15° to the wall. The two-point correlation $R_{uu}(\Delta x, z_r)$ using a PIV data set is shown in figure 2.9(b). A forward leaning structure in the near-wall region can be seen. A signature of the backward leaning flow structures is observed in the outer most location shown ($z_r^+ \approx 0.6Re_\tau$). These observations are consistent with Banyassady and Piomelli's (2014) observations in a PWJ LES.

Similar to canonical boundary layers, these energetic large-scales within a PWJ are seen to amplitude modulate the near-wall small-scales. Figure 2.10 shows this amplitude and frequency modulation effect in the near-wall velocity signal of the current PWJ. As shown, the red box shows a low-speed event where the large-scales reduce the amplitude and frequency of the corresponding small-scales, while the blue box shows the corresponding high-speed event. This similarity with canonical boundary layers is also reflected in the amplitude modulation correlation coefficient R_{AM} (see Figure 2.11) for the PWJ (Gnanamanickam et al., 2019).

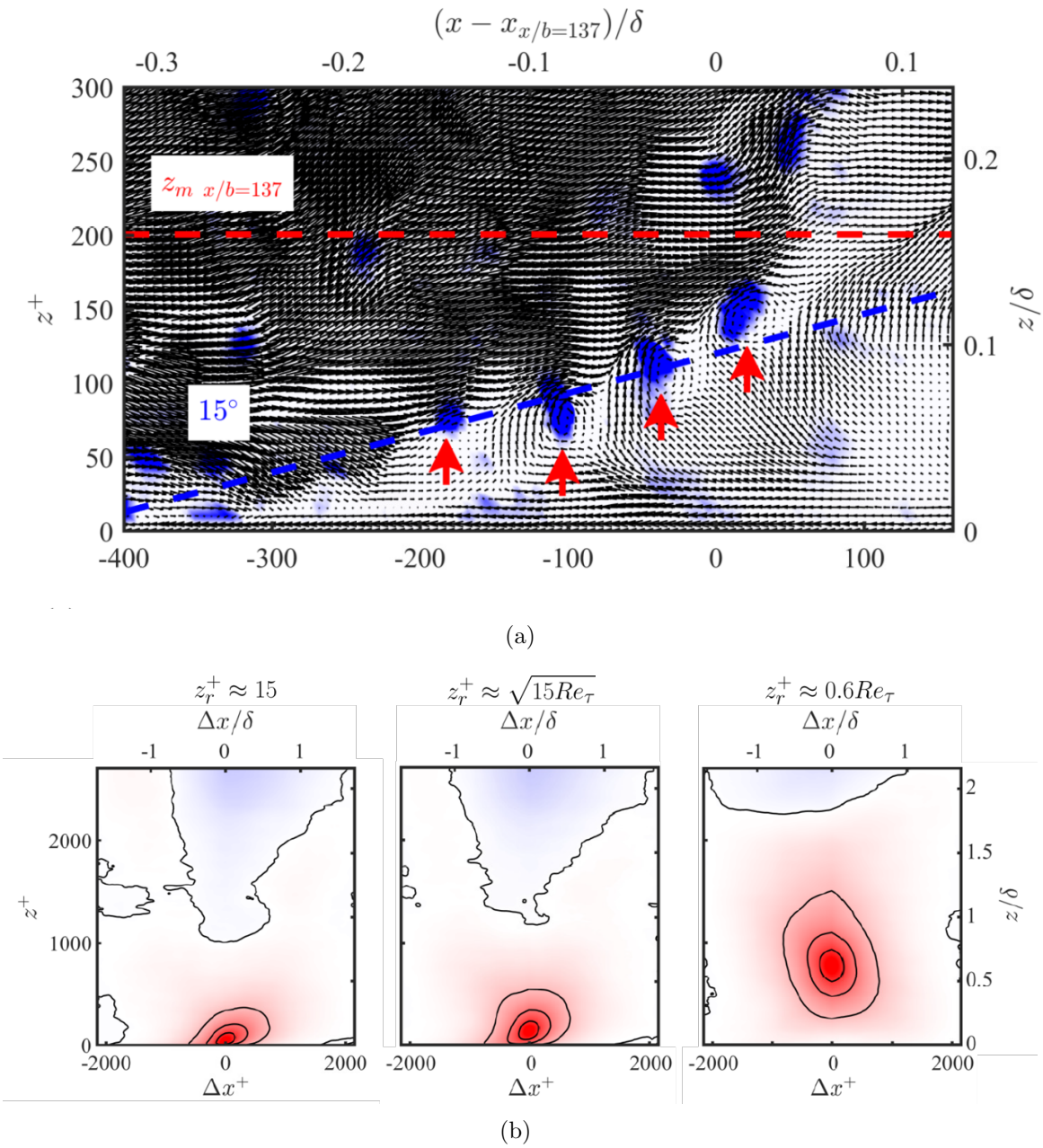

Figure 2.9. (a) The PWJ instantaneous velocity fields from particle image velocimitry (PIV) measurements and (b) the corresponding two-point correlation $R_{uu}(\Delta x, z_r)$ in the wall-normal-streamwise plane. The red arrows indicate the cores of hairpin packets with clockwise vorticity. Figures taken from Gnanamanickam et al. (2019).

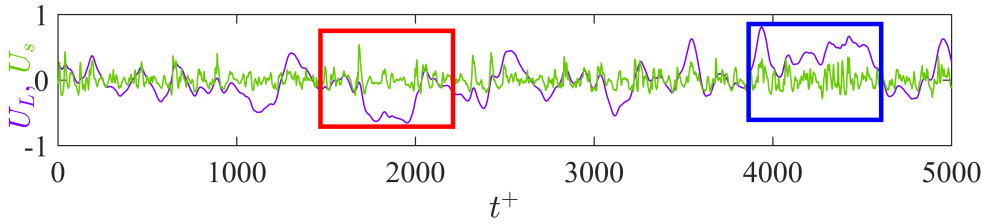

Figure 2.10. Velocity field in the near-wall region at $z^+ \approx 6$ of the PWJ decomposed into the large-scale U_L and the small-scale U_s components. The amplitude of the small-scale components has been scaled down by a factor of 3 for the purpose of visualization. The red box highlights one of the low-speed events, where a low-speed large-scale structure reduces amplitude and frequency of the small-scale structures. The blue box highlights one of the high-speed events, where a high-speed large-scale structure increases amplitude and frequency of the small-scale structures.

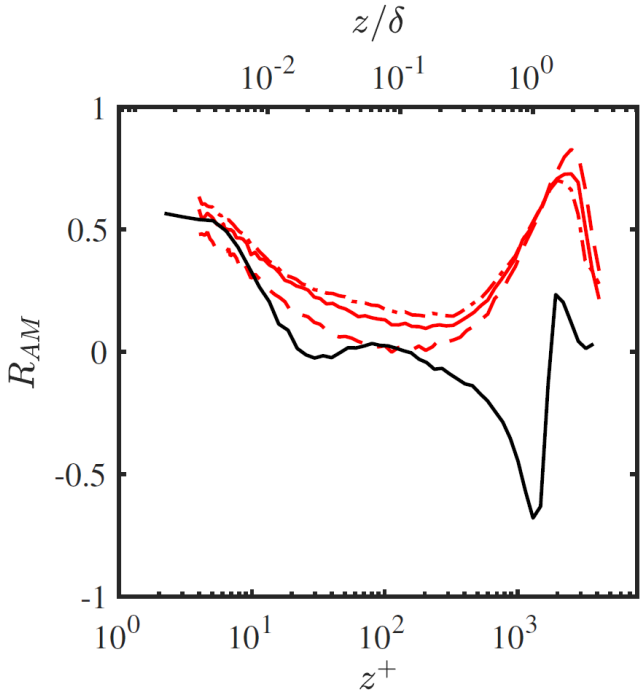

Figure 2.11. A comparison of the amplitude modulation coefficient R_{AM} of the PWJ, using different large-scales discriminator thresholds ($\lambda_x = \delta$: - - - -, $\lambda_x = 2\delta$: ——, $\lambda_x = 4\delta$: - - - -), with a zero pressure gradient boundary layer (——, Nugroho et al. (2013)) using $\lambda_x = 2\delta$ threshold as given by Gnanamanickam et al. (2019).

An overview of past studies regarding the forced PWJ relevant to the present work is now presented. Katz et al. (1992) and Zhou et al. (1996) acoustically forced a PWJ and investigated their influence on the embedded coherent motions. Katz et al. (1992) observed that the rate of spread of the PWJ and the maximum mean velocity were unchanged upon forcing. They noticed that the forcing increased the two-dimensionality of the PWJ. They also observed that despite no apparent alteration in the mean velocity, the forcing reduced the wall-shear stress and the streamwise turbulence intensity in the near-wall region ($z^+ < 100$).

Zhou et al. (1996) observed that the forcing increased the coherence of the large-scale structures and that the momentum exchange between the PWJ and the entrainment largely depended on these large-scale structures. Schober and Fernholz (2000) manipulated the outer shear layer of the PWJ using a self-oscillating wire to force and a still wire to suppress the outer coherent structures. They observed decreased skin-friction and increased outer turbulence intensity peak when the flow was forced, whereas decreased turbulence intensity when they suppressed the outer shear layer.

Therefore it can be concluded that, a PWJ exhibits characteristics that resemble a zero pressure gradient boundary layer in the near-wall region. The PWJ contains extremely energetic outer large-scale structures at very modest development lengths that are responsible for the outer turbulence intensity peak. In addition, these outer large-scales interact with the near-wall small-scale structures. Studies of the forced turbulent PWJ show that manipulating the outer shear layer strongly influences the

near-wall region. Therefore, the outer large-scale structures are a suitable target for the purpose of the current work.

3. Experimental Approach

This chapter discusses the details of the current PWJ experimental facility and the hot-wire measurement techniques used to conduct the experiments. The PWJ exit conditions and the two-dimensionality are documented in this chapter. The approach used for calculating the friction velocity U_τ is also discussed.

3.1 Experimental Facility

Measurements were carried out in a PWJ facility at Embry-Riddle Aeronautical University. A schematic of the facility is shown in Figure 3.1. The PWJ facility is designed to generate a thick incompressible flow layer at sufficiently high frictional Reynolds number ($Re_\tau > 1000$). The PWJ facility is powered using a centrifugal fan and the fan speed is controlled using a variac. Air flow from the fan passes through a series of filters and screens before entering the plenum chamber.

A speaker is installed in the plenum chamber to acoustically force the PWJ. From the plenum, air goes through a honeycomb followed by a two-dimensional contraction channel of ratio 16:1 and into a rectangular nozzle exit. The contraction curvature was designed using a fifth-order polynomial. The nominal nozzle exit height $b = 5$ mm and thus the exit has an aspect ratio of 128. Past the jet exit, a 5 inch long strip of 60 grit sandpaper is installed across the span, which trips the boundary layer at the wall and ensures a controlled transition of the inner wall layer. A comparison of the pre-multiplied energy spectra before and after the sandpaper installation is shown

in Appendix D. The test section of the facility is 12 ft (3.66 m) long, resulting in a fully developed PWJ with a thick shear layer. The entrainment was controlled using a series of screens and honeycomb, as shown in Figure 3.1.

3.2 Hot-Wire Measurements

All the measurements were conducted using single wire hot-wire anemometry (HWA). The hot-wire sensors were made from Wallaston platinum wire of diameter d = 2.54 µm. The ratio of the length to diameter was ensured to be nominally 200 to adequately resolve the near-wall small-scale fluctuations (Hutchins et al., 2009). The length of the sensing elements along with a summary of flow parameters for the present set of unforced PWJ measurements are summarized in Table 3.1. Table 3.2 lists the corresponding flow parameters for the forced PWJ.

The sensors were operated in constant temperature mode using Embry-Riddle Aeronautical University's in-house anemometer with an over-heat ratio of 1.8. The sensors were calibrated using a calibration jet before and after each run (pre-calibration and post-calibration). Details of the calibration jet are given in Appendix A. A third order polynomial curve was used to fit the calibration data. The average velocity using the pre-calibration and post-calibration was used to account for the difference in the calibrations before and after a run.

A boundary-layer type probe was used to carry out all measurements. The probe was supported using streamline tubing to reduce flow disruption. The sensor was traversed in the wall-normal direction using a traversing system. The traverse has

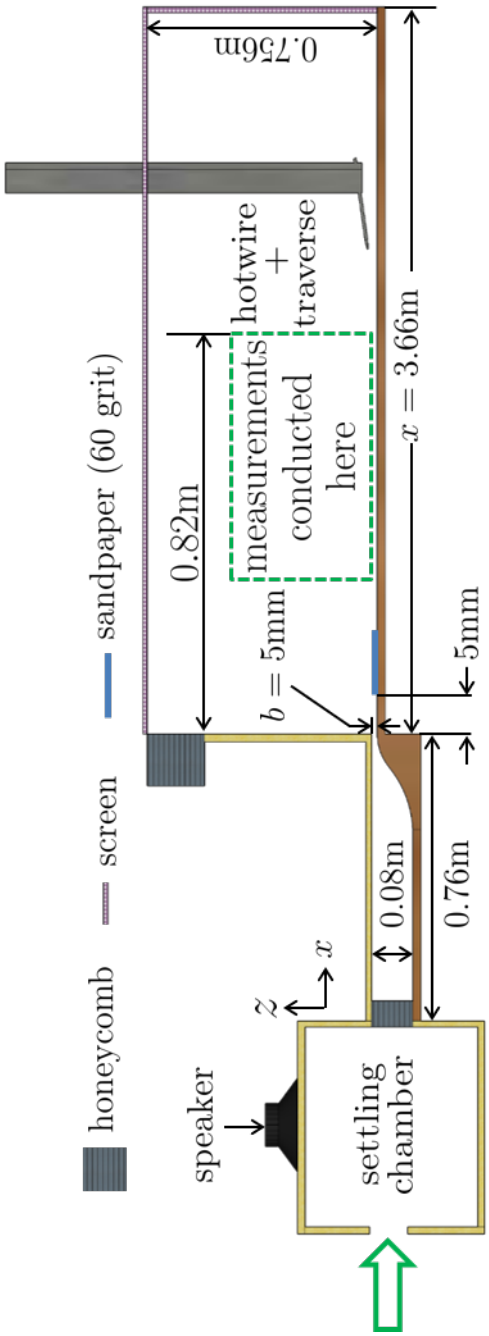

Figure 3.1. A schematic highlighting key features of the experimental facility and the measurement setup. The figure is not to scale. A scaled model of the current facility is shown in Appendix E

Table 3.1.
Experimental parameters from the current hot-wire measurements for the unforced PWJ. Here, x is streamwise direction, b the jet exit height, $Re_j = V_j b/\nu$ is the jet exit Reynolds number, V_j is the jet exit velocity, ν is the kinematic viscosity, U_m is the maximum velocity, u_τ is the friction velocity, z_0^+ is the point nearest to the wall used for calculating the friction velocity, $Re_\tau = u_\tau \delta/\nu$ is the friction Reynolds number, δ is the outer length scale, ν/u_τ is the viscous length scale, l is the length of hot-wire sensing element, d is the hot-wire sensor diameter, T is the sampling time, $\Delta T = 1/f_s$ is the sampling period, f_s is the sampling frequency, f_{HW} is the resonance frequency of the hot-wire sensing element and $f_c = U_\tau^2/3\nu$ is the maximum frequency in the flow as per Hutchins et al. (2009). The superscript '*' indicates the forced data sets discussed in subsequent chapters.

x/b	Re_j	V_j ms^{-1}	U_m ms^{-1}	U_τ ms^{-1}	z_0^+	Re_τ	ν/U_τ µm	δ cm	l^+	l/d	TU_m/δ	ΔT^+	f_s kHz	f_{HW} kHz	f_c kHz
50	5905	17.94	5.95	0.4009	4.34	901	38	3.47	13.5	205	72071	0.5209	20	16.7	3.5
50*	5902	17.83	5.91	0.3834	4.20	868	40	3.48	25	200	40790	0.1835	20	7.2	3.2
50	5896	17.84	6.04	0.3976	4.15	900	39	3.48	26	200	41654	0.2044	20	7.2	3.4
75	5879	17.96	4.88	0.3296	4.05	1039	47	4.89	21	200	35939	0.1154	20	7.2	2.3
75*	5933	17.85	4.81	0.3325	4.26	1038	46	4.77	22	200	33290	0.1203	20	7.1	2.4
95	5965	17.94	4.41	0.2898	4.22	1093	53	5.76	9.9	205	36743	0.2748	20	16.7	1.8
110*	5964	17.98	4.18	0.2700	4.02	1199	56	6.77	9.8	216	25967	0.2425	20	15	1.6
110	5888	17.96	3.97	0.2709	4.34	1172	57	6.71	9.1	205	42592	0.2365	20	16.7	1.6
125	5901	17.89	3.75	0.2551	4.15	1245	60	7.51	8.6	205	29928	0.2116	20	16.7	1.4
125	5868	17.90	3.88	0.2638	4.11	1282	59	7.52	8.9	205	30984	0.225	20	16.7	1.5
137	5867	17.90	3.68	0.2463	4.02	1271	63	8.00	8.3	205	33111	0.1957	20	16.7	1.3
137*	6001	18.06	3.73	0.2471	4.20	1315	62	8.11	8.9	216	22068	0.2002	20	15	1.3
137	6000	18.03	3.74	0.2370	4.12	1219	65	7.87	8.5	217	19987	0.1836	20	15.1	1.2
137	5955	17.95	3.64	0.2400	4.14	1249	64	7.97	8.6	217	21915	0.1881	20	15.1	1.3
137	5925	18.02	3.79	0.2436	4.19	1242	64	7.90	8.7	217	23060	0.1917	20	15.1	1.3
137	5940	18.07	3.72	0.2442	4.05	1260	63	7.99	8.7	217	22370	0.1926	20	15.1	1.3
137	5965	18.07	3.74	0.2421	4.08	1269	64	8.09	8.6	217	22202	0.1899	20	15.1	1.3
150	5880	17.79	3.67	0.2416	4.11	1390	64	8.85	8.7	217	27352	0.1897	20	15.1	1.3
162	5903	17.94	3.29	0.2231	4.70	1325	69	9.14	7.6	205	25958	0.1617	20	16.7	1.1
162*	5991	18.00	3.62	0.2261	4.10	1396	68	9.46	8.1	216	18354	0.1669	20	15	1.1
162	5867	17.86	3.52	0.2244	4.25	1325	69	9.12	7.5	205	25474	0.1626	20	16.7	1.1
137	5972	18.04	–	0.2335	4.24	–	66	–	8.4	217	–	0.1776	20	15.1	1.2
137	5932	18.02	–	0.241	4.10	–	64	–	8.6	217	–	0.1881	20	15.1	1.3
137	5986	18.11	–	0.2493	4.26	–	62	–	8.9	217	–	0.2023	20	15.1	1.3

Table 3.2.
Flow properties for the unforced and the corresponding forced PWJ. Here, $C_{f_j} = 2U_\tau^2/V_j^2$ is the friction coefficient.

x/b	f_f Hz	λ_j/b	V_j ms^{-1}	Re_j	U_m ms^{-1}	δ cm	U_τ ms^{-1}	Re_τ	Cf_j $\times 10^{-4}$
50	0	0	17.83	5902	5.90	3.48	0.3833	868	9.24
50	7	500	17.82	5899	5.64	4.08	0.3707	986	8.65
50	12	295	17.81	5896	5.36	4.28	0.3580	999	8.08
50	16	220	17.81	5894	5.46	4.43	0.3600	1038	8.17
75	0	0	17.85	5933	4.81	4.77	0.3325	1038	6.94
75	7	500	17.84	5931	4.66	5.55	0.3226	1171	6.54
75	12	295	17.84	5929	4.50	5.88	0.3132	1204	6.17
75	16	220	17.84	5929	4.56	5.95	0.3134	1220	6.17
110	0	0	17.98	5964	4.18	6.77	0.2700	1199	4.46
110	7	500	17.98	5964	3.93	7.84	0.2553	1306	4.03
110	12	295	17.98	5964	3.85	8.17	0.2495	1332	3.85
110	16	220	17.98	5964	3.92	8.20	0.2539	1359	3.99
137	0	0	18.06	6001	3.73	8.11	0.2471	1315	3.73
137	7	500	18.06	6001	3.48	9.50	0.2326	1446	3.32
137	12	295	18.06	6001	3.43	9.93	0.2293	1489	3.23
137	16	220	18.06	6001	3.49	9.75	0.2326	1484	3.32
162	0	0	18.00	5991	3.62	9.46	0.2261	1396	3.08
162	7	500	18.00	5991	3.35	10.96	0.2072	1488	2.65
162	12	295	18.00	5992	3.31	11.08	0.2038	1481	2.57
162	16	220	18.00	5992	3.37	11.01	0.2066	1490	2.64

the ability to move in increments of 6.35 µm. The motion of the traverse was tracked using a linear magnetic encoder with a resolution of 1 µm.

The measurements were conducted in the wall-normal direction at points logarithmically spaced with each other. At each wall-normal location, the measurements were first conducted for the unforced flow, followed by each forcing frequency before moving to the next wall-normal location. The hot-wire signals were sampled at 20kHz using a Data Translation DT9836 16-bit data acquisition board.

The largest flow frequency as estimated using the quantity $\approx U_\tau^2/3\nu$ (Hutchins et al., 2009) is given in Table 3.1. A 2kHz low-pass cut-off filter was used for all the data presented in the current work. The atmospheric temperature and pressure was monitored using a thermocouple and a barometer (Omega - PX409-32B5V). The PWJ exit velocity was monitored using the chamber pressure measured using a pressure transducer (Omega PX653-05D5V).

A function generator was used to generate the forcing signal for the PWJ. A pulse function with width of 0.001 s was used at the desired frequencies for all the forcing cases presented (see Figure 3.3). The signal was amplified using an amplifier before being fed to the speaker. Various MATLAB scripts were used to communicate with all devices and to automate the process where necessary.

It is noted that because of the single HWA technique used, all the measurements presented in the current work measures effective velocity $U = \overline{U} + U' = \sqrt{(u+u')^2 + (w+w')^2}$. Here, $\overline{U}$ is the resultant mean velocity divided in the mean streamwise u the wall-normal w components. Whereas, U', u' and w' are the corre-

sponding fluctuations. The single hot-wire sensitivity to the spanwise velocity component is negligible. These notations are used for the rest of this work.

3.3 PWJ Exit Profiles

The nominal PJW exit velocity V_j for the presented cases is nominally 17.95 ms^{-1} and the corresponding Reynolds number $Re_j = V_j b/\nu \approx 5975$. Figure 3.2 shows the typical velocity and turbulence intensity profiles at the PWJ exit for the unforced and the primary forcing conditions. The turbulence intensity at the PWJ exit was 0.7%, 5.5%, 1.8% and 2.5% for the unforced, forced at 7Hz, forced at 12Hz and forced at 16Hz flows respectively.

While Figure 3.2 shows the average velocity at the exit, Figure 3.3 shows a typical forced velocity at the PWJ exit centerline and the corresponding forcing voltage signal. A parametric study was conducted to ensure constant energy input upon forcing over a forcing cycle at the exit of the PWJ. This study is documented in the following section.

3.4 Energy of Forcing at PWJ Exit

To ensure that the energy over a sampling period being added to the flow is constant, the following was carried out. The PWJ was forced at twenty different frequencies from 1 to 20 Hz and twenty-five different amplitudes varying from 0.2 V_{pp} to 5 V_{pp} where V_{pp} is peak to peak voltage.

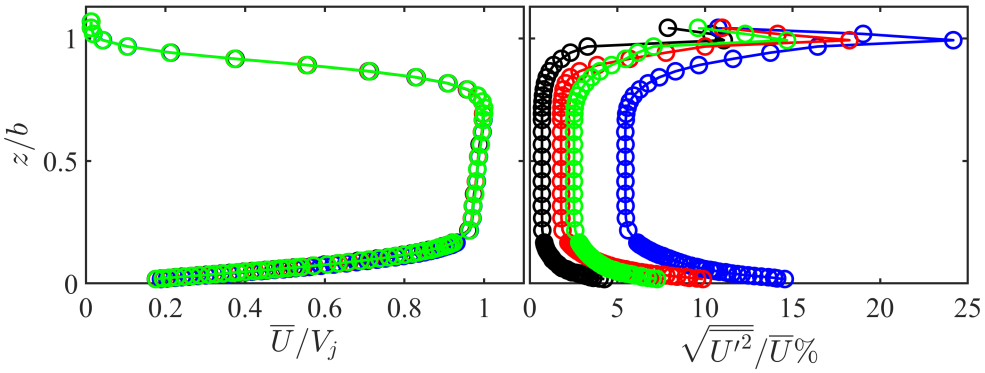

Figure 3.2. Velocity profile (left) and turbulence intensity (right) at the jet exit. Here, V_j is the PWJ exit velocity calculated from the static pressure in the contraction. The lines indicate unforced ( ), forced 7Hz ( ) , forced 12Hz ( ) and forced 16Hz ( ) flows respectively.

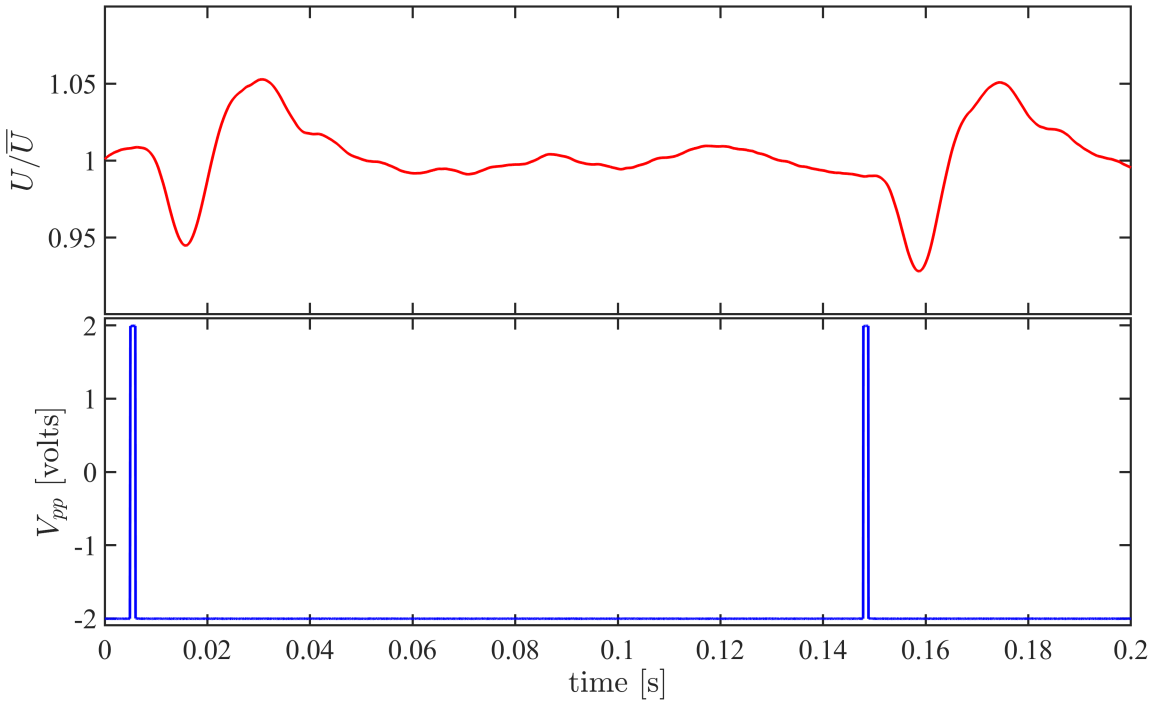

Figure 3.3. Forcing velocity at the PWJ exit at $z = 0.5b$ (top) and the corresponding forcing pulse fed to the speaker (bottom) for $f_f = 7$ Hz forcing with $V_{pp} = 4.0$ V.

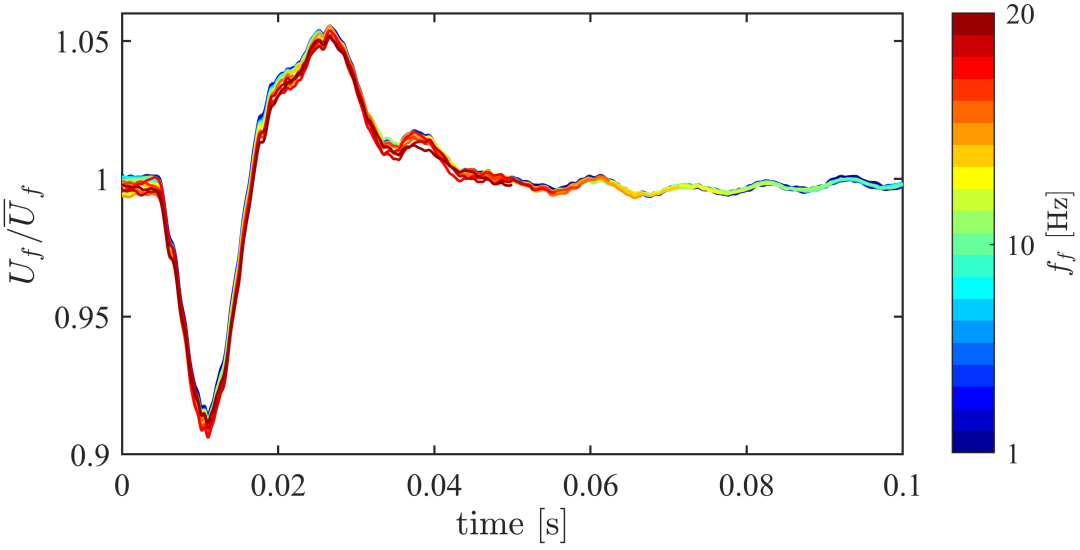

Figure 3.4. An average forcing cycle for the frequencies ranging from $f_f = 1 - 20$ Hz at $V_{pp} = 4.0$ averaged over the total number of cycles within the sampling period.

The PWJ exit centerline velocity was measured at $z = 0.5b$ for 120 s. This velocity is shown in Figure 3.3 along with the corresponding forcing signal for $f_f = 7$ Hz and $V_{pp} = 4$.

Figure 3.4 shows the averaged forcing cycle when $V_{pp} = 4.0$ at all the chosen forcing frequencies. The energy upon forcing was then calculated, which is shown in Figure 3.5 as a function of the forcing frequency and the amplitude. This energy was calculated over the total sampling time for each case, so is a measure of the total energy over a certain time period.

Using these experimental values, a function was fit to calculate the required forcing amplitude for the desired forcing frequency to give a constant energy of forcing. For the current work this value refers to $\approx 8.78. \times 10^{8}$ Jkg^{-1}. More information on calculation this constant energy is given in Appendix C.

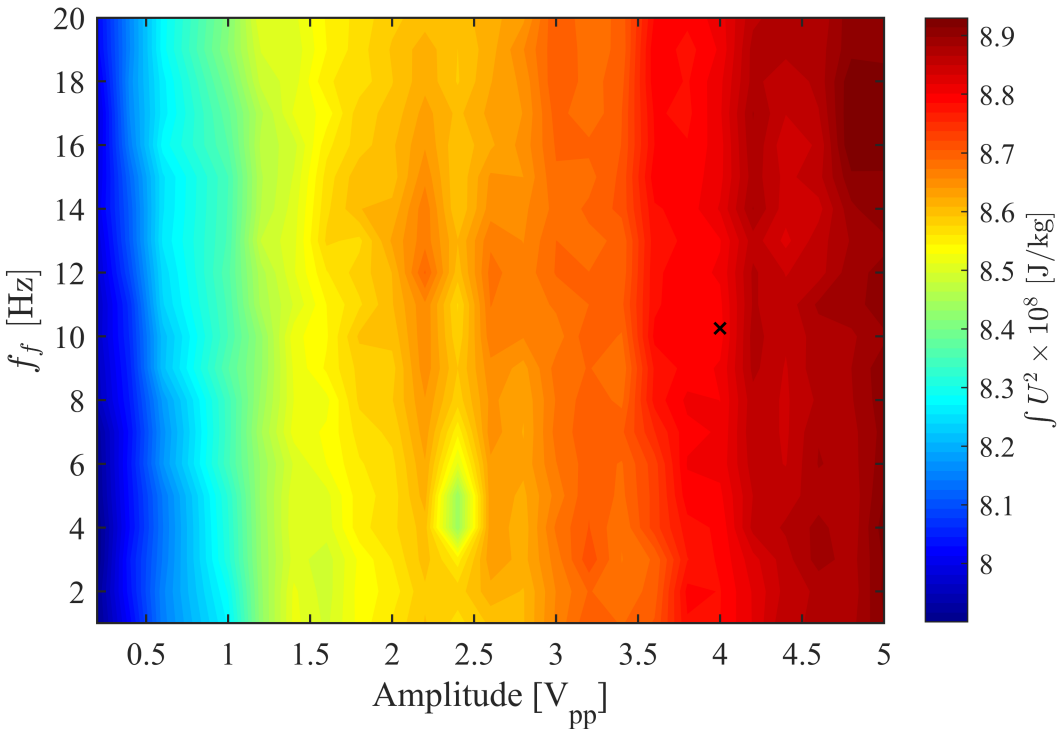

Figure 3.5. Forcing energy at the PWJ exit centerline as a function of the forcing frequency f_f and amplitude V_{pp}. The black cross indicates energy value ($\approx 8.78. \times 10^8$ Jkg^{-1}) chosen for current work.

3.5 Two Dimensionality

The two-dimensionality of the PWJ was tested at the exit and several streamwise locations up to $x/b = 162$ across a span of ± 5.5 inches from the jet centerline. The average velocity variation across the span at the farthest streamwise location was $\pm 0.36\%$. In Launder and Rodi's (1981) review, they emphasized the use of the streamwise momentum equation to determine the two-dimensionality of the PWJ. They observed that the friction losses corresponded to only a small percentage of the momentum loss, and any large momentum losses observed at the downstream locations had to be attributed to the lack of two-dimensionality of the flow. Therefore, the current work used the two-dimensional momentum equation to determine the two-dimensionality of the PWJ. Irwin (1973) derived a two-dimensional momentum equation for a PWJ based on standard boundary layer approximations. Integrating this equation in the streamwise direction would give the momentum integral equation for a PWJ (George et al., 2000; Eriksson et al., 1998).

3.5.1 Derivation of the Momentum Integral Equation

The equation of motion for a PWJ as derived by Irwin (1973) is given as

$$\overline{U}\frac{\partial \overline{U}}{\partial x} + \overline{W}\frac{\partial \overline{U}}{\partial z} + \frac{\partial\left(u^2 - w^2\right)}{\partial x} = \frac{\partial}{\partial z}\left(-uw + \nu\frac{\partial \overline{U}}{\partial z}\right). \tag{3.1}$$

The boundary conditions for a PWJ are,

$$\text{At } z = 0,\ \overline{U} = 0 \text{ and } \overline{W} = 0$$

$$\text{As } z \to \infty,\ \overline{U} \to 0.$$

Equation 3.1 is further simplified using the the continuity equation as

$$\frac{\partial}{\partial x}\left(\overline{U}^2 + u^2 - w^2\right) + \frac{\partial \overline{UW}}{\partial z} = \frac{\partial}{\partial z}\left(-uw + \nu\frac{\partial \overline{U}}{\partial z}\right). \tag{3.2}$$

Integrating Equation 3.2 with respect to z and applying the boundary conditions yields

$$\frac{\partial}{\partial x}\int_0^\infty \left(\overline{U}^2 + u^2 - w^2\right) dz = (-uw) + \nu\frac{\partial \overline{U}}{\partial z}. \tag{3.3}$$

Integrating Equation 3.3 with respect to x yields

$$\int_0^\infty \left(\overline{U}^2 + u^2 - w^2\right) dz = M_0 - \int_0^x \frac{\tau_w}{\rho} dx. \tag{3.4}$$

Equation 3.4 is the integral momentum equation for a PWJ. Here, M_0 is the momentum of PWJ at some upstream location. For simplicity, it is assumed that

$$M_j = \int_0^\infty \left(\overline{U}^2 + u^2 - w^2\right) dz. \tag{3.5}$$

$$= M_0 - \int_0^x \frac{\tau_w}{\rho} dx. \tag{3.6}$$

Considering some reference location x_r in the flow, the momentum at this location is

$$\text{Therefore } M_r = M_0 - \int_0^{x_r} \frac{\tau_w}{\rho} dx \tag{3.7}$$

$$.M_0 = M_r + \int_0^{x_r} \frac{\tau_w}{\rho} dx \tag{3.8}$$

Substituting equation 3.8 in equation 3.6 yields,

$$M_j = M_r + \int_0^{x_r} \frac{\tau_w}{\rho} dx - \int_0^{x} \frac{\tau_w}{\rho} dx \tag{3.9}$$

$$= M_r - \int_{x_r}^{x} \frac{\tau_w}{\rho} dx. \tag{3.10}$$

$$\text{Therefore } M_j = M_r - M_\tau, \tag{3.11}$$

$$\text{where } M_\tau = \int_{x_r}^{x} \frac{\tau_w}{\rho} dx. \tag{3.12}$$

$$\text{Therefore } \frac{M_j}{M_r} = 1 - \frac{M_\tau}{M_r}. \tag{3.13}$$

While calculating M_j using the present hot-wire measurements, the values of $\overline{W'^2}$ was neglected. M_τ was calculated by integrating the variation of the friction coefficient $C_{f_j} = 2U_\tau^2/V_j^2$ in the streamwise direction. Figure 3.6(a) shows this variation of C_{f_j} as a function of the streamwise distance. This curve was integrated over the specific streamwise distance ($x_r = 95b$ to x) to obtain the momentum loss from friction. Figure 3.6(b) shows the values of the two sides of Equation 3.12. Multiple runs were conducted at several x/b locations to obtain an estimate of the error. The largest values of the standard deviation associated with the current measurements are also presented in Figure **??**. It was clear that the momentum equation is satisfied

between x/b = 95 and 162. Hence, it is inferred that the current PWJ is sufficiently two-dimensional between these streamwise locations.

3.6 Calculation of the Friction Velocity (U_τ)

Researchers have used various techniques for measuring wall shear stress τ_w and subsequently the friction velocity u_τ in wall bounded flows. Klewicki (2007) has reviewed different techniques for measuring wall shear stress in detail, along with their limitations. Several of these techniques have been used to measure wall shear stress in PWJs. However, the accurate measurement of the wall shear stress remains a challenging task.

Wygnanski et al. (1992); Zhou et al. (1996) and Karlsson et al. (1992) used a linear relation between U^+ and z^+ in the viscous sublayer to measure U_τ. Eriksson et al. (1998) used a near-wall fit to the mean velocity profile to obtain U_τ. Abrahamsson et al. (1994) and Schober and Fernholz (2000) used Preston tubes to measure τ_w. Smith (2008) used a correlation between the skin friction and the local Reynolds number $Re_m = U_m\delta/\nu$ to obtain τ_w. George et al. (2000) gave a composite velocity profile in terms of a fifth order polynomial for the PWJ, i.e.,

$$\begin{aligned} U^+ &= \left(z^+ + c_4 z^{+4} + c_5 z^{+5}\right)\exp\left(-dz^{+6}\right) \\ &\quad + C_i z^{+\gamma}\left(1 + \gamma a^+ z^{+-1} + \frac{1}{2}\gamma(\gamma-1)a^{+2}z^{+-2}\right)\left(1 - \exp\left(-dz^{+6}\right)\right) \end{aligned} \tag{2.2}$$

Tachie et al. (2002, 2004) and Rostamy et al. (2011a,b) obtained U_τ by fitting this composite velocity profile to their measurements in the near-wall region of the PWJ;

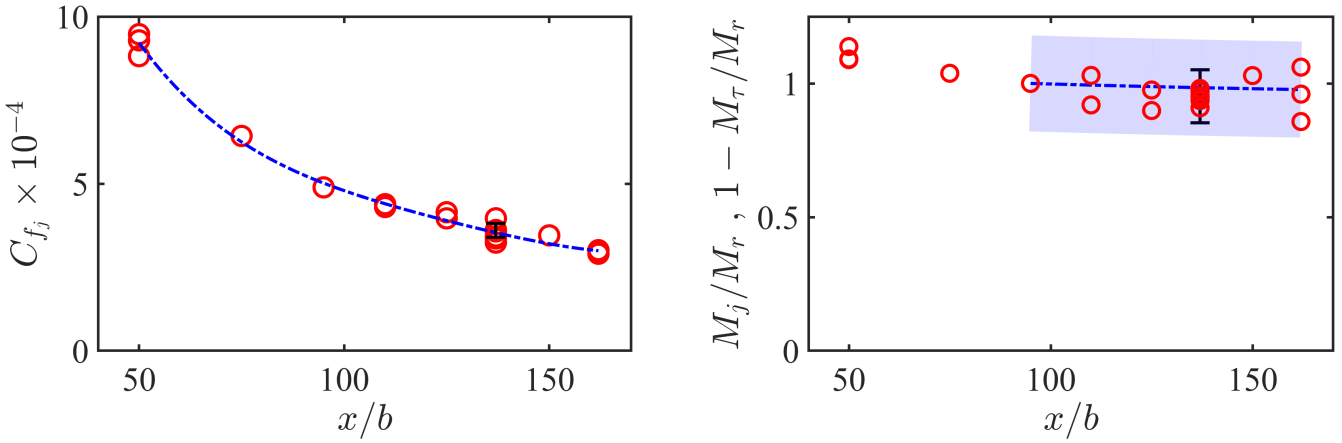

Figure 3.6. (a) C_{f_j} as a function of streamwise distance. Red circles (○) show current hot-wire data and blue line (-----) represents a 3$^{\text{rd}}$ order polynomial fit through the hot-wire data. The error bar shows (± one standard deviation) in the estimation of C_{f_j} at x/b = 137. (b) Momentum balance from equation 3.12. Red circles (○) represent the left-hand side of the equation 3.12 and blue line (-----) represents the right-hand side. Here, x_r/b = 95. The shaded area represents an estimation of the propagation error associated with the calculation of the ratio M_τ/M_r and the error bar shows the errors associated with the M_j/M_r calculation at x/b = 137.

see Figure 3.7. In the figure, the profile used $c_4 = 0.27 \times 10^{-3}$ and $c_5 = 13.6 \times 10^{-6}$, which are in agreement with the values in the literature (Eriksson et al., 1998; George et al., 2000; Bergstrom et al., 2001) and Tachie et al. (2002). The figure also shows a comparison with the near-wall mean velocity profiles of a zero pressure gradient boundary layer (Örlü and Schlatter, 2013), a fully developed channel flow (Lee and Moser, 2015) and the current PWJ measurements.

As seen in Figure 3.7, for $z^+ \lessapprox 10$, the profiles collapse well with each other. It can also be seen that the profiles follow a linear relation for $z^+ \lessapprox 3$. The current work uses this universality of the inner velocity profile to determine U_τ. Careful hot-wire measurements were conducted in the near-wall region of the PWJ and a sixth-order curve fit based on the velocity profiles of Figure 3.7 was used as a part of the least-squares fit to simultaneously solve for U_τ and $z = 0$. About 15 to 20 closely spaced points were used between $4 \lessapprox z^+ \lessapprox 10$ as part of the curve-fitting process. Points close to the wall ($z^+ < 4$) were ignored because of possible errors from conduction in the vicinity of the wall (Hutchins and Choi, 2002).

Figure 3.8 shows a comparison of the near-wall velocity profile of the current PWJ with that in the literature. As seen in the figure, the results are in good agreement. Hence, the near-wall curve-fitting approach is followed for calculating the friction velocity U_τ.

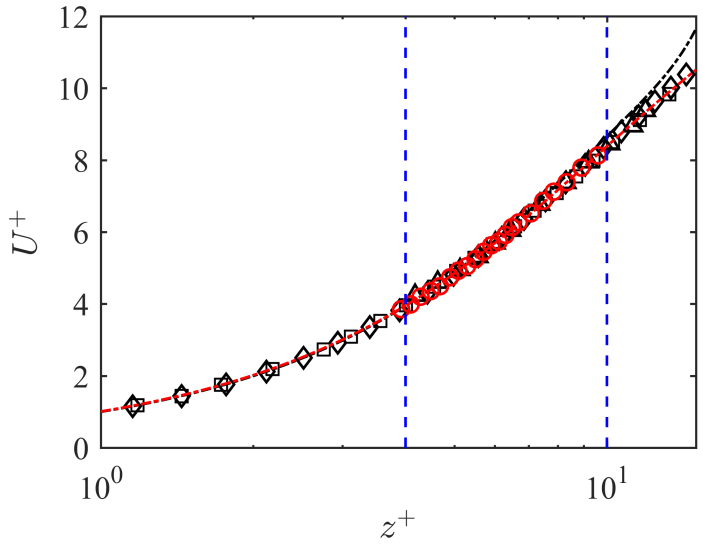

Figure 3.7. A comparison of the canonical velocity profiles with the current PWJ in near-wall region $z^+ < 10$. The line (-----) is the polynomial fit from (George et al., 2000) and the line (-----) shows the curve fit through all the different profiles. A comparison with measurements reported in the literature is also shown. The corresponding symbols are listed below.

zero pressure gradient boundary layer at $Re_\tau \approx 1150$ (Örlü and Schlatter, 2013) △
PWJ DNS at $Re_\tau = 2000$ (Ahlman et al., 2009) □
fully developed channel flow DNS at $Re_\tau = 2000$ (Lee and Moser, 2015) ◇
current PWJ measurements at $Re_\tau \approx 1250$ ○

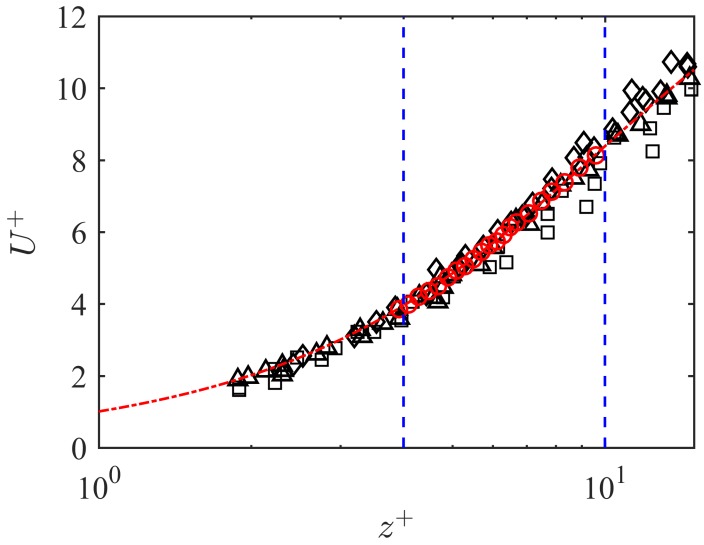

Figure 3.8. A comparison of the near-wall ($z^+ < 10$) velocity profiles from the literature with the current PWJ. The line (-----) shows the curve fit through all the near-wall measurements. A comparison with measurements reported in the literature is also shown. The corresponding symbols are listed below.

Eriksson et al. (1998) □
Karlsson et al. (1992) △
Tachie et al. (2002) ◇
current PWJ ○

4. Scaling of the Reduction in Friction Velocity

This chapter presents the near-wall response of the PWJ to a range of large-scale forcing. The reduction in the friction velocity ΔU_τ is considered as a function of the forcing and its dependency on the inner, outer as well as the global scales (PWJ exit characteristics) is discussed.

For this portion of the work, the measurements were divided into two sets, a near-all study and a detailed study. In the near-wall study, the PWJ was forced at twenty different frequencies ranging from 1 to 20 Hz and the corresponding effect on the friction velocity U_τ was measured at x/b = 110, 125, 137, 150 and 162. The measurements were conducted only in the near-wall region of the PWJ ($0 < z^+ \lessapprox 10$). Three large-scale forcing wavelengths were then chosen for a more detailed analyses of the forced PWJ at x/b = 50, 75, 110, 137 and 162. In this latter study, the measurements were conducted at wall-normal distance ranging from $0 < z \lessapprox 2.5\delta$ capturing the full wall-normal velocity profile. This study is referred to as the detailed study and is discussed at length in subsequent chapters.

Based on the PWJ exit conditions, the Strouhal number and forcing wavelengths associated with the forcing frequency f_f varied from $St = f_f b/V_j = 0.28 \times 10^{-3}$ to 5.7×10^{-3}, where f_f is the forcing frequency. The wavelength based on global variables (PWJ exit conditions, i.e., V_j and b) was $\lambda_j/b = V_j/f_f b = 0.18 \times 10^3$ to 3.5×10^3. These frequencies were chosen to target the large-scales of the flow. The large-scales within a PWJ shear layer are of the order of outer length scale δ.

To calculate the length scale corresponding to the forcing frequency, these forcing-scales are assumed to convect at the maximum mean velocity U_m. Thus, with the outer length scale and the outer velocity scale as the appropriate scales, using Taylor's hypothesis, the streamwise forcing wavelength in multiples of the unforced outer length scale δ^0 is defined as

$$\frac{\lambda_x^f}{\delta^0} = \frac{U_m}{f_f \delta^0}. \tag{4.1}$$

Here, the superscript '0' represents flow properties of the unforced flow at a given streamwise location. This notation will be used for the rest of this dissertation.

Table 4.1 lists the parameter λ_j and λ_x^f for all the forcing frequencies f_f considered in the near-wall study, as well as the detailed study at the various downstream locations. For both of these studies, the friction velocity U_τ was calculated by fitting a sixth-order polynomial to the near-wall velocity measurements between $4 \lessapprox z^+ \lessapprox 10$, as described in §3.6. The streamwise locations considered in these studies are listed in Table 4.2 along with the line styles used to represent them.

4.1 Reduction in Friction Velocity ΔU_τ

A reduction in U_τ was observed for all chosen forcing wavelengths. Figure 4.1 shows the percentage reduction in the friction velocity U_τ upon forcing as a function of Strouhal number ($St = f_f b/V_j$). The superscript '+' indicates non-dimensionalization with respect to the inner scales. With increase in the Strouhal number St, the reduction in U_τ (ΔU_τ) increases and reaches a clear maximum (most negative ΔU_τ) before decreasing again. This trend is observed at all the streamwise locations considered. It

Table 4.1.
Nominal forcing scales $\lambda_j = V_j/f_f$ or $\lambda_x^f = U_m^0/f_f$ with respect to the chosen forcing frequencies f_f and the flow length scales at different downstream locations. The superscript '†' indicates runs from the near-wall study whereas the outlined rows indicate forcing scales chosen for the detailed study of the PWJ discussed in Chapters 5 to 7. For the near-wall study, the outer variables from a full profile run are used to non-dimensionalize λ_x^f.

f_f	λ_j/b	St	λ_x^f/δ^0						
Hz		$\times 10^{-3}$	x/b = 50	75	110	125	137	150	162
1	3520	0.28	170.0	100.9	58.5 †	52.0 †	46.0 †	41.7 †	36.0 †
2	1760	0.57	85.0	50.4	29.3 †	26.0 †	23.0 †	20.8 †	18.0 †
3	1173	0.85	56.7	33.6	19.5 †	17.3 †	15.3 †	13.9 †	12.0 †
4	880	1.14	42.5	25.2	14.6 †	13.0 †	11.5 †	10.4 †	9.0 †
5	704	1.42	34.0	20.2	11.7 †	10.4 †	9.2 †	8.3 †	7.2 †
6	587	1.70	28.3	16.8	9.8 †	8.7 †	7.7 †	6.9 †	6.0 †
7	503	1.99	24.3	14.4	8.4 †	7.4 †	6.6 †	6.0 †	5.1 †
8	440	2.27	21.2	12.6	7.3 †	6.5 †	5.7 †	5.2 †	4.5 †
9	391	2.56	18.9	11.2	6.5 †	5.8 †	5.1 †	4.6 †	4.0 †
10	352	2.84	17.0	10.1	5.9 †	5.2 †	4.6 †	4.2 †	3.6 †
11	320	3.13	15.5	9.2	5.3 †	4.7 †	4.2 †	3.8 †	3.3 †
12	293	3.41	14.2	8.4	4.9 †	4.3 †	3.8 †	3.5 †	3.0 †
13	271	3.69	13.1	7.8	4.5 †	4.0 †	3.5 †	3.2 †	2.8 †
14	251	3.98	12.1	7.2	4.2 †	3.7 †	3.3 †	3.0 †	2.6 †
15	235	4.26	11.3	6.7	3.9 †	3.5 †	3.1 †	2.8 †	2.4 †
16	220	4.55	10.6	6.3	3.7 †	3.3 †	2.9 †	2.6 †	2.2 †
17	207	4.83	10.0	5.9	3.4 †	3.1 †	2.7 †	2.5 †	2.1 †
18	196	5.11	9.4	5.6	3.3 †	2.9 †	2.6 †	2.3 †	2.0 †
19	185	5.40	8.9	5.3	3.1 †	2.7 †	2.4 †	2.2 †	1.9 †
20	176	5.68	8.5	5.0	2.9 †	2.6 †	2.3 †	2.1 †	1.8 †

Table 4.2.
Symbols used in Chapter 4 plots for streamwise locations considered. Both near-wall study as well as the detailed study symbols are shown.

x/b	near-wall study		detailed study	
	first runs	repetition	first runs	repetition
50	-	-		
75	-	-		-
110				-
125		-	-	-
137		-		-
150		-	-	-
162		-		-

is also seen that ΔU_τ reaches the minimum value (maximum reduction) at a nominal Strouhal number of 3.4×10^{-3} for all the streamwise locations considered.

Figure 4.2 shows the variation of ΔU_τ with respect to the streamwise distance for the three forcing wavelengths chosen for the detailed study. No clear trend in variation of ΔU_τ as a function of streamwise distance is observed. As seen, the maximum decrease in U_τ corresponds to $\lambda_j/b \approx 295$ (f_f = 12 Hz) at all streamwise locations and varied between 6 – 10% between x/b = 50 and x/b = 162.

Based on the reduction in U_τ presented in Figure 4.1, three forcing wavelengths were chosen for the detailed study of the forced PWJ. These three forcing wavelengths are shown using vertical dashed lines in Figure 4.1.

The line (----) corresponds to $\lambda_j/b \approx 295$ which resulted in the maximum U_τ reduction for all the streamwise locations considered. Along with the $\lambda_j/b \approx 295$

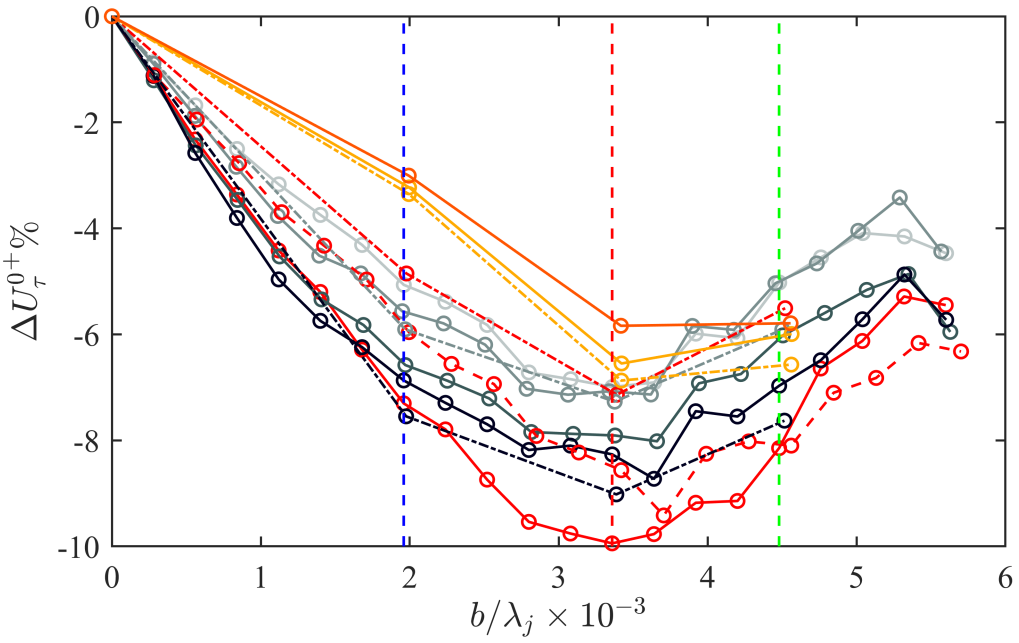

Figure 4.1. The reduction in the friction velocity ΔU_τ as a function of the Strouhal number $St = b/\lambda_j$. For line style information refer to Table 4.2. The vertical dashed lines show the forcing frequencies f_f = 7 Hz corresponding to Case A (----), f_f = 12 Hz corresponding to Case B (----) and f_f = 16 Hz corresponding to Case C (----) respectively, chosen for the detailed study.

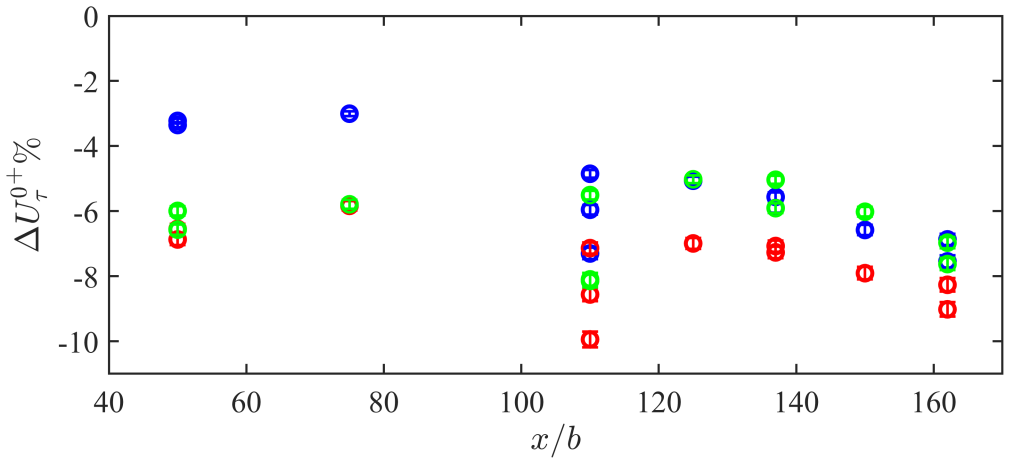

Figure 4.2. The ΔU_τ variation as a function of streamwise distance for f_f = 7 Hz corresponding to Case A (○), f_f = 12 Hz corresponding to Case B (○) and f_f = 16 Hz corresponding to Case C (○) respectively. The error bars are calculated using methods described in §3.5.1.

(f_f = 12 Hz), two other wavelengths, corresponding to $\lambda_j/b \approx 500$, f_f = 7Hz (- - - -) and $\lambda_j/b \approx 220$, f_f = 16Hz (- - - -) were chosen for the detailed study of the flow field. These forcing conditions are referred to as Case A ($\lambda_j/b \approx 500$, f_f = 7Hz), Case B ($\lambda_j/b \approx 295$, f_f = 12Hz) and Case C ($\lambda_j/b \approx 220$, f_f = 16Hz) respectively. The corresponding forcing scales λ_x^f are given in Table 4.1.

4.2 Scaling of ΔU_τ

The reduction in U_τ shown in Figure 4.1 appears to vary in a similar manner at all the streamwise locations considered. This suggests an underlying common scaling behavior. To further investigate this dependency, scaling in inner, outer, and global flow variables was considered. The global variables refer to the PWJ exit conditions, i.e., slot height b and exit velocity V_j. The lines and symbols used for representing these variations are same as the ones used in Figure 4.1 and listed in Table 4.2.

Figure 4.3 shows the variation of ΔU_τ with respect to the forcing wavelength λ_j when scaled using inner variables (ν/U_τ and U_τ). Here, ΔU_τ has been pre-multiplied by the forcing frequency (f_f) to obtain the reduction in U_τ per forcing cycle. This approach allows for comparison between forcing frequencies on a cycle average basis. Figure 4.3 shows that the curves follow an overall similar trend as noted previously. However, they appear to collapse for larger wavelengths up to a cut-off wavelength before diverging for smaller wavelengths. This result indicates a dependency on the inner variables and forcing scales up to a certain wavelength.

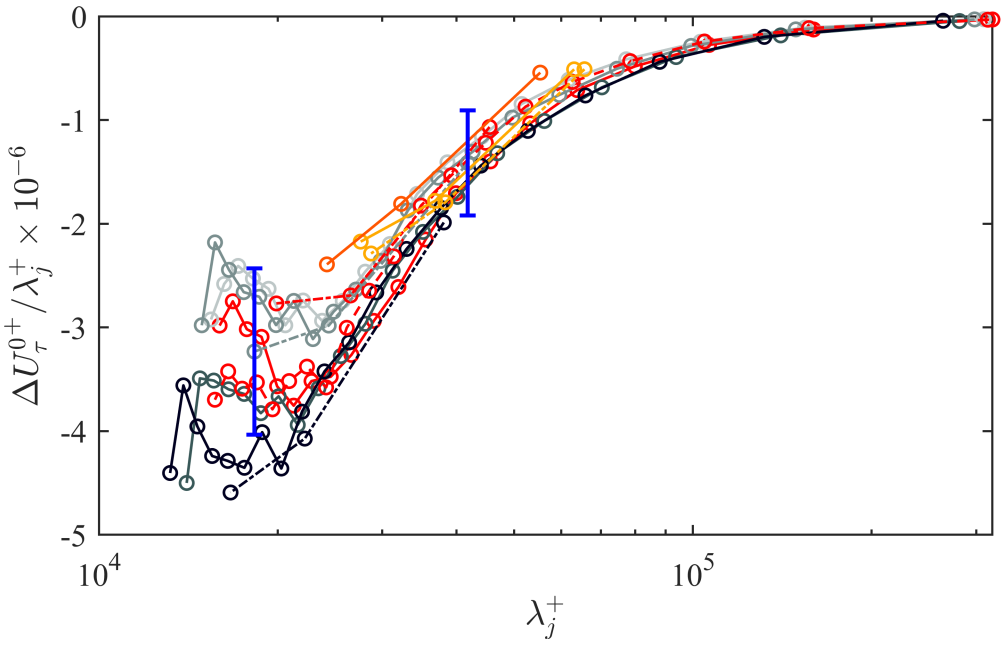

Figure 4.3. Pre-multiplied ΔU_τ variation with respect to the forcing wavelength λ_j when scaled with the inner variables. For line style information please refer to Table 4.2. The error bars represent the propagation error for forcing frequencies f_f = 7 Hz and f_f = 16 Hz at x/b = 137.

Figure 4.4 shows the variation of the pre-multiplied ΔU_τ with respect to the forcing wavelength λ_j when scaled with outer variables (δ and U_m). The outer variables used for the near-wall study are that of the full-profile measurements. Here, the curves can be seen to collapse within experimental error for all downstream locations ($x/b > 110$).

Figure 4.5 shows the variation of the pre-multiplied ΔU_τ with respect to the forcing wavelength λ_j when scaled with the global variables i.e. velocity scale V_j and length scale b. Figure 4.5 shows that the curves collapse well within experimental error for the most downstream locations ($x/b > 100$). This observation suggests that the flow is developing (or setting up/reacting to the forcing) when $x/b \leq 110$. After this streamwise location the flow shows a consistent scaling behavior.

The friction velocity U_τ is a scaled measure of the wall shear stress τ_w and hence, is directly linked with the mechanisms responsible for the shear force at the wall. The scaling dependence of ΔU_τ on inner variables suggests a direct relation with these mechanisms. In the outer region the flow is dominated by large-scales that scale with the outer length scale δ. The largest scales of the wall region (LSM and VLSM) also scale with the outer length scale δ. Thus, the outer scaling of ΔU_τ indicates a strong influence of the outer scales on the near-wall cycle in the case of the PWJ.

On one hand this type of mixed scaling suggests that the mechanism that is caused by the interaction between the outer scales ($\mathcal{O}(\delta)$) and inner small-scales ($\mathcal{O}(\nu/U_\tau)$) is responsible for the reduction in U_τ. On the other hand, the scaling behavior with respect to the global variables suggests that this mechanism also has a strong dependence on the PWJ exit Reynolds number.

With the observation that the scaling behavior points to an inner-outer interaction that is influenced by the forcing, a detailed study of this interaction is explored the subsequent chapters at three fixed forcing wavelengths.

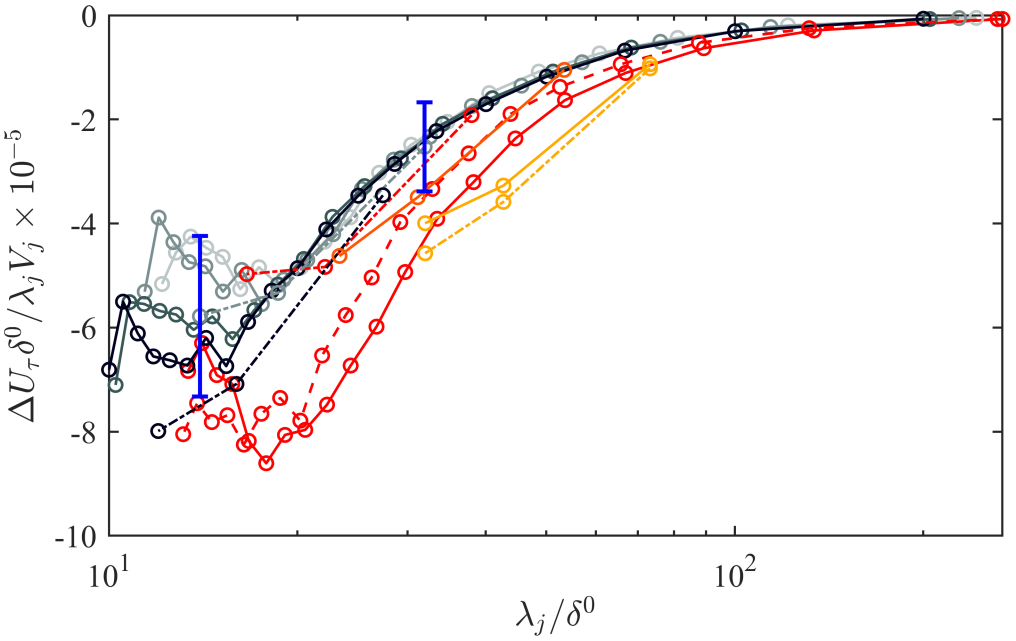

Figure 4.4. Pre-multiplied ΔU_τ variation with respect to the forcing wavelength λ_j when scaled with the outer variables. For specific line style information refer to Table 4.2. The error bars represent the propagation error for forcing frequencies f_f = 7 Hz and f_f = 16 Hz at x/b = 137.

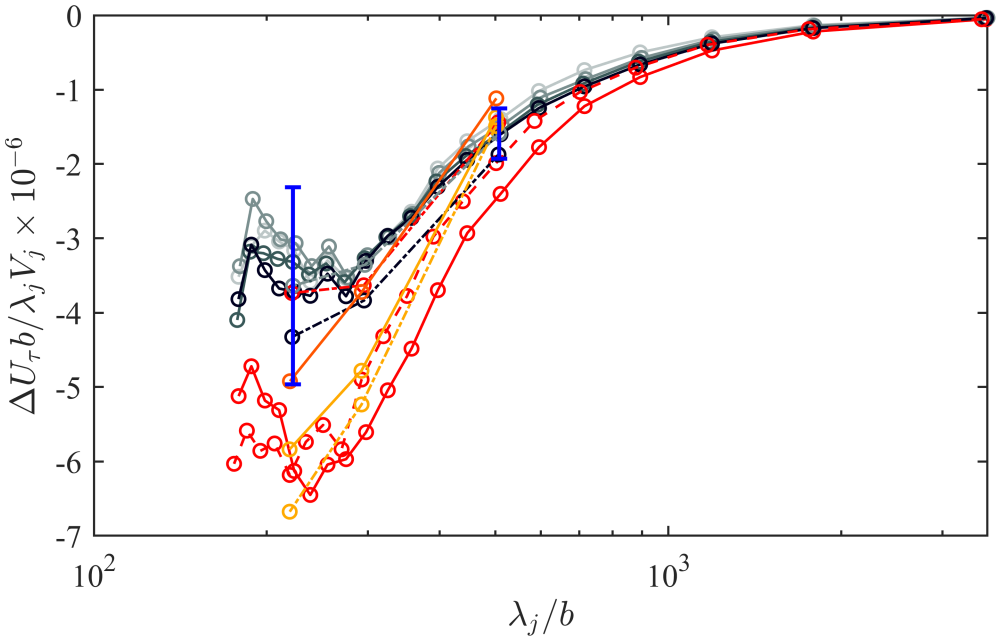

Figure 4.5. Pre-multiplied ΔU_τ variation with respect to the forcing wavelength λ_j when scaled with the global variables. For specific line style information please refer to Table 4.2. The error bars represent the propagation error for forcing frequencies f_f = 7 Hz and f_f = 16 Hz at x/b = 137.

5. Turbulence Statistics

Based on the observations made in the near-wall study, three forcing frequencies f_f = 7 Hz, 12 Hz and 16 Hz corresponding to $\lambda_j/b \approx 500$, 295 and 220, respectively, were chosen for a detailed investigation of the PWJ. From here on, the forcing corresponding to $\lambda_j/b \approx 500$ is referred to as Case A, $\lambda_j/b \approx 295$ is referred to as Case B and $\lambda_j/b \approx 220$ is referred to as Case C. The unforced flow is considered the baseline case.

This investigation was conducted at streamwise locations x/b = 50, 75, 110, 137 and 162. All three of the forcing wavelengths correspond to the large-scales of the flow at all streamwise locations therefore considered. The forcing wavelengths based on the outer velocity scale $\lambda_x^f = U_m^0/f_f$ ranged from $2.2\delta^0$ to $24.3\delta^0$ depending on the streamwise location. These parameters associated with each forcing case and streamwise location are listed in Table 5.1; this table also lists the corresponding change in U_τ (ΔU_τ). Here, Case B corresponding to $\lambda_j/b \approx 295$ (f_f = 12 Hz) forcing is responsible for the maximum reduction in U_τ at all streamwise locations that were considered.

While comparing the unforced and forced flows, Case B ($\lambda_j/b \approx 295$, f_f = 12 Hz) is used to discuss typical changes in the flow resulting because of the forcing. The discussion is then followed by a comparison accounting for Case A corresponding to $\lambda_j/b \approx 500$ (f_f = 7 Hz) and Case C corresponding to $\lambda_j/b \approx 220$ (f_f = 16 Hz). To aid in this comparison, the following line/symbol style conventions are followed (also listed in Table 5.1). Black lines and symbols are used to represent the baseline case,

Table 5.1.
Forcing wavelengths used for the detailed study of the PWJ and corresponding ΔU_τ reduction. Here, $\lambda_x^f = U_m/f_f$.

Case	f_f	x/b = 50		x/b = 75		x/b = 110		x/b = 137		x/b = 162		Line style
	Hz	λ_x^f	$-\Delta U_\tau$	λ_x^f	$-\Delta U_\tau$	λ_x^f	$-\Delta U_\tau$	λ_x^f	$-\Delta U_\tau$	λ_x^f	$-\Delta U_\tau$	
Baseline	0	-	0	-	0	-	0	-	0	-	0	
A	7	$24.3\delta^0$	3.30%	$14.3\delta^0$	3.00%	$8.4\delta^0$	4.89%	$6.6\delta^0$	5.72%	$5.1\delta^0$	7.27%	
B	12	$14.2\delta^0$	6.61%	$8.3\delta^0$	5.80%	$4.9\delta^0$	7.04%	$3.8\delta^0$	7.04%	$3\delta^0$	8.78%	
C	16	$10.6\delta^0$	6.10%	$6.2\delta^0$	5.75%	$3.7\delta^0$	5.43%	$2.9\delta^0$	5.71%	$2.2\delta^0$	7.53%	

i.e., the unforced quantities while blue, red and green lines and symbols are used to depict $\lambda_j/b \approx 500$ (Case A), 295 (Case B) and 220 (Case C), respectively, unless noted otherwise.

The current chapter discusses the turbulent statistics of the unforced and the forced flows. To conduct comparisons between various streamwise locations, most quantities are non-dimensionalized using the PWJ exit conditions, i.e., using the PWJ jet exit height b as the length scale and the nominal PWJ exit centerline velocity V_j as the velocity scale. Normalizations based on inner and outer scaling are also used where appropriate. The superscript 0 is used to indicate unforced quantities while the superscript '*' is used to indicate forced quantities.

5.1 Mean Velocity Profile

The PWJ has been shown to have a self-similar velocity profile past the initial transitional region (Wygnanski et al., 1992; Eriksson et al., 1998; Banyassady and Piomelli, 2014; Naqavi et al., 2018). A typical self-similar velocity profile for the unforced PWJ at $x/b = 50-162$ is shown in Figure 5.1. Also shown are the self-similar velocity profiles from various experiments in the literature. The plot shows profiles from Guitton and Newman (1977) at $Re_j = 30000$, Irwin (1973) at $Re_j = 28000$, Eriksson et al. (1998) at $Re_j = 9600$, Wygnanski et al. (1992) at $Re_j = 5000$ and 10000, and Tailland (1967) at $Re_j = 11000$. As seen, the unforced profiles at all the streamwise locations collapse onto each other as well as those found in the literature.

The data scatter in the outer region ($z/\delta > 1.3$) has been previously reported in the literature (Wygnanski et al., 1992; Naqavi et al., 2018).

The flow in this region is significantly affected by the entrainment conditions. This entrainment is governed by the PWJ exit geometry and possibly the boundary conditions. For example, some water-based facilities are influenced by the free surface (Eriksson et al., 1998). Also, the entrainment conditions of a PWJ with a sharp nozzle lip would be different from that of a blunt lip. Hence, this data scatter is generally associated with different entrainment conditions and nozzle geometries (Wygnanski et al., 1992; Banyassady and Piomelli, 2015; Naqavi et al., 2018). Nevertheless, it is suffice to say that the current PWJ unforced velocity profile is self-similar when scaled using outer variables.

Figure 5.2 compares the self-similar velocity profile of the unforced PWJ with that of the forced PWJ for Case B, in logarithmic coordinates at $x/b = 110$, 137 and 162. It is clear that the forcing results in a velocity profile that is still self-similar with identical outer scaling behavior as the unforced PWJ.

Figure 5.3 compares the unforced and Case B velocity profiles non-dimensionalized with respect to the inner variables in logarithmic coordinates. As seen, the flow exhibits a limited logarithmic region for both the forced and unforced flows. The logarithmic region in a PWJ is described in the same manner as in turbulent boundary layers, i.e.,

$$U^+ = \frac{1}{\kappa} \log z^+ + A. \tag{5.1}$$

However, a significant amount of scatter in the values of the constants κ and A is seen in literature in the case of the PWJ. Banyassady and Piomelli (2015) have summarized this scatter; the reported values for the constant k varies from 0.41-0.6 whereas, A varies from 5.0-10.53. Some studies suggest dependence of A on the PWJ exit Reynolds number Re_j and local streamwise conditions such as U_m/U_τ (Banyassady and Piomelli, 2015; Guerra et al., 2005; Wygnanski et al., 1992; Naseem et al., 2009). For the current work, the value of κ = 0.59 for both the forced and unforced flows. The value of A varies based on the streamwise location and differs for the forced flow.

In Figure 5.2, the approximate wall-normal extent of the logarithmic region is highlighted (----). This logarithmic region was observed to increase in extent with increasing downstream distance. Refer to appendix B for inner and outer scaled velocity profiles for all forcing cases and streamwise locations considered.

Figure 5.4 shows the streamwise development of the mean velocity profiles for both the unforced and forced PWJ for Case B. In both cases, as the PWJ develops downstream the maximum mean velocity U_m decreases and the outer length scale δ increases. At a fixed streamwise location, the effect of forcing itself is to reduce the outer velocity scale which is the maximum mean velocity U_m, while the the outer length scale δ is increased. It is noted that this decrease is U_m is accompanied by the reduction in the inner velocity scale U_τ.

The mean velocity profiles for all forcing cases (Case A, B and C) are now considered. Figure 5.5(a) shows a comparison of the mean velocity profiles at x/b = 137

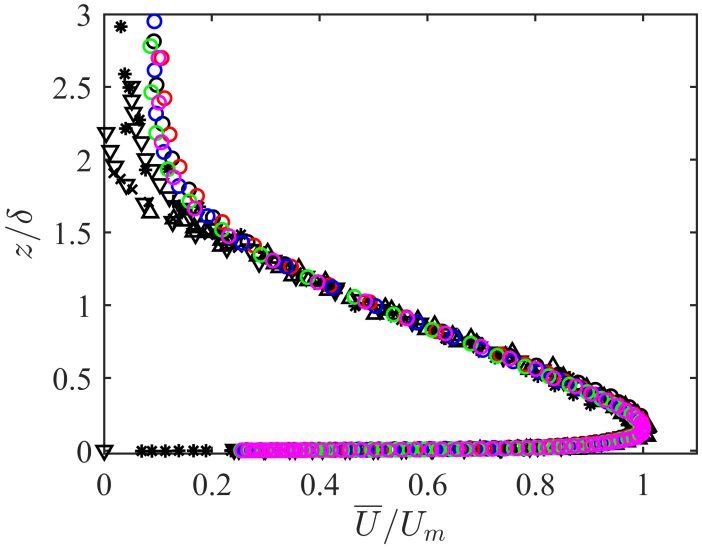

Figure 5.1. Self-similar velocity profile of the unforced PWJ and its comparison with the literature. Here, the circles show current unforced PWJ velocity profiles at x/b = 50 (○), 75 (○), 110 (○), 137 (○) and 162 (○). These profiles are compared with data from Guitton and Newman (1977)(+) at Re_j = 30000, Tailland (1967)(△) at Re_j = 11000, Irwin (1973)(×) at Re_j = 28000, Wygnanski et al. (1992)(▽) at Re_j = 5000 and 10000, and Eriksson et al. (1998)(∗) at Re_j = 9600.

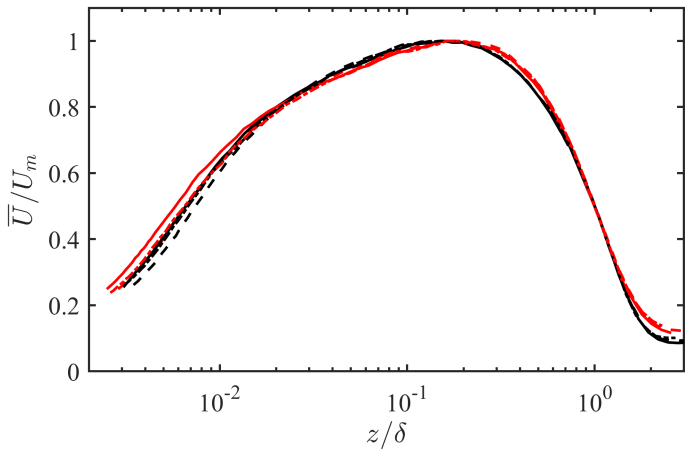

Figure 5.2. Self-similar velocity profiles in wall-normal logarithmic coordinates at x/b = 110 (- - - -), 137 (——) and 162 (-----) for the unforced (black) and Case B ($\lambda_j/b \approx 295$, red) conditions.

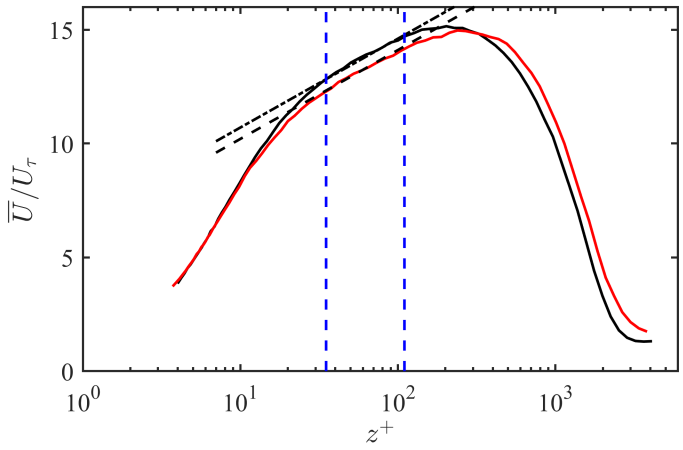

Figure 5.3. Velocity profiles non-dimensionalized using inner scales in wall-normal logarithmic coordinates at $x/b = 137$ for unforced (——) and Case B (——) flows. Also shown is the equations $U^+ = 1/0.59 \log z^+ + 6.8$ (- - - -) and $U^+ = 1/0.59 \log z^+ + 6.3$ (- - - -) indicating the logarithmic region of the flow in the unforced and forced flows respectively. The logarithmic region spans over $z^+ \approx 35 - 110$ (- - - -) for the unforced flow.

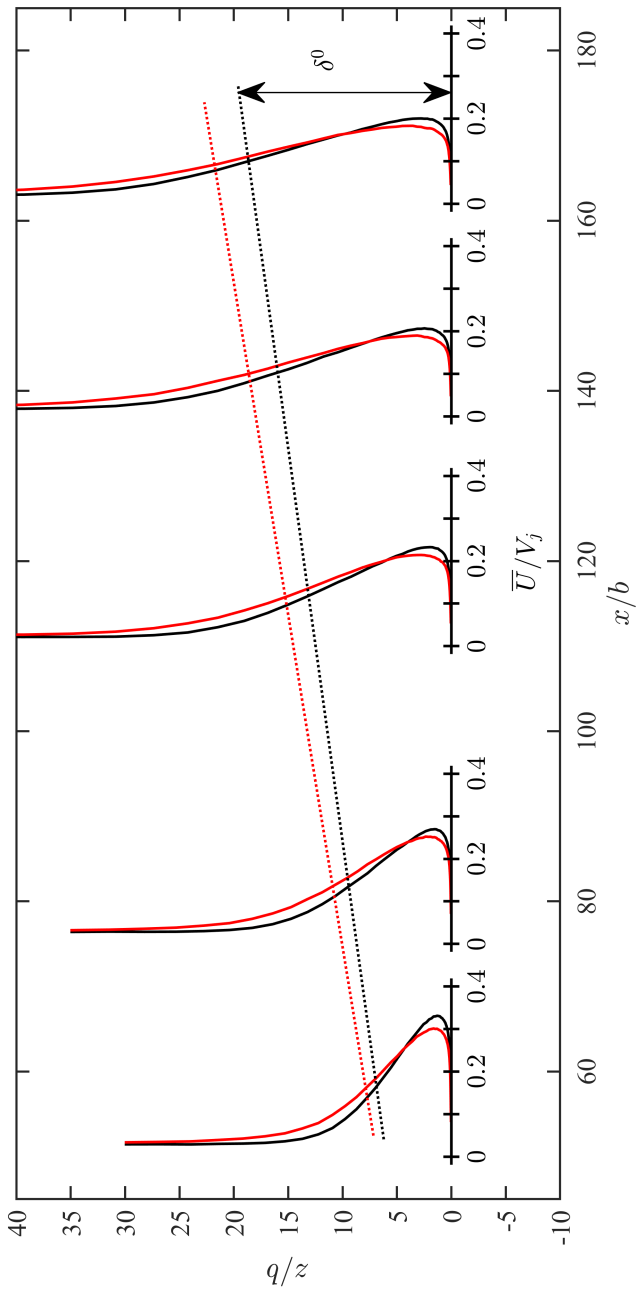

Figure 5.4. Comparison of the development of the PWJ self-similar velocity profiles (——) under unforced and forced conditions for Case B. Black lines and symbols are used to represent the unforced quantities while red lines and symbols are used for Case B ($\lambda_j/b \approx 295$) forcing. The development of the corresponding shear layer thickness δ (.....) is also shown.

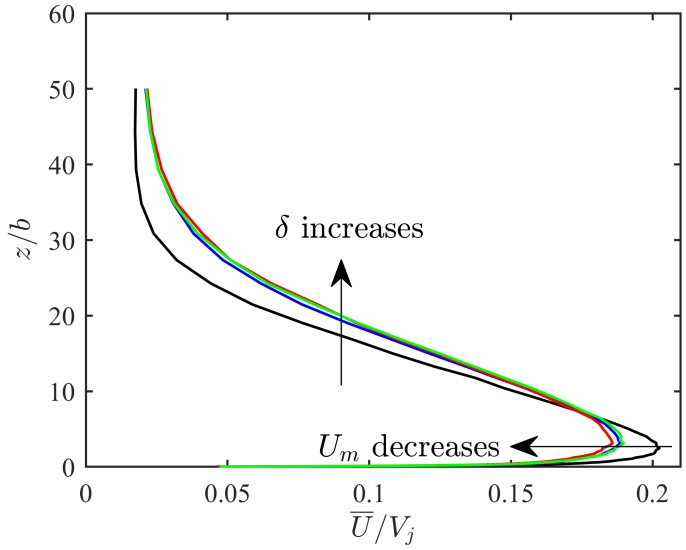

Figure 5.5. Mean velocity profiles non-dimensionalized with respect to global variables (b and V_j) at x/b = 137 for the unforced (——), Case A (——), Case B (——) and Case C (——) flows.

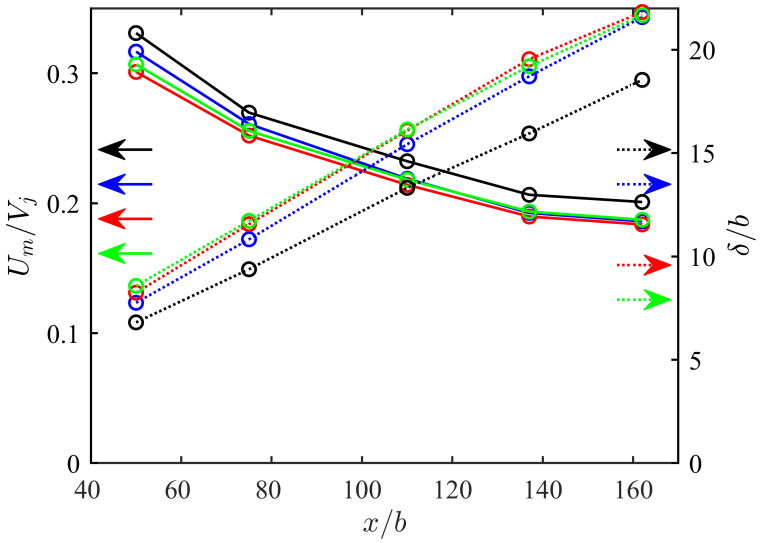

Figure 5.6. The variation of U_m (——) and δ (·····) as a function of the streamwise distance for the unforced (black), Case A (blue), Case B (red) and Case C (green) conditions.

for all forcing cases. It is seen that the maximum mean velocity U_m decreases for all forcing cases considered. The maximum reduction in the U_m is that for Case B (the red line). It is noted that Case B corresponds to the maximum reduction in U_τ. This decrease in U_m and increase in δ is observed at all streamwise locations and for all forcing wavelengths considered; see Figure 5.5(b). The results show the variation of the maximum mean velocity U_m and outer length scale δ as a function of the streamwise distance for the unforced and the forced flows. With increasing streamwise distance, U_m decreases and δ increases as a result of the development of the flow. At each streamwise location, U_m further reduces upon forcing whereas δ increases. The largest reduction in U_m corresponds to that of Case B at all streamwise locations considered. Incidentally, this is also the wavelength with maximum reduction in U_τ at all streamwise locations. The increase in δ upon forcing implies an increase in the the spreading rate of the PWJ. This outcome is also evident from the diverging lines of constant δ shown in figure 5.4. The spreading rate of the PWJ when forced, increased from $d\delta^0/dx \approx 0.1051$ for the unforced PWJ to $d\delta^*/dx \approx 0.1243$, 0.1230 and 0.1179 for Case A, B and C respectively. This outcome corresponds to an increase of 18%, 17% and 12% respectively.

5.2 Skin Friction Coefficient C_{f_j} and Momentum M_j

The skin friction coefficient based on the PWJ exit velocity V_j is given as, $C_{f_j} = 2U_\tau^2/V_j^2$. The streamwise variations of the skin friction coefficient C_{f_j} for the unforced flow and Case B ($\lambda_j/b \approx 295$) are shown in Figure 5.7(a). The forcing reduces the

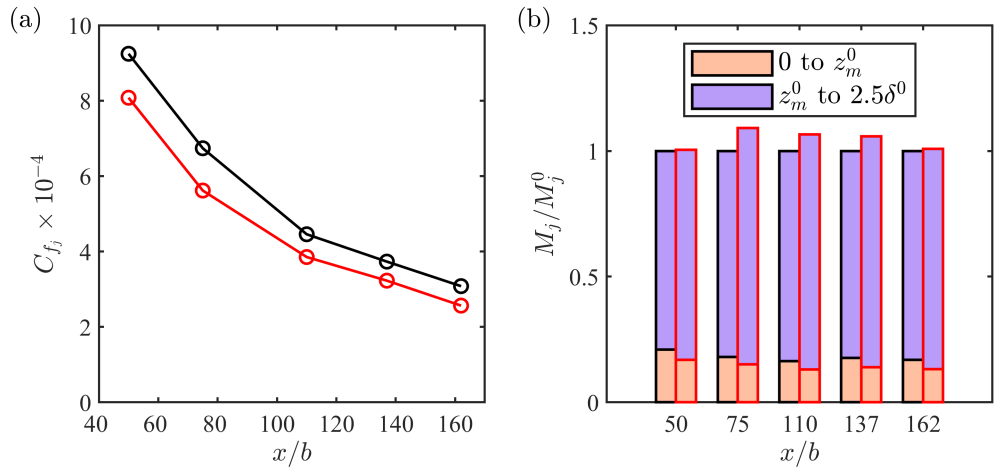

Figure 5.7. (a) Variation of the skin friction coefficient $C_{f_j} = 2U_\tau^2/V_j^2$ as a function of x/b. The unforced quantities are shown using black lines and symbols whereas the Case B ($\lambda_j/b \approx 295$) quantities are shown using red lines and symbols. (b) Variation of the momentum as a function of x/b decomposed into that corresponding to the inner ($z \leq z_m^0$) and the outer ($z > z_m^0$) region and non-dimensionalized with respect to the total unforced momentum M_j^0 as shown in Equation 3.8. Here, M_j indicates both unforced M_j^0 and forced M_j^* momentum for Case B ($\lambda_j/b \approx 295$).

friction coefficient at all streamwise locations considered. On average the reduction in C_{f_j} for Case B was $\approx 13.5\%$ across all streamwise locations.

Considering all forcing cases (Case A, B and C), the variation of C_{f_j} as a function of streamwise distance is shown in Figure 5.8. The forcing is seen to cause a reduction in C_{f_j} for all cases considered. Moreover, the maximum reduction in C_{f_j} corresponds to Case B, see Figure 5.8. The reduction in C_{f_j} combined with the increase in δ causes an increase in the local friction Reynolds number $Re_\tau = \delta U_\tau/\nu$ upon forcing. For instance, for the unforced PWJ at $x/b = 137$, then $Re_\tau \approx 1315$. Upon forcing, then Re_τ increases to 1446, 1489, 1484 for Case A, B and C respectively. Numerical values of the Re_τ at other streamwise locations are given in Table 3.2.

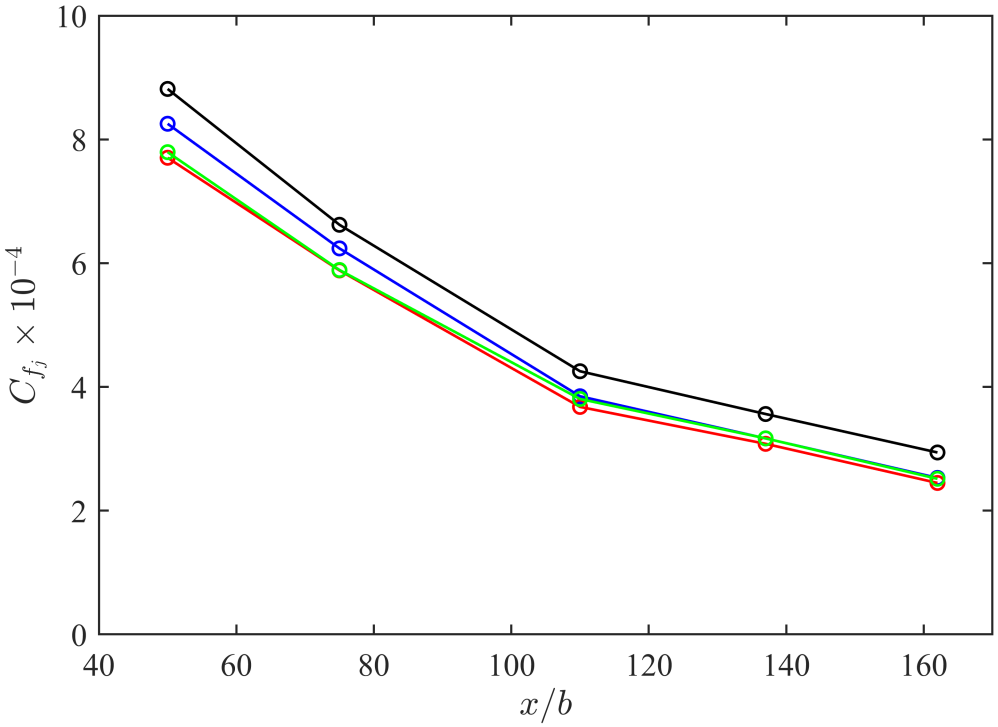

Figure 5.8. Variation of the skin friction coefficient $C_{f_j} = 2U_\tau^2/V_j^2$ as a function of x/b for all forcing scales. The color convention is given in Table 5.1.

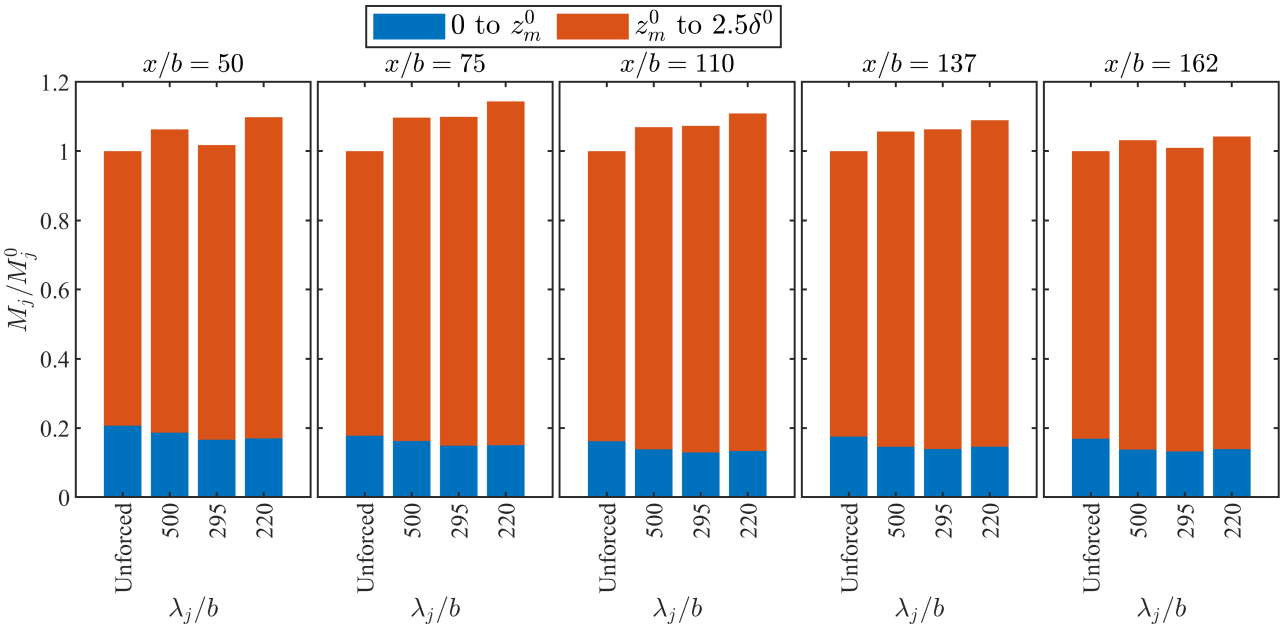

Figure 5.9. A comparison of the PWJ momentum M_j upon forcing decomposed into inner $z \leq z_m^0$ and outer ($z > z_m^0$) contributions for Case A ($\lambda_j/b \approx 500$), Case B ($\lambda_j/b \approx 295$) and Case C ($\lambda_j/b \approx 220$) at different streamwise locations normalized with respect to the total unforced momentum M_j^0. Here, M_j indicates both unforced M_j^0 and forced M_j^* momentum.

This reduction is C_{f_j} is also accompanied by a reduction in PWJ momentum M_j. At a given streamwise location the value of M_j is calculated using Equation 3.8, given previously, i.e.,

$$M_j = \int_0^{z_m^0} \overline{U}^2 dz + \int_{z_m^0}^{2.5\delta^0} \overline{U}^2 dz. \tag{3.8}$$

Where, z_m^0 is the wall-normal location of the outer velocity scale U_m^0 and is used to separate the contribution from the inner wall layer and the outer free-shear layer.

Figure 5.7(b) shows the PWJ momentum for the unforced flow and Case B ($\lambda_j/b \approx 295$) as a function of streamwise location. As stated, the total momentum is split into contributions from the inner wall layer ($z \leq z_m^0$) and the outer free-shear layer ($z > z_m^0$). It is clear that the forcing increases the PWJ momentum. The increased momentum reaches a maximum at $x/b = 75$ and gradually decreases as the flow develops further downstream. However, this increase in momentum occurs in the outer free-shear layer region ($z > z_m$). In contrast, the forcing reduces the momentum in the wall region ($z < z_m^0$) coincident with the decrease in U_m. It is noted here that z_m also increases upon forcing similar to the outer length scale δ.

These observations are true for all forcing cases considered (Case A: $\lambda_j/b \approx 500$, Case B: $\lambda_j/b \approx 295$ and Case C: $\lambda_j/b \approx 220$). Figure 5.9 shows a comparison of the PWJ momentum for all three forcing cases non-dimensionalized with respect to the unforced momentum at different streamwise locations. The total momentum is shown to increase for all forcing cases considered. However, the momentum in the inner region ($z < z_m^0$) decreases. Moreover, it is observed that the maximum reduction

in the inner momentum is for Case B, which corresponds to the maximum reduction in U_τ. One possible explanation for this decrease in the near-wall momentum is that the forcing enhances the turbulent transport of momentum away from the near-wall region into the outer free-shear layer. This effect decreases the near-wall momentum which will also occur when there is an increase in the entrainment of the external still (low momentum) fluid into the near-wall region. However, if there is large-scale mixing in the flow it is likely both these processes occur simultaneously, leading to a reduction in momentum in the near-wall region and subsequently a reduction in the skin friction.

5.3 Triple Decomposition of Velocity

The forcing response of the mean velocity is now considered. Because the imposed forcing is a periodic function, following past studies (Hussain and Reynolds, 1970; McKeon et al., 2018), the velocity field is triple decomposed into a mean velocity component $\overline{U}$, a periodic component U_f that is phase locked with the imposed forcing, and an unsteady fluctuating component U_f', i.e.,

$$U\left(z,t\right) = \overline{U\left(z\right)} + U_f\left(z,\theta_f\right) + U_f'\left(z,t\right). \tag{5.2}$$

Where, θ_f is the forcing period.

Figure 5.10 shows the periodic forcing response U_f for Case B ($\lambda_j/b \approx 295$, $f_f = 12$ Hz) forcing as a function of downstream distance. The periodic component

U_f captures the response at the fundamental forcing frequency f_f, which is the linear response of the PWJ to the forcing (McKeon et al., 2018). As a first observation, it is evident that the magnitude of these response structures (or modes) reduce with increasing downstream distance.

The periodic response of Case B ($\lambda_j/b \approx 295$) forcing at $x/b = 110$ is shown in Figure 5.11 to highlight key features. At this streamwise location, the periodic response has three distinct features (highlighted by the three arrows) that span the wall-normal region. In the region closest to the wall ($z \lessapprox 0.6\delta^0$) the response is a forward leaning (positive inclination angle) flow structure or mode. This response mode is "attached" to the wall in that its footprint extends down to the wall. This inner response mode also extends well past z_m^0, the location of the maximum local mean velocity U_m.

In the outer extremities of the flow ($z \gtrapprox 0.6\delta^0$), two other features are seen. The middle one of these response features extends to about $z \approx 1.5\delta^0$, while the other feature extends past $z \approx 1.5\delta^0$. The response flow feature spanning the wall-normal region $0.6 \lessapprox \delta^0 \lessapprox 1.5$ shows a negative inclination angle (backward leaning). At this streamwise location, the outermost feature has an inclination angle nearly aligned with the vertical.

Considering the streamwise evolution of these response modes shown in Figure 5.10, these three basic flow features are observed at all the streamwise locations. However, the relative phase between them changes with downstream location. The innermost flow feature has a constant forward inclination angle. The middle flow

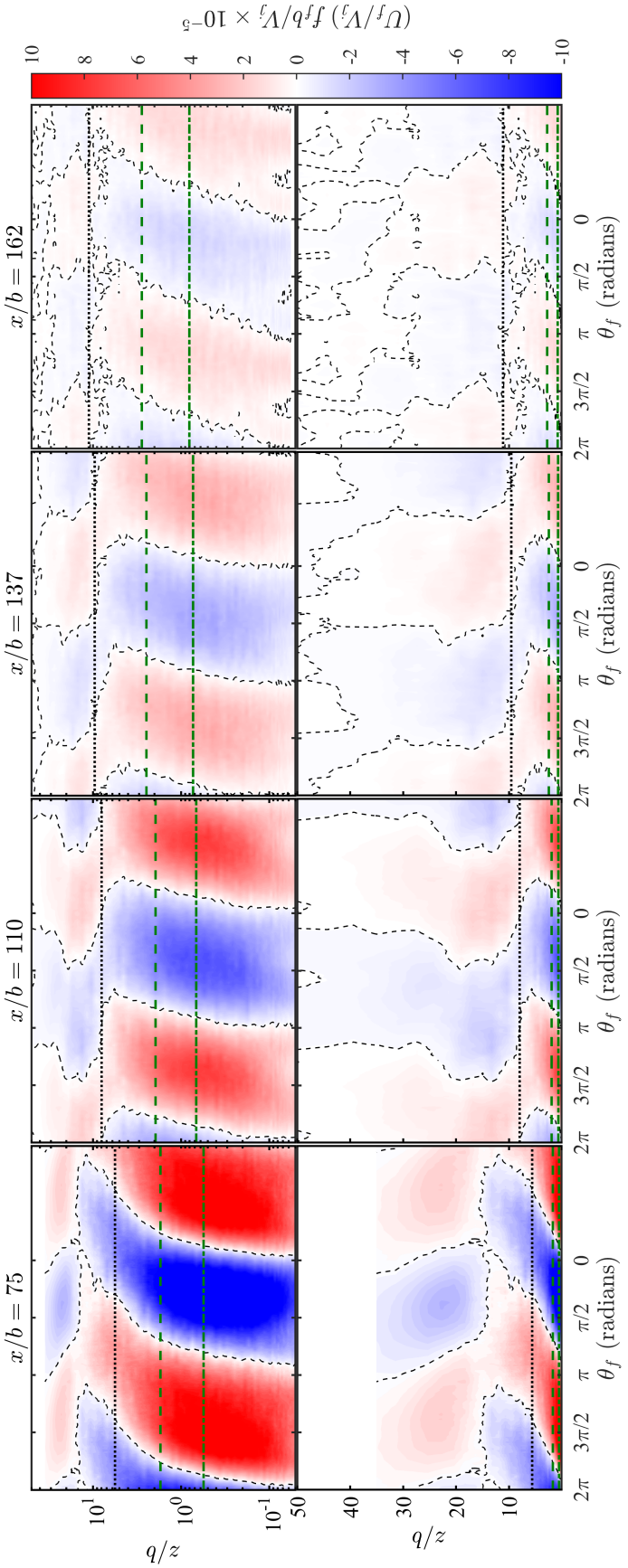

Figure 5.10. Variation of the mean periodic velocity U_f (see Equation 5.2) in logarithmic coordinates (top) and linear coordinates (bottom) for Case B ($\lambda_j/b \approx 295$, $f_f = 12$ Hz). The color represents the magnitude of U_f as indicated by the color bar on the right. The red regions indicate positive fluctuation whereas the blue regions indicate negative fluctuations. The line (- - - -) shows $U_f = 0$. The wall-normal locations $z^+ \approx 60$ (- - - -), $z \approx z_m^0$ (— · — ·) and $z \approx 0.6\delta^0$ (.....) are also shown.

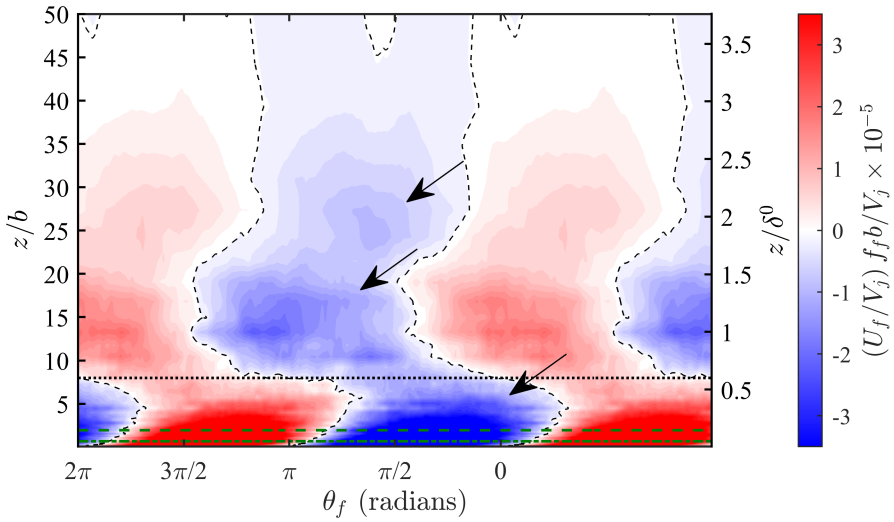

Figure 5.11. Variation of the mean periodic velocity U_f at x/b = 110 as shown in Figure 5.10. The contour line (----) shows U_f = 0. The wall-normal locations $z^+ \approx 60$ (----), $z \approx z_m^0$ (—·—) and $z \approx 0.6\delta^0$ (·····) are also shown. Arrows indicate three distinct periodic structures of the linear forcing response.

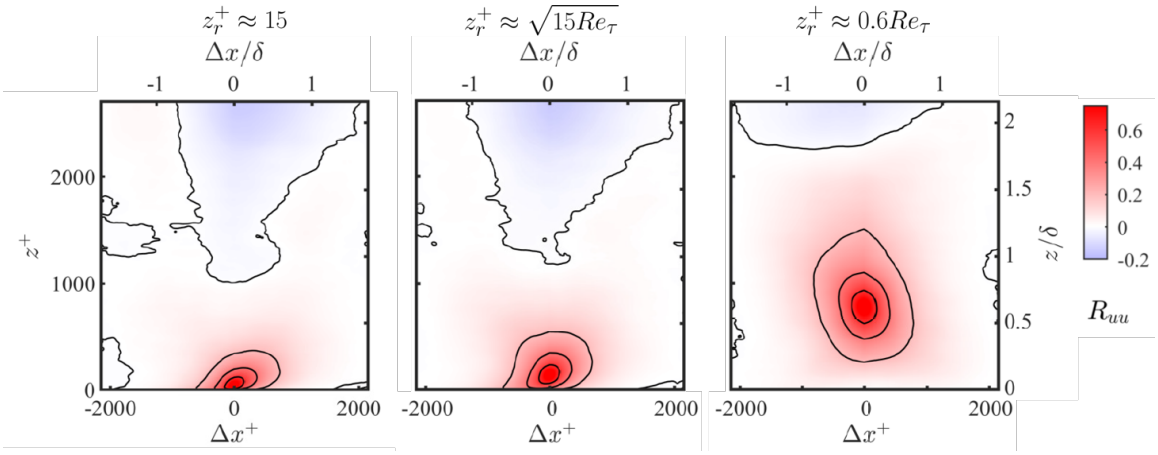

Figure 5.12. Two-point correlation $R_{uu}(\Delta x, z_r)$ in the wall-normal-streamwise plane from a particle image velocimetry measurement of Gnanamanickam et al. (2019).

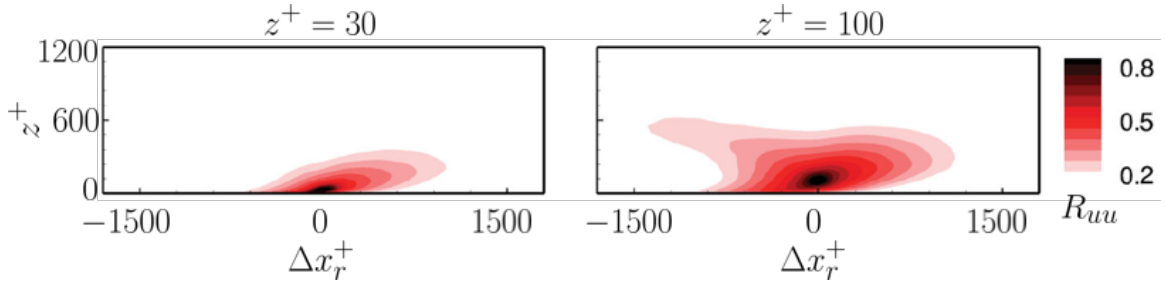

Figure 5.13. Two-point correlation $R_{uu}(\Delta x, z_r)$ in the wall-normal-streamwise plane from a large eddy simulation of Banyassady and Piomelli (2014).

feature shows a negative inclination angle at all streamwise locations. However, the outer most flow feature exhibits a small negative inclination angle at x/b = 75 and 110 and transitions into a flow feature with a small positive inclination angle at x/b = 162. At the most upstream streamwise location (x/b = 75), the two inner flow features also appear to be merged into a single flow feature.

The corresponding forcing response of the forced PWJ for Case A, B and C are now considered. Figures 5.14 and 5.15 show the corresponding forcing response for Case A ($\lambda_j/b \approx 500$) and Case C ($\lambda_j/b \approx 220$), respectively. For a proper comparison of all forcing cases the forcing cycles presented in Figure 5.10, 5.14 and 5.15 are pre-multiplied by the forcing frequency f_f. This procedure accounts for the fact that different forcing frequencies have different cycle periods and gives a cycle averaged measurement.

Considering Case A first (Figure 5.14), along with the linear response the flow also captures some of the non-linearities of the forcing in the form of higher harmonics at x/b = 75 and 110. The three basic flow features seen in Case B are also seen in Case A. The forward leaning structures near the wall appear to be merged with the middle structures at x/b = 75 and 110, whereas at x/b = 137 and 162 the three structures are distinct. The middle structure shows positive inclination at all streamwise locations. The outermost features appears to be backward leaning at x/b = 75 and 110, whereas slightly forward leaning at x/b = 137 and 162.

Considering Case C (Figure 5.15), the three structural features seen in this case retains the least coherence as the flow develops downstream when compared to Case

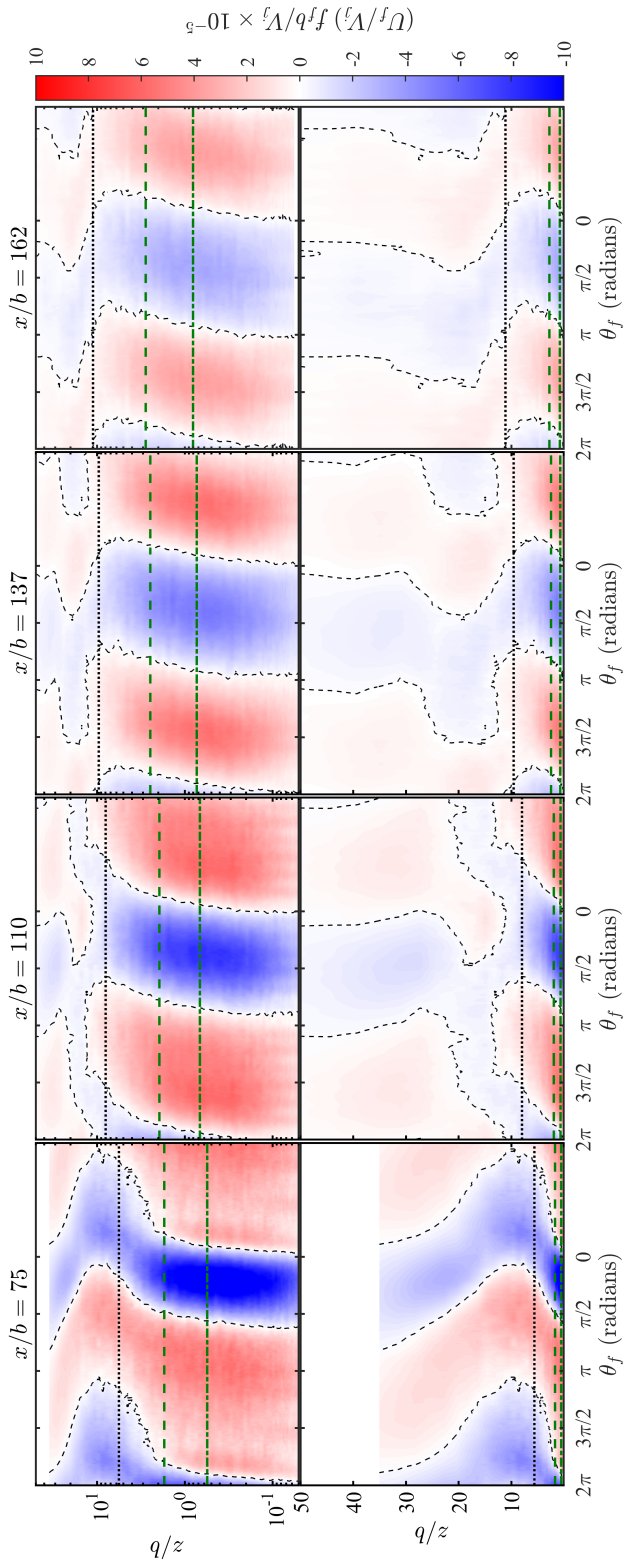

Figure 5.14. Variation of the mean periodic velocity in logarithmic coordinates (top) and linear coordinates (bottom) for Case A ($\lambda_j/b \approx 500$, f_f = 7 Hz). The color represents the magnitude of U_f as indicated by the color bar on the right. The red regions indicate positive fluctuation whereas the blue regions indicate negative fluctuations. The line (- - - -) shows U_f = 0. The wall-normal locations $z^+ \approx 60$ (- - - -), $z \approx z_m^0$ (—·—·) and $z \approx 0.6\delta^0$ (.....) are also shown.

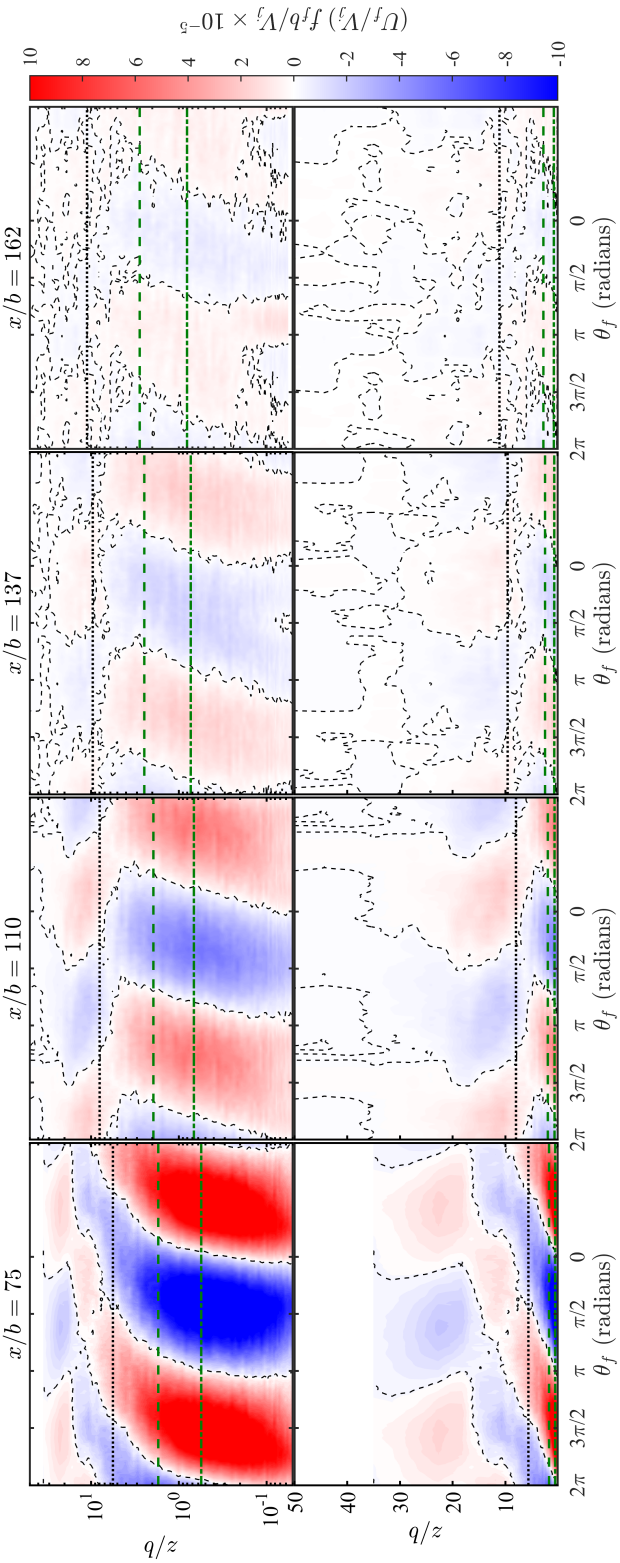

Figure 5.15. Variation of the mean periodic velocity U_f in logarithmic coordinates (top) and linear coordinates (bottom) for Case C ($\lambda_j/b \approx 220$, f_f = 16 Hz). The color represents the magnitude of U_f as indicated by the color bar on the right. The red regions indicate positive fluctuation whereas the blue regions indicate negative fluctuations. The line (- - - -) shows U_f = 0. The wall-normal locations $z^+ \approx 60$ (- - - -), $z \approx z_m^0$ (—·—·) and $z \approx 0.6\delta^0$ (.....) are also shown.

A and B. This outcome is because this corresponds to that with the smallest forcing frequency. The near-wall structures are forward leaning at all streamwise locations. However, at x/b = 162, past $z \approx 0.6\delta^0$, these structures loose their periodicity. Upstream of x/b = 162, the middle structure appears to be forward leaning at x/b = 75, whereas it is backward leaning at x/b = 110 and 137. The outer most structure appears to be backward leaning at x/b = 75, forward leaning at x/b = 110, and looses its coherence past this streamwise location.

Past studies (Banyassady and Piomelli, 2014, 2015; Gnanamanickam et al., 2019) have indicated that the unforced PWJ encapsulates flow features in the inner wall region that are forward leaning that are identical to those seen in canonical boundary layers. Hence, there simultaneously exists outer layer structures that share similarities to free-shear layer structures that are backward leaning (see Figures 5.12 and 5.13 for a comparison). This observation suggests that at least the two inner most linear response structures observed are two different flow structures. The phase shift observed with increasing downstream location would then indicate that these structures are convecting at different velocities.

As the PWJ shows increased entrainment upon forcing it is then possible that the outermost structure is the one responsible for the increased entrainment. However, because of the limitation of current single point hot-wire measurements, it is not possible to explicitly determine if these flow features are indeed two different structures. Recalling the forcing frequencies f_f associated with the forcing cases, Case A corresponds to 7 Hz, Case B corresponds to 12 Hz and Case C corresponds to 16 Hz. With

increasing forcing frequency f_f, the coherent structures that are introduced loses its energy to background turbulence at shorter streamwise distance, i.e., the shortest wavelength loses its coherence the fastest.

5.4 Turbulent Intensity

A typical streamwise turbulence intensity profile in the fully developed region (at $x/b = 137$) is shown in Figure 5.17(a). The streamwise turbulence intensity profile of the PWJ has two peaks: 1). The inner-peak in the near-wall region is associated with near-wall structures; 2). The outer peak is associated with the outer free-shear layer structures with some overlap of structures.

First Case B ($\lambda_j/b \approx 295$) is considered. The streamwise development of the streamwise turbulence intensity profiles for both the unforced flow and Case B is shown in Figure 5.16. The variation in magnitudes of the inner and outer peaks of the same are shown in Figure 5.17(b). As expected, both the peaks gradually reduce in the magnitude as the PWJ develops downstream in the cases of the forced and unforced PWJ. In the case of the unforced PWJ the inner peak is always smaller in magnitude than the outer peak for all streamwise locations considered. On average, the outer peak in the unforced PWJ is approximately 17.7% larger than the inner peak. However, in the case of the forced PWJ, the inner peak is higher in magnitude than the outer peak, i.e., the forcing increases the inner peak by $\approx$ 47.5% across all streamwise locations considered. There is also a slight but not as substantial

increase in the magnitude of the outer peak in the case of the forced PWJ for Case B (approximately 5.6% on average across all streamwise locations).

The total turbulence intensity profile indicates the turbulent activity integrated across all wavelength components. To obtain a clearer view of the forcing response, Figure 5.17 also shows the turbulence intensity profile at $x/b = 137$ decomposed into a large-scale and small-scale components. Here, large-scales are defined as those scales with streamwise wavelength $\lambda_x \geq 2\delta^0$, where Taylor's hypothesis is used to convert a velocity into a wavelength. On one hand, the large-scales are seen to be primarily responsible for the larger outer peak in the unforced PWJ. A peak in the small-scale intensity is also shown in the outer free-shear layer. On the other hand, in the inner wall layer there is a peak in both the large-scale and small-scale turbulence intensity. In the case of the unforced PWJ these two peaks contribute almost equally to the turbulence intensity, although the small-scale peak is located closer to the wall.

In the case of the forced PWJ, there is slight decrease in the inner peak of the small-scale turbulence intensity. However, there is an increase in the large-scale intensity across the entire layer. This increase is a maximum around the wall-normal location $z^+ \approx 60$ at all streamwise locations considered; this location lies within the logarithmic region of the mean velocity profile.

Forcing Case A, B and C are now considered together. Figure 5.18 compares the total turbulence intensity decomposed into the large-scale turbulence intensity and the small-scale turbulence intensity of the forced PWJ with the unforced flow. The forcing increases the total turbulence intensity of the flow primarily around the

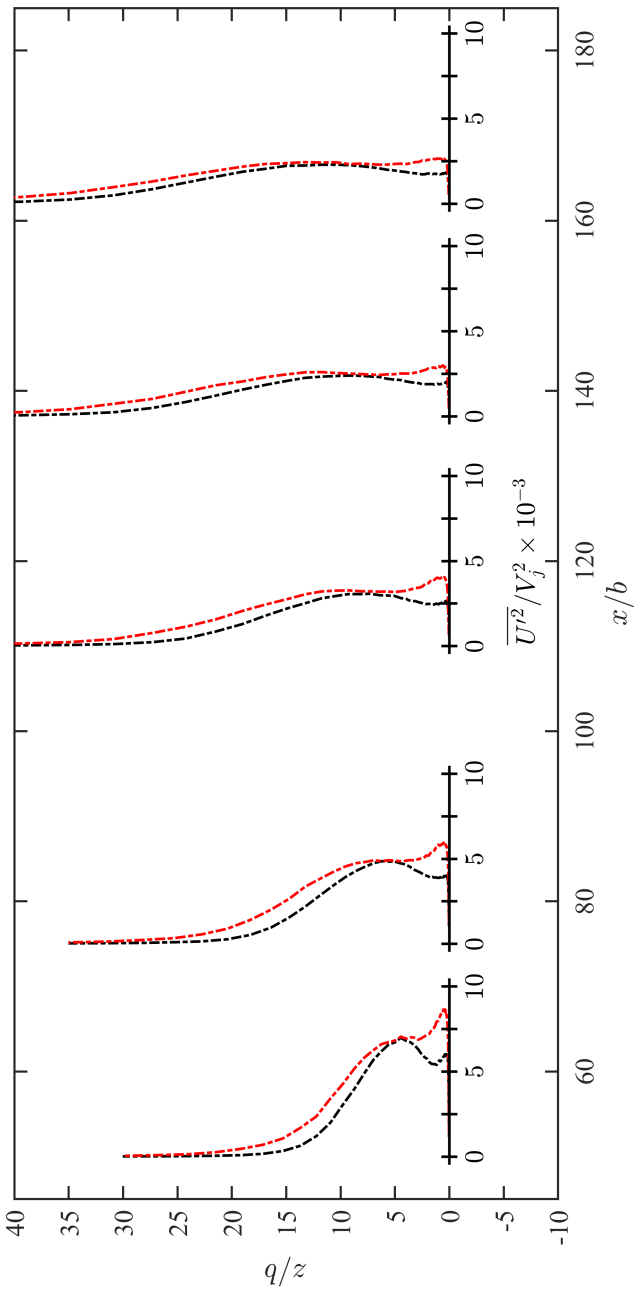

Figure 5.16. Streamwise development of the PWJ turbulence intensity profiles (- - - -) under unforced and forced conditions for Case B. Black lines are used to represent unforced quantities while red lines are used for Case B ($\lambda_j/b \approx 295$) forcing.

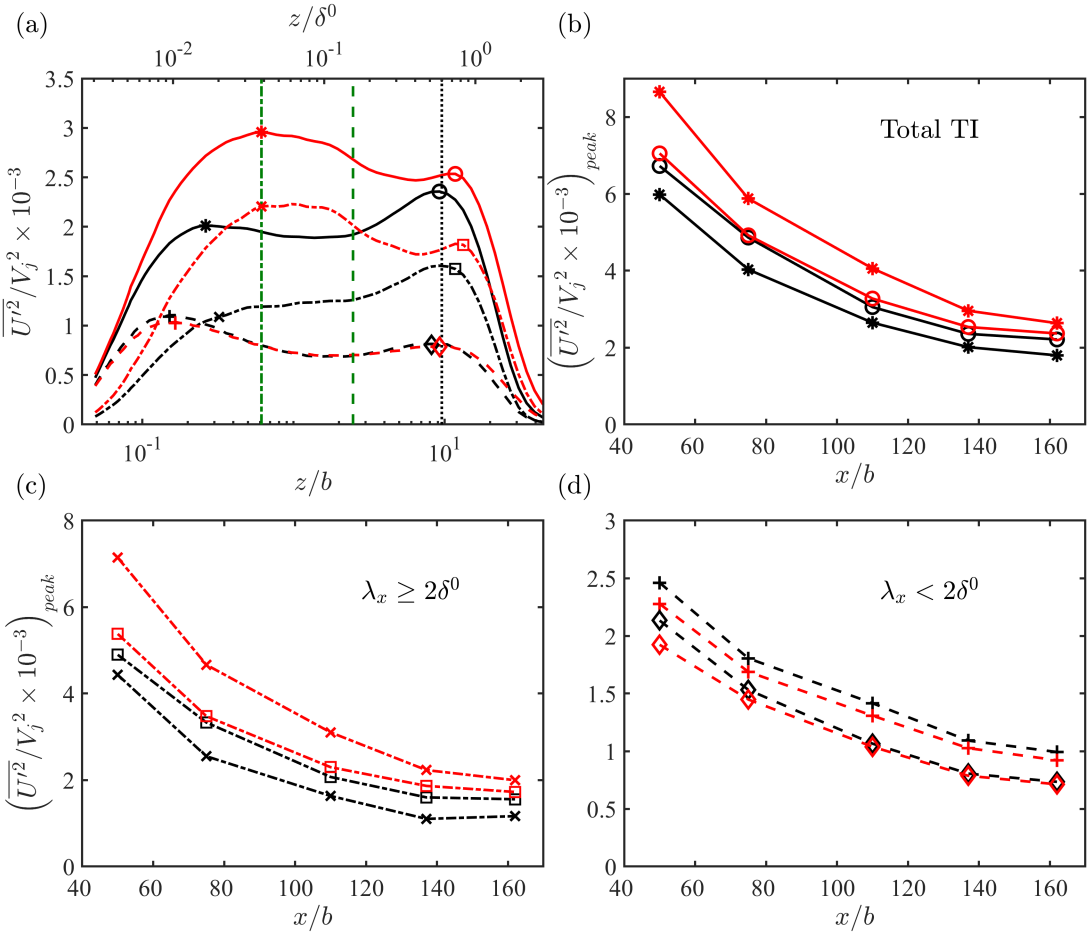

Figure 5.17. (a) Turbulence intensity (TI) profiles at x/b = 137 decomposed into a large-scale component ($\lambda_x \geq 2\delta^0$) and a small-scale component ($\lambda_x < 2\delta^0$). The lines (——) show the total turbulence intensity, the lines (- - - -) show large-scale component of the turbulence intensity and the lines (- - - -) show small-scale component of the turbulence intensity. The open symbols ✱ , × , + mark the location of the inner peaks and the closed symbols ○ , □ , ◇ mark the location of the outer peaks of the total turbulence intensity, large-scale turbulence intensity and small-scale turbulence intensity respectively. Also shown are the variation of the inner and outer peaks with respect to the streamwise distance for (b) total turbulence intensity peaks, (c) large-scale turbulence intensity peaks and (d) small-scale turbulence intensity peaks. While comparing forced and unforced quantities black lines and symbols are used to represent unforced quantities whereas red lines and symbols are used for Case B. The lines show wall-normal locations $z^+ \approx 60$ (—·—·—), $z \approx z_m^0$ (- - - -) and $z \approx 0.6\delta^0$ (·····) respectively.

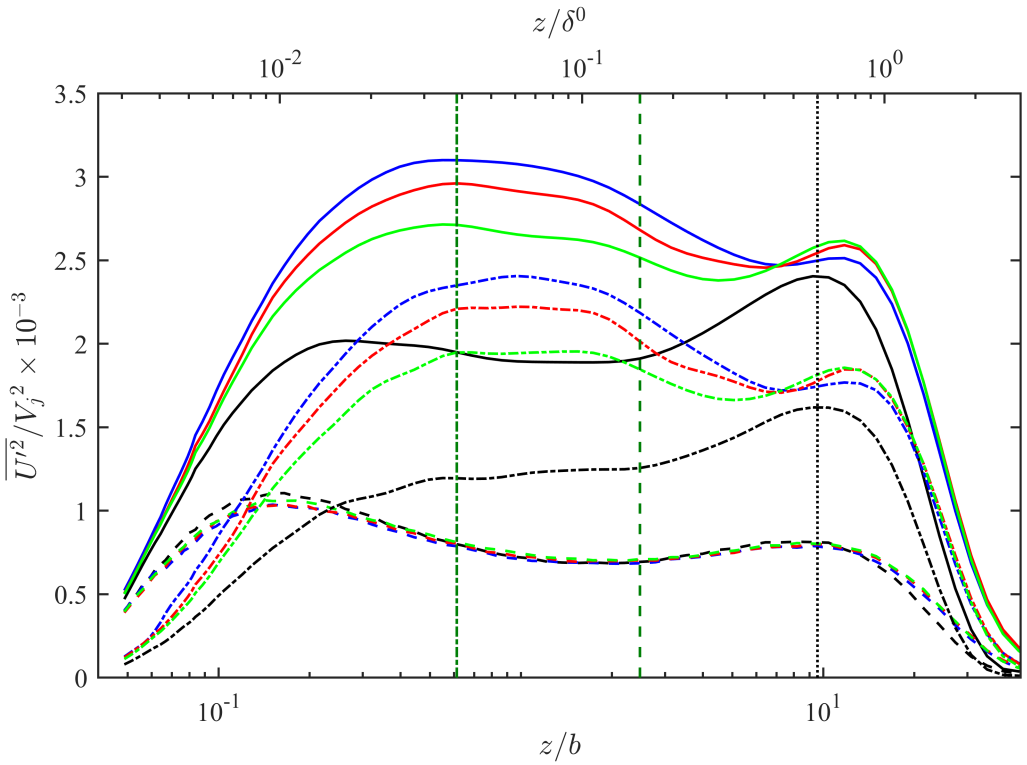

Figure 5.18. Turbulence intensity (——) profiles at x/b = 137 decomposed into large-scale components ($\lambda_x \geq 2\delta^0$, - - - -) and small-scale components ($\lambda_x < 2\delta^0$, - - - -) for unforced (black), Case A (blue), B (red) and C (green) respectively. The lines show wall-normal locations $z^+ \approx 60$ (—·—), $z \approx z_m^0$ (- - - -) and $z \approx 0.6\delta^0$ (·····) respectively.

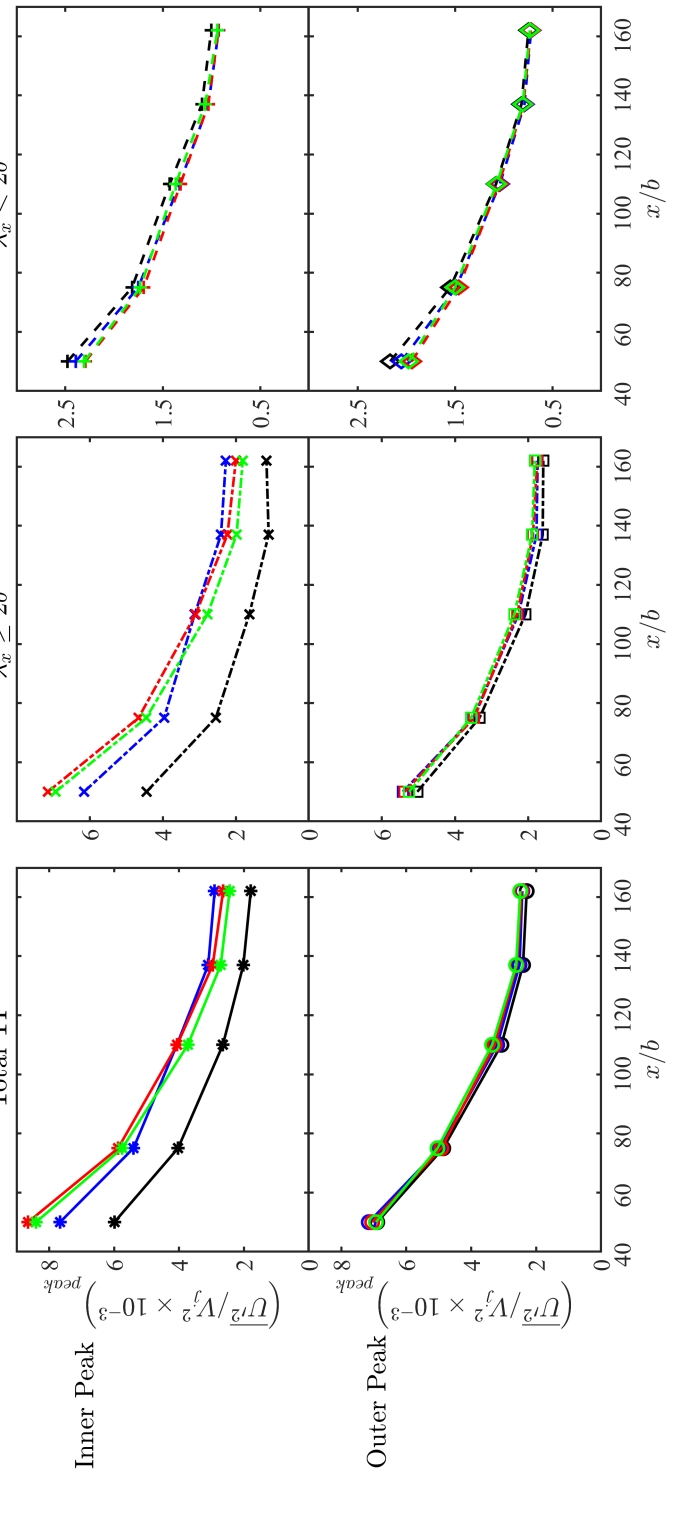

Figure 5.19. The variation of the inner (top) and outer (bottom) peaks with respect to streamwise distance. Shown are the total turbulence intensity peaks (left), large-scale turbulence intensity peaks (middle) and small-scale turbulence intensity peaks (right). The turbulence intensity corresponding to both the unforced as well as Case A, B and C are shown. Line style and color convention is as used in figure 5.17 and firgure 5.18.

inner peak. This increase corresponds to the large-scale turbulence intensity. The outer peak of the turbulence intensity also increases, however, not as substantially as the inner peak. The inner peak of the small-scale turbulence intensity reduces upon forcing.

The behavior of the forced PWJ at the streamwise location x/b = 137 is typical of all streamwise locations and forcing scales considered, and is not presented here in the interest of brevity. This decision is supported by the variation of the turbulence intensity peaks in Figure 5.19. Across all streamwise locations considered the large-scales contribute approximately 67% to the outer turbulence intensity peak and approximately 63% to the inner peak in the case of the unforced PWJ i.e., the large-scale make a larger contribution towards the outer peak. However, on one hand upon forcing, the large-scale contribution to the outer peak is approximately 71.8%, 72% and 72.5% for Case A, B and C forcing conditions, respectively. On the other hand in the case of the inner peak this contribution is approximately 77.3%, 77.9% and 76.3% for Case A, B and C forcing conditions, respectively.

5.5 Summary

A detailed study of the mean turbulence statistics of the PWJ when forced at three different forcing wavelengths was presented. The following is the summary of the observations:

- All of the forcing wavelengths caused a reduction in the friction velocity U_τ. The reduction was a maximum for Case B ($\lambda_j/b \approx 295$).

- The forcing also caused a reduction in the maximum mean velocity U_m. The maximum reduction in U_m corresponded to the case with maximum U_τ reduction, i.e., Case B, $\lambda_j/b \approx 295$.

- The forcing was observed to increase the spread rate ($d\delta/dx$) of the PWJ.

- The reduction in the values of U_τ and U_m were accompanied by the reduction in skin friction. This outcome caused a transfer of momentum from the inner region ($z \leq z_m^0$) to the outer region ($z > z_m^0$).

- The triple decomposition of the velocity revealed that the forcing introduces distinct periodic structures to the flow. In the near-wall region, these structures are forward leaning, whereas away from the wall their inclination varied with the streamwise distance and forcing wavelength. Moreover, these structures exhibit a phase difference with respect to each other in the wall-normal direction. This effect suggested that they travel at different convective velocities.

- The turbulence intensity was seen to increase upon forcing. This increase was significant in the logarithmic region of the PWJ, and was almost exclusively in the large-scales of the flow corresponding to the large-scales of the flow.

However, the turbulence intensity is an integral quantity. To get a better understanding of the scales associated with the flow physics, a spectra analysis is necessary and so is presented in the following chapter.

6. Energy Spectra

To get a clear insight into the energy transfer upon forcing, a spectral analyses of the unforced PWJ was compared to that of the forced PWJ. This chapter discusses this transfer of forcing energy in terms of the scale sizes. Case B corresponding to $\lambda_j/b \approx 295$ forcing is used as a representative forcing condition to compare the unforced and the forced flows.

Throughout this work three different wall-normal locations, at each streamwise location, are used to highlight key changes to the flow field. These wall-normal locations are $z^+ \approx 15$, $z^+ \approx 60$, and $z \approx 0.6\delta$. These locations estimated using unperturbed quantities are highlighted in the figures using lines as described in the caption of Figure 6.1.

For the remainder of this work the region around the wall-normal location $z^+ \approx 15$ is referred to as the near-wall region. Both the wall-normal locations $z^+ \approx 15$ and 60 are both less than z_m^0, the wall-normal location of the maximum mean velocity U_m^0. The wall-normal region that contains both these wall-normal locations, i.e., $z < z_m^0$, is referred to as the wall region or the inner region. The wall-normal region around $z \approx 0.6\delta^0$, for the remainder of this work, is then referred to as the outer region (for the outer free-shear region). To convert Fourier components f of the mean velocity field into a streamwise wavelength λ_x the outer velocity scale of the unforced PWJ is used, i.e., $\lambda_x = U_m^0/f$.

6.1 Spectra Comparison for Case B

The change in the PWJ upon forcing is first discussed for Case B ($\lambda_j/b \approx 295$) forcing condition. A comparison with all forcing cases (Case A and C) is then followed.

6.1.1 Forcing Spectral Response at $x/b = 50$

A sandpaper trip was used to trip the inner wall layer in both the case of the forced and unforced flow. Hence, the streamwise location $x/b = 50$ maybe considered as the "input" forcing location with respect to the further downstream locations from $x/b = 75$ to 162. This streamwise location $x/b = 50$, which is $24b$ downstream of the sandpaper trip is also past the initial PWJ development region, i.e., past this region the unforced flow may not be two dimensional.

The spectrograms of the unforced and Case B at $x/b = 50$ are shown in figure 6.1(a). Here, spectrogram refers to contour of the pre-multiplied, one-dimensional, streamwise power spectra $k_x\phi_{uu}$ as a function of wall-normal distance z/b and the inverse of streamwise flow frequency components V_j/fb such that

$$\int_0^\infty \phi_{uu} dk_x = \int_0^\infty k_x\phi_{uu} d(\log k_x) = \overline{U'^2}. \tag{6.1}$$

The energy ϕ_{uu} is pre-multiplied with respect to the streamwise wavenumber k_x as a consequence of plotting in the logarithmic coordinates (see Equation 6.1).

The differences between the two spectrograms are highlighted in the difference plot of Figure 6.1(c), while the differences at the three highlighted wall-normal locations

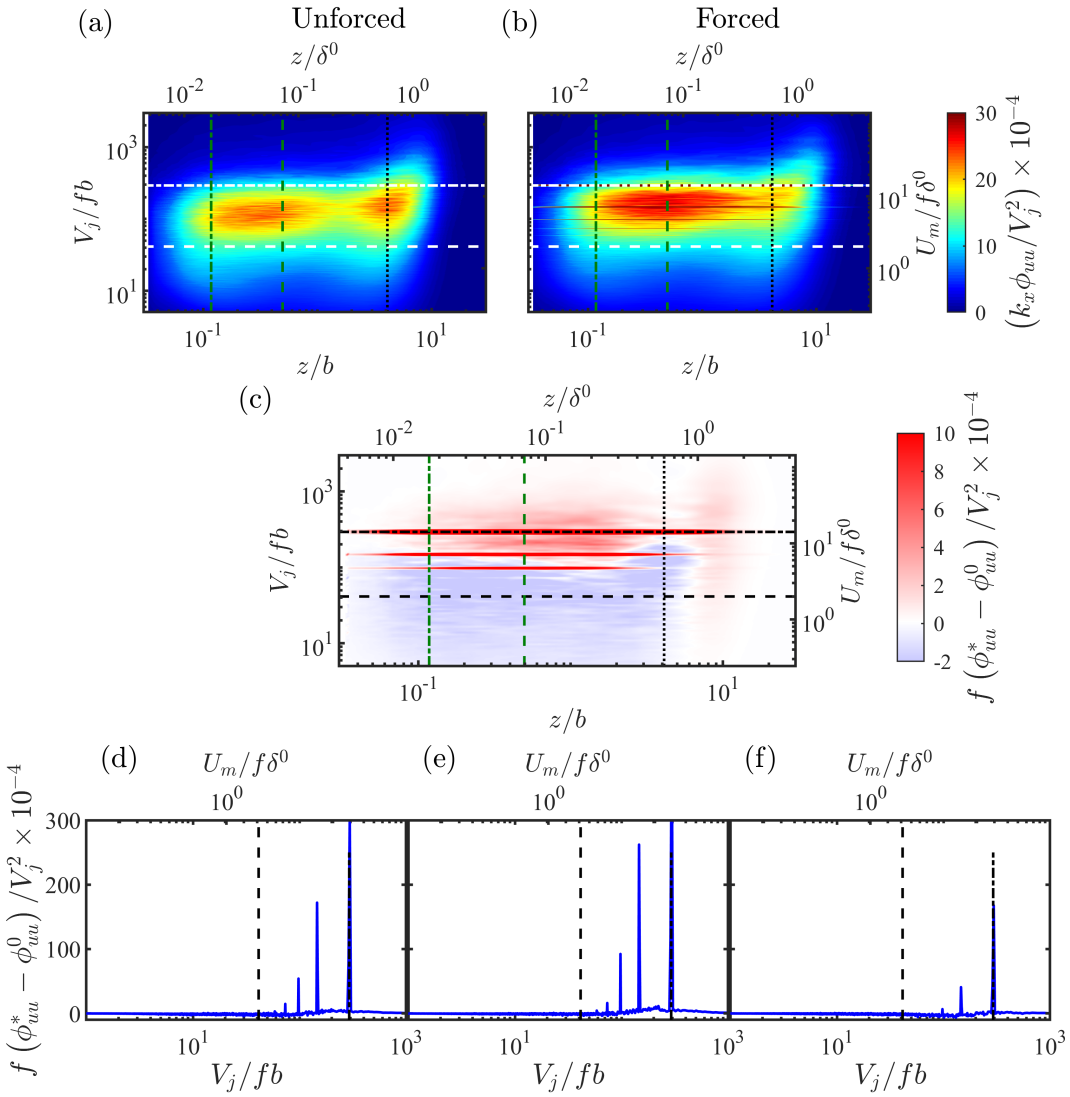

Figure 6.1. Pre-multiplied energy spectra at $x/b = 50$ for the (a) unforced, (b) forced flow and (c) the difference of the two. The lines show wall-normal locations $z^+ \approx 15$ (—·—·), 60 (- - - -) and $z \approx 0.6\delta^0$ (·····) respectively. Comparison of the difference in energy spectra at (c) $z^+ \approx 15$, (d) $z^+ \approx 60$ and (e) $z \approx 0.6\delta^0$. The cut-off wave length $\lambda_c = 2\delta^0$ (- - - -) separating the large-scales ($\lambda_x \geq 2\delta^0$) from the small-scales ($\lambda_x < 2\delta^0$) and the the forcing wavelength corresponding to Case B, $\lambda_j = V_j/f_f \approx 295b$ (-----) are also shown. Here, $f_f = 12$ Hz is the forcing frequency.

are presented in Figure 6.1(d), (e) and (f). On one hand, a peak in $k_x\phi_{uu}$ at the fundamental forcing frequency f_f = 12 Hz (Case B) as well as several higher harmonics can be observed. In the wall region ($z^+ \approx 15$ and 60) three harmonics are seen. On the other hand, in the outer region ($z \approx 0.6\delta^0$) only two harmonics are seen. Away from f_f and its harmonics, the results in Figure 6.1(c) shows that the forcing increases the energy of all flow scales in the outer extremities of the PWJ ($z \gtrapprox 0.6\delta^0$). In the wall region, the increase in energy is limited to scales larger than $V_j/fb > 10^2$ (or $\lambda_x = U_m/f > 6\delta^0$) while for smaller scales the forcing decreases the energy. These changes point to the introduction of large-scale transport within the PWJ by the forcing. The development of the forced flow for Case B and unforced PWJ is now compared at further downstream locations x/b = 75 to 162.

6.1.2 Energy Spectra

The streamwise spectral evolution of Case B (forced) and the unforced flow is shown in Figure 6.4 in the form of spectrograms. Line plots of the one-dimensional, pre-multiplied, streamwise energy spectra $k_x\phi_{uu}$ at the aforementioned three wall-normal locations $z^+ \approx 15$, $z^+ \approx 60$ and $z \approx 0.6\delta^0$ are shown in Figure 6.3 to aid in the discussion of the spectra.

The spectrograms of the unforced PWJ are first considered. To highlight key features, the unforced spectrogram at x/b = 137 is shown in Figure 6.2. It is noted that the features of the unforced PWJ discussed at x/b = 137 are exemplary of all other streamwise locations considered (see also the spectrogram of Figure 6.1(a)

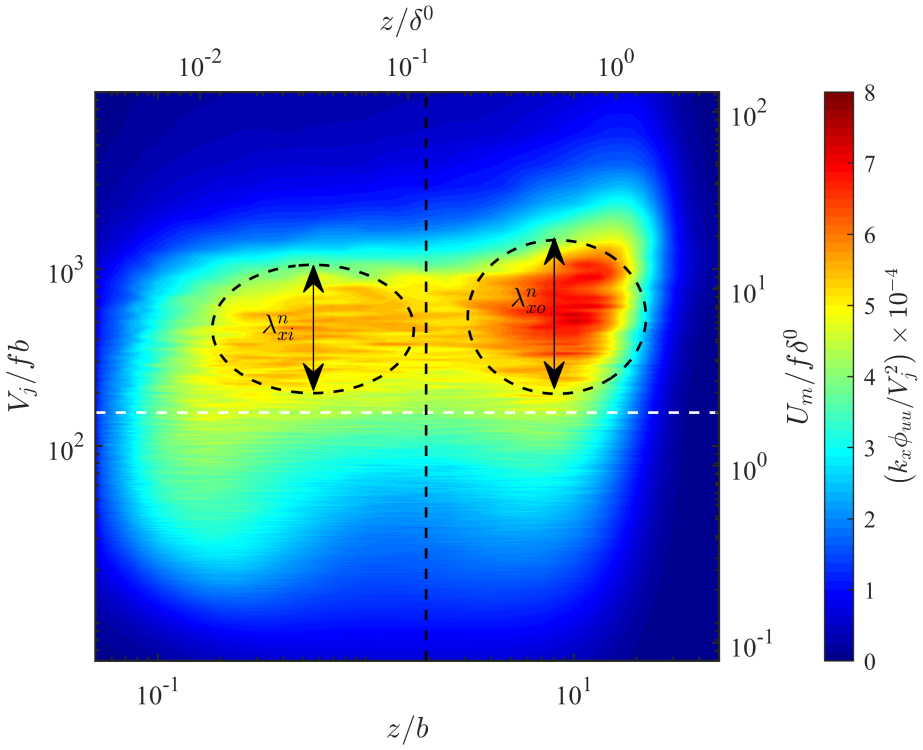

Figure 6.2. Pre-multiplied energy spectra at x/b = 137 for the unforced PWJ. The vertical line shows $z = z^0_m$ (----) whereas the horizontal lines show the cut-off wavelength $\lambda_c = 2\delta^0$ (white ----) respectively.

at $x/b = 50$). At all streamwise locations the PWJ encapsulates highly energetic large-scale structures ($\lambda_x \geq 2\delta^0$), which span the entire wall-normal extent of the PWJ. Notice, in Figure 6.4 and 6.3 a line (----) is used to highlight the spatial differentiator wavelength $\lambda_c = 2\delta^0$ at each streamwise location.

Though this large-scale energy resides at all wall-normal locations there is a concentration of large-scale energy at two wall-normal regions. These two regions are highlighted in Figure 6.2. The first of these regions lies between $z \approx 0.01\delta^0$ and $z \approx 0.12\delta^0$; these are the wall-normal locations spanning the limited logarithmic region of the inner wall layer as shown in Figure 5.3. This region lies below z_m^0, the wall-normal location of the maximum mean velocity U_m^0.

For the remainder of this work the large-scale wavelengths that reside in this first region are referred to as λ_{xi}^n, i.e., λ_{xi}^n represents the naturally occurring energetic large-scales that are observed in the PWJ between the wall-normal locations $0.01\delta^0 \lessapprox z \lessapprox 0.12\delta^0$. The second region where large-scale energy is concentrated is around the wall-normal location $z \approx 0.6\delta^0$.

This wall-normal location lies in the outer free-shear portion of the PWJ and for the remainder of this work these outer large-scale wavelengths are referred to as λ_{xo}^n. In case of the unforced PWJ, the concentration of energy is greater in this second outer region when compared with the inner region for all streamwise locations considered, i.e., the peak of λ_{xo}^n is larger in magnitude when compared to the peak of λ_{xi}^n. It must be emphasized that λ_{xo}^n and λ_{xi}^n are not single wavelengths but a range of energetic large-scale wavelengths, each with a peak that varies with wall-normal

distance (see Figure 6.2 and 6.3). It is also noted that in the case of the unforced flow λ_{xo}^{n} spans a wider wavelengths when compared to λ_{xi}^{n}.

The forced PWJ corresponding to Case B is now considered. It is observed that at x/b = 75 shown in Figure 6.3, apart from the linear response at the forcing frequency higher order harmonics are seen in the wall region at $z^{+} \approx 15$ and 60. With increasing downstream distance the non-linear, higher-order harmonic response dies out at all wall-normal locations. In the outer region ($z \approx 0.6\delta^{0}$) the higher harmonics have no energy. Notice also the linear response mode at the fundamental forcing frequency (f_f = 12 Hz for Case B). In the wall region at $z^{+} \approx 15$ and 60, the fundamental forcing frequency has significant energy at x/b = 75. This energy gradually decreases as the flow develops downstream and dies out at x/b = 162. In the outer region, there is very little energy at f_f at streamwise distances $x/b \geq 110$.

As the PWJ spreads in extent in the downstream direction, the naturally occurring energetic large-scales in both the inner region λ_{xi}^{n} and the outer region λ_{xo}^{n} are moving to larger and larger scales, i.e., they are getting larger because of the spreading of the PWJ. However, the forcing and its energetic linear response are at a single fixed wavelength λ_{x}^{f} for all streamwise locations.

The forcing scales λ_{x}^{f} (numerical values) corresponding to the detailed study are listed in Table 5.1. At the most upstream locations ($x/b \leq 75$), λ_{x}^{f} is larger than the peak in the naturally occurring large-scales in both the inner and outer regions (larger than λ_{xi}^{n} and λ_{xo}^{n}, respectively). As the PWJ develops further downstream, the fixed forcing wavelength λ_{x}^{f} (and its linear response at this fixed wavelength)

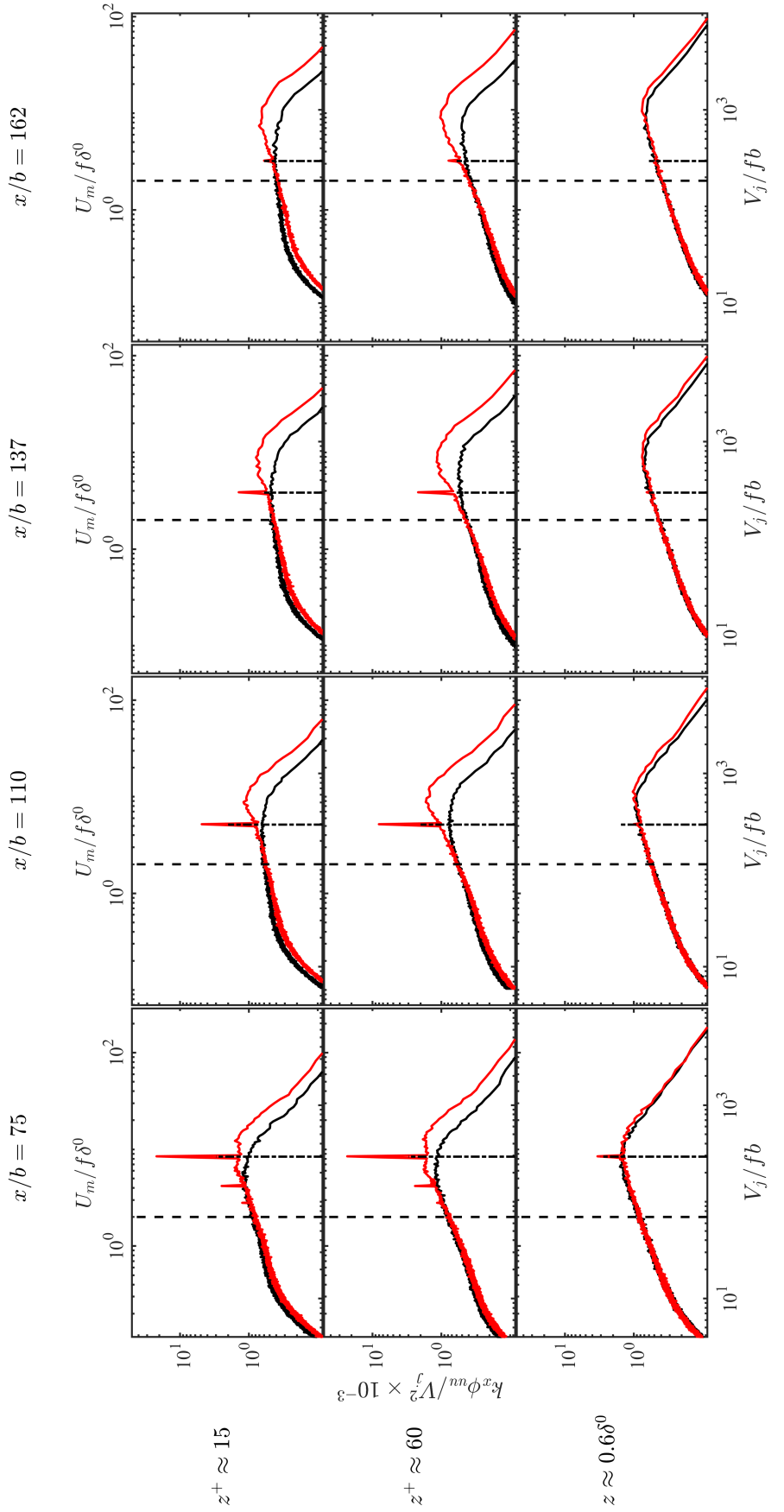

Figure 6.3. Comparison of PWJ pre-multiplied spectra $k_x\phi_{uu}/V_j^2$ (——) verses $V_j f/b$ at the near-wall locations z^+ = 15 (top), logarithmic location z^+ = 60 (middle) and outer location z = 0.6δ (bottom) respectively. The black color represents unforced flow and the red color represents forced flow conditions. The vertical lines show the cut-off wavelength $\lambda_c = 2\delta^0$ (- - - -) and the forcing wavelength $\lambda_j/b \approx 295$ for Case B (-----) respectively.

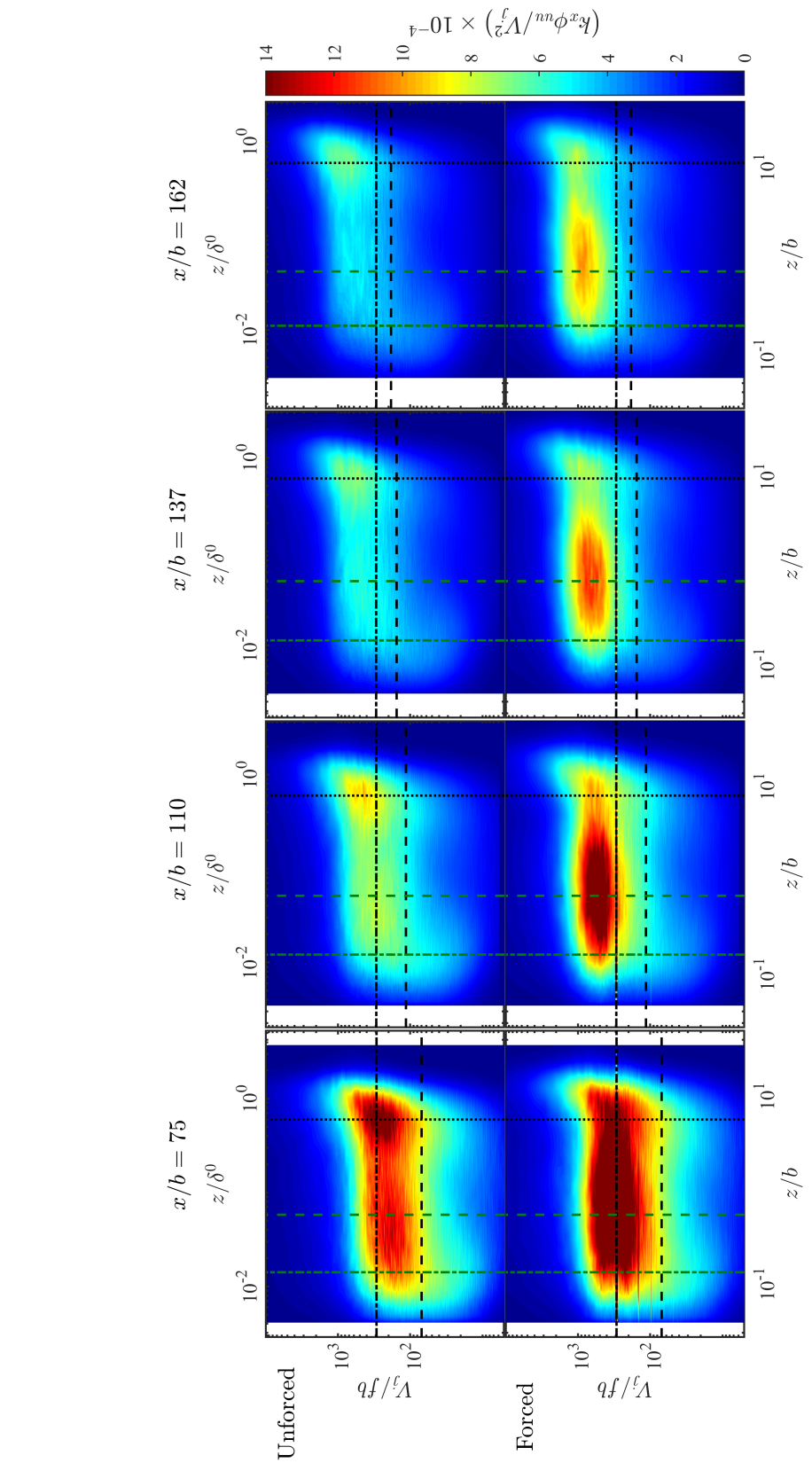

Figure 6.4. Comparison of contour maps of the stream-wise pre-multiplied energy spectra $k_x\phi_{uu}/V_j^2$ for the unforced (top) and Case B (bottom) conditions. The streamwise distance increases moving from left to right. The vertical lines show the wall-normal locations $z^+ \approx 15$ (-·-·-), $z^+ \approx 60$ (- - - -) and $z \approx 0.6\delta^0$ (.....) respectively. The horizontal lines show the cut-off wavelength $\lambda_c = 2\delta^0$ (-----) and the forcing wavelength $\lambda_j/b \approx 295$ for Case B (-----) respectively.

becomes equal to and then eventually smaller than the naturally occurring energetic large-scales of both the inner (λ_{xi}^n) and outer (λ_{xo}^n) regions. This transition occurs earlier in the outer region when compared to the inner region because the peak of the large-scale wavelengths in the outer region λ_{xo}^n is larger than the peak of the large-scale wavelengths in the wall region λ_{xi}^n.

This arrangement of the naturally occurring energetic large-scale relative to the forcing scale allows for an interesting energy transfer mechanism in the forced PWJ. Two difference plots are used to aid in this discussion. A comparison of the unforced flow with Case B at $\lambda_j/b \approx 295$ forcing is first discussed.

Figure 6.5 shows the difference between the spectrograms of the unforced flow and Case B forcing as a function of downstream distance. Figure 6.6 shows the difference between the spectrograms at a given streamwise location and the immediate upstream location. The line plots of pre-multiplied energy spectra at $z^+ \approx 15,\ 60$ and $z \approx 0.6\delta^0$ are shown in Figure 6.3. This representation allows for a visual comparisons of the relative scale sizes of the unforced flow and Case B forcing ($\lambda_j/b \approx 295$) at a given streamwise location.

The difference between Case B ($\lambda_j/b \approx 295$) and the unforced flow at a fixed streamwise location is first considered (Figure 6.5). It is observed that energy at the forcing wavelength λ_x^f is primarily transferred to the large-scales of the flow ($\lambda_x > 2\delta^0$) that reside at a specific wall-normal region. These recipient scales are seen to reside primarily in the logarithmic region of the PWJ. This outcome reinforces the observations of the turbulence intensity plot of figure 5.17(a) where the dominant increase in

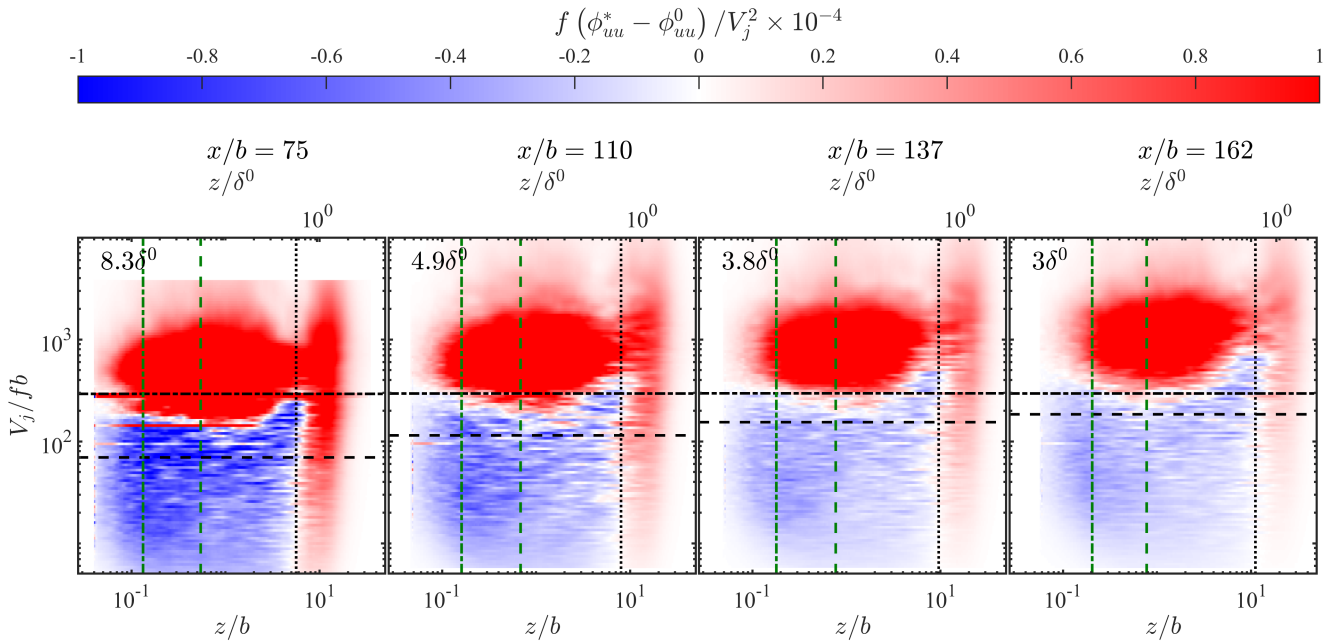

Figure 6.5. Change in pre-multiplied energy spectra ($f\left(\phi^*_{uu}-\phi^0_{uu}\right)/V_j^2$) for Case B ($\lambda_j/b\approx295$) as the flow develops downstream. The vertical lines show the wall-normal locations $z^+\approx15$ (—·—·), $z^+\approx60$ (- - - -) and $z\approx0.6\delta^0$ (·····) respectively. The cut-off wavelength $\lambda_c=2\delta^0$ (- - - -) and the forcing wavelength $\lambda_j/b\approx295$ for Case B (-----) are also shown. The number on the top left corner indicates corresponding forcing wavelength non-dimensionalized with respect to the outer unforced variables (λ_x^f) at each streamwise location.

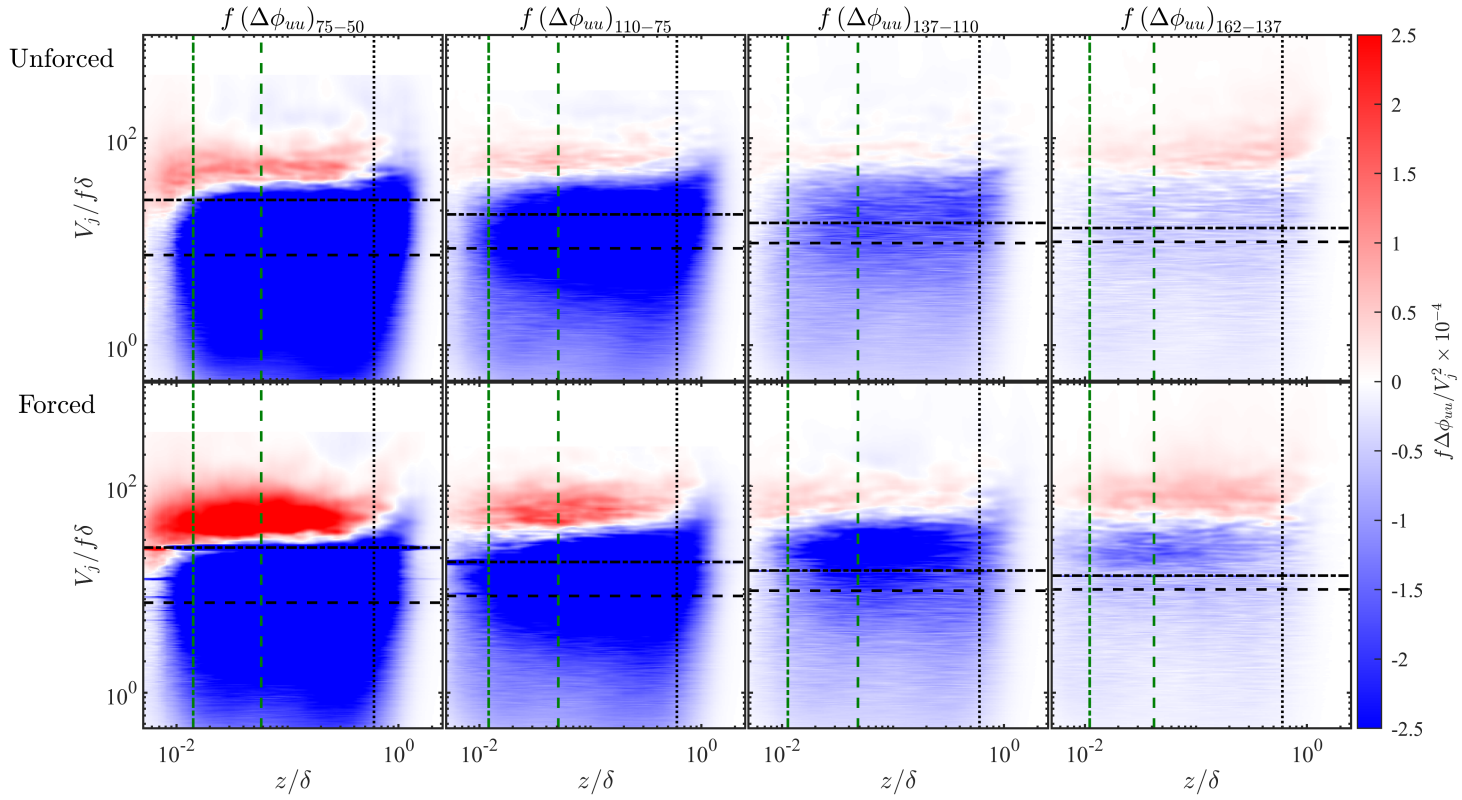

Figure 6.6. Difference of the pre-multiplied energy spectra between a streamwise location (n) and the immediate upstream location ($n-1$). Here, n represents n^{th} streamwise location where $n = 1 \implies x/b = 75$. The top figures represent unforced flow and the bottom figures represent forced flow for Case B conditions. The vertical lines show the wall-normal locations $z^+ \approx 15$ (—·—·), $z^+ \approx 60$ (- - - -) and $z \approx 0.6\delta^0$ (·····) respectively at the n^{th} location. The cut-off wavelength $\lambda_c = 2\delta^0$ (- - - -) and the forcing wavelength $\lambda_j/b \approx 295$ for Case B (-----) non-dimensionalized with respect to the outer length scale δ are also shown.

energy is seen in the large-scales that lie below z_m^0. The recipient wavelengths, referred to as λ_x^r for the remainder of this discussion, moves to larger and larger wavelengths with increasing downstream location. Here again, it is noted that λ_x^r refers to a range of wavelengths.

Restricting for the moment the discussion to the wall region, at the most upstream locations $x/b \leq 110$, λ_x^f is greater than the peak in λ_{xi}^n. However, the forcing wavelength is nominally equal to the larger wavelengths of the peak in λ_{xo}^n; see Table 5.1 for a numerical value associated with λ_x^f at each streamwise location. In this case the energy from λ_x^f and its harmonics are transferred to λ_x^r with λ_x^r spanning wavelengths greater than and and less than λ_x^f. Hence the energy at λ_x^f is being depleted to scales larger than itself in the manner of an inverse cascade as well as to scales smaller than itself in the manner of a forward cascade.

In the case of the higher harmonics of λ_x^f the energy transfer is in the manner of an inverse cascade as the higher harmonics of λ_x^f are smaller than λ_x^r. At further downstream locations $x/b \geq 137$, the energy transfer is almost exclusively to scales larger than λ_x^f in the manner of an inverse cascade.

In the outer region, there is no increase in the large-scale energy (except at λ_x^f and its harmonics) up to $x/b = 75$. When $x/b \geq 110$, there is a small increase in the energy of the scales larger than λ_x^f again indicative of an energy transfer in the manner of an inverse cascade. In the outer regions of the flow ($z \approx 0.6\delta^0$), the line plots of Figure 6.3 show that the effect of forcing at streamwise locations $x/b \geq 110$ is to increase the overall energy in the large-scales while increasing the peak of λ_{xo}^n.

Considering the small-scale energy $\lambda_x < 2\delta^0$, at all streamwise distances there is a decrease in small-scale energy in the forced flow with respect to the unforced flow at wall-normal distances $z \lessapprox 0.6\delta^0$, whereas at higher wall-normal locations there is an increase in energy (see Figure 6.5). Particularly in the near-wall region $z^+ \approx 15$ (see line plots of Figure 6.3) the reduction in energy of the small-scales are more significant than at $z^+ \approx 60$. This reduction in the near-wall small-scale energy is tied to the observed decrease in C_{f_j} when the flow is forced.

The difference in energy between a streamwise location and the preceding upstream location corresponding to Case B and the unforced flow is now considered. As discussed previously, the energy transfer upon forcing is directed with respect to the relative size between the forcing scales (λ_x^f) and the naturally energetic large-scales of the flow (λ_{xi}^n and λ_{xo}^n). The naturally energetic large-scales grow larger as the flow develops downstream. Taking the difference of the pre-multiplied energy spectra between a downstream streamwise location and the immediate upstream location provides insight into the transfer of energy between scales as the flow develops.

Figure 6.6 plots the difference of the pre-multiplied energy spectra $\Delta\phi_{uu}$ versus the streamwise wavelength non-dimensionalized using the respective outer length scale δ of the forced and unforced flows. In the case of the unforced flow, the energy in the large-scales is increasing naturally with an increase in downstream direction as the larger scales are getting larger because of the spreading of the PWJ. This increase primarily occurs in the wall region ($z \lessapprox 0.6\delta^0$) at $x/b \leq 137$. At streamwise locations $x/b \leq 137$, the energy of the large-scales larger than the naturally energetic large-

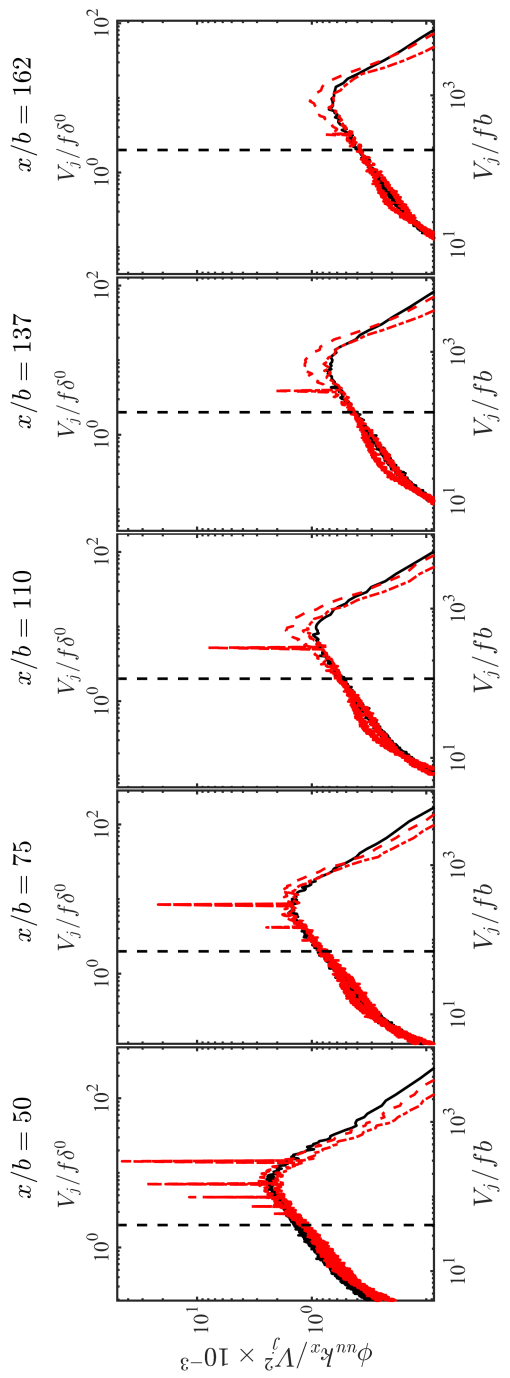

Figure 6.7. Comparison of PWJ pre-multiplied spectra $k_x\phi_{uu}/V_j^2$ verses V_jf/b for Case B at the near-wall locations $z^+ = 15$ (- - - -) and logarithmic location $z^+ = 60$ (- - - -) and the unforced flow at $z = 0.6\delta$ (——) respectively. The vertical line (- - - -) shows the cut-off wavelength $\lambda_c = 2\delta^0$.

scales appear to reduce as the flow develops. At x/b = 162, the energy of the large-scales increases in both the inner and outer region. The energy of the small-scales decreases at all wall-normal locations as the flow develops downstream.

It appears that the forcing augments this natural behavior of the flow. In the case of the forced flow, the energy of the large-scales increases as the flow develops. This increase in the energy of the large-scales occurs at all wall-normal locations. At each stream-wise location, the energy peak corresponding to the linear forcing response is also shown (**-----**). The decrease of energy at the forcing wavelength λ_x^f suggests a transfer of forcing energy. The recipient scales of the energy are scales larger than λ_x^f. This again indicates the transfer of energy in the manner of an inverse cascade. However, the recipient wavelengths of large-scales in the case of the forced flow are λ_{xo}^n, i.e. the naturally energetic large-scales concentrated in the outer region of the unforced flow.

The latter behavior is shown in Figure 6.7, which shows a comparison of the pre-multiplied energy spectra of the forced flow at $z^+ \approx 15$ and 60 with that of the unforced flow at $z \approx 0.6\delta^0$, i.e., the forcing response in the wall region is compared with the unforced flow in the outer region. It is observed that the energy peak corresponding to the forced PWJ in the wall region are that of the unforced PWJ in the outer region, i.e., the recipient scales λ_x^r correspond to wavelengths belonging to naturally energetic large-scales in the outer region λ_{xo}^n or $\lambda_x^r \cong \lambda_{xo}^n$. However, this increase primarily occurs in the wall-region.

This observation suggests that the non-linear forcing response has two aspects. First, the recipient wavelength corresponds to the wavelength of the energetic scales of the outer free-shear layer layer. Second, its signature in the wall region suggests that the forcing in addition causes a transport of the scales from the outer region into the wall-region.

6.2 Comparison of Case A, Case B, and Case C

A comparison of all forcing cases (Case A, B and C) is now discussed. Figure 6.8 shows the energy spectra at the previously mentioned three wall-normal locations for the unforced (——), Case A (——), Case B (——) and Case C (——) respectively. The energy spectra at $x/b = 50$ is also included for comparison. The corresponding contour plots of the pre-multiplied energy spectra are given in Appendix B.

The forced flow for Case A ($\lambda_j/b \approx 500$) is first discussed. Along with the linear response at the forcing frequency several higher order harmonics are seen at stream-wise locations $x/b \leq 110$ (see blue lines in Figure 6.8). The wall region ($z^+ \approx 15$ and 60) contains more higher order harmonics when compared to the outer region ($z \approx 0.6\delta^0$) at $x/b \leq 110$. With increasing downstream distance the non-linear, higher order harmonic response eventually dies out at all wall-normal locations, although it prevails to greater downstream locations in the wall region ($z^+ \approx 15$ and 60) than in the outer region ($z \approx 0.6\delta^0$). In the outer region ($z \approx 0.6\delta^0$) the higher harmonics have no energy past $x/b = 75$, though at $z^+ \approx 15$ and 60 the first harmonic has significant energy at $x/b \leq 75$, and this energy dies out at $x/b = 137$. It can also

be seen that the linear response mode at the fundamental forcing frequency (f_f = 7 Hz) persists in the wall layer through all streamwise locations considered, while in the outer region there is very little energy at f_f at streamwise distances $x/b \geq 137$.

At x/b = 50, the first harmonics is stronger in magnitude than the peak corresponding to the fundamental forcing frequency (f_f = 7 Hz). A possible explanation for this observation is that at this streamwise location, for Case A, the fundamental forcing wavelength is larger than the naturally energetic large-scales of the flow ($\lambda_x^f > \lambda_{xo}^n$). Hence, the fundamental forcing wavelength transfers energy in a manner of a forward cascade at x/b = 50.

At this location the corresponding wavelength of the first harmonic of f_f = 7 Hz corresponds to λ_{xo}^n. Hence, the first harmonic at x/b = 50 receives the energy from the fundamental forcing wavelength. At x/b = 75 and 110, the forcing energy appears to be transferred to scales both larger and smaller than the fundamental forcing frequency indicating energy transfer in a manner of an inverse as well as a forward cascade, respectively. At downstream locations ($x/b \geq 137$), the flow primarily transfers energy in a manner of an inverse cascade for Case A.

The forced flow for Case C ($\lambda_j/b \approx 220$) is now considered. The higher-order harmonics observed at $x/b \leq 75$ for Case C are fewer than Case A and B (see green lines in Figure 6.8). The higher harmonics lose their magnitude in the wall region ($z^+ \approx 15$ and 60) at $x/b \geq 110$. In the outer region ($z \approx 0.6\delta^0$), the higher harmonics contain very little energy that dies out at $x/b \geq 75$. The fundamental forcing response at f_f = 16 Hz exhibits a strong peak in the wall region at $x/b \leq 110$ and in the outer

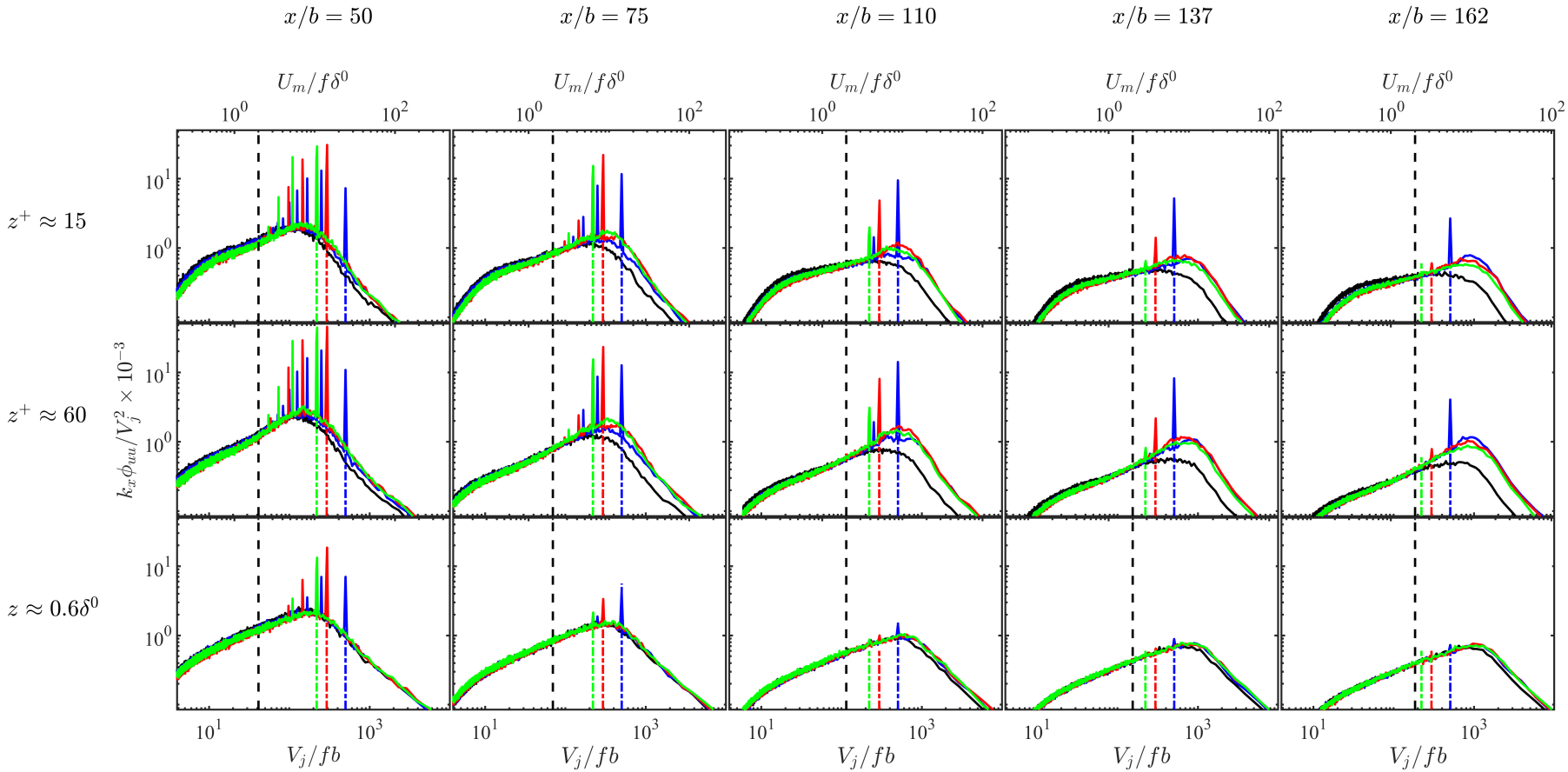

Figure 6.8. Comparison of PWJ pre-multiplied spectra $k_x\phi_{uu}/V_j^2$ (——) verses $V_j f/b$ for all forcing wavelengths at the wall-normal locations z^+ = 15 (top), z^+ = 60 (middle) and $z = 0.6\delta$ (bottom) respectively. The black color represents the unforced flow, blue color represents Case A ($\lambda_j/b \approx 500$), red color represents Case B ($\lambda_j/b \approx 295$) and green color represents Case C ($\lambda_j/b \approx 220$). The vertical lines show the cut-off wavelength $\lambda_c = 2\delta^0$ (- - - -) and the forcing wavelength λ_j/b for Case A (-·-·-), B (-·-·-) and C (-·-·-) respectively.

region at $x/b = 50$. In this forcing case, the flow appears to transfer energy in a manner of a forward as well as an inverse cascade at $x/b \leq 75$. Past $x/b = 110$, the flow almost exclusively transfers energy in a manner of an inverse cascade.

Therefore, all forcing cases transfer energy in a manner of a forward and an inverse cascade, depending on their relative scale with respect to the naturally energetic large-scales of the flow (λ_{xi}^n and λ_{xo}^n). Also, it appears that the persistence of the energy peak at the fundamental forcing wavelength as the flow develops is proportional to the size of the forcing scales. In other words, the energy peak corresponding to the fundamental forcing wavelengths (and its harmonics) retain its magnitude through longer streamwise distances for larger forcing wavelengths.

Consistent with the observations made for Case B, Case A and Case C also reduces the energy of the small-scales in the wall region ($z^+ \approx 15$ and 60). This reduction in small-scales is more prominent at $z^+ \approx 15$. In the interest of brevity, the contour plots showing the difference of the pre-multiplied energy spectra, at a fixed streamwise location, between forced and unforced flows for Case A and C are shown in Appendix B.

Figure 6.9 shows the difference of the pre-multiplied energy spectra $\Delta\phi_{uu}$ between $x/b = 75$ and 50 for Case A. This figure is used to highlight a feature of the transfer of energy between scales upon forcing. Is observed that the energy at the fundamental forcing (λ_x^f) wavelength reduces in the outer region ($z \geq 0.6\delta^0$), whereas it increases in the inner region. This mechanism suggests a transfer of energy from the outer region to the inner region. This behavior occurs only at the large-scales of the flow.

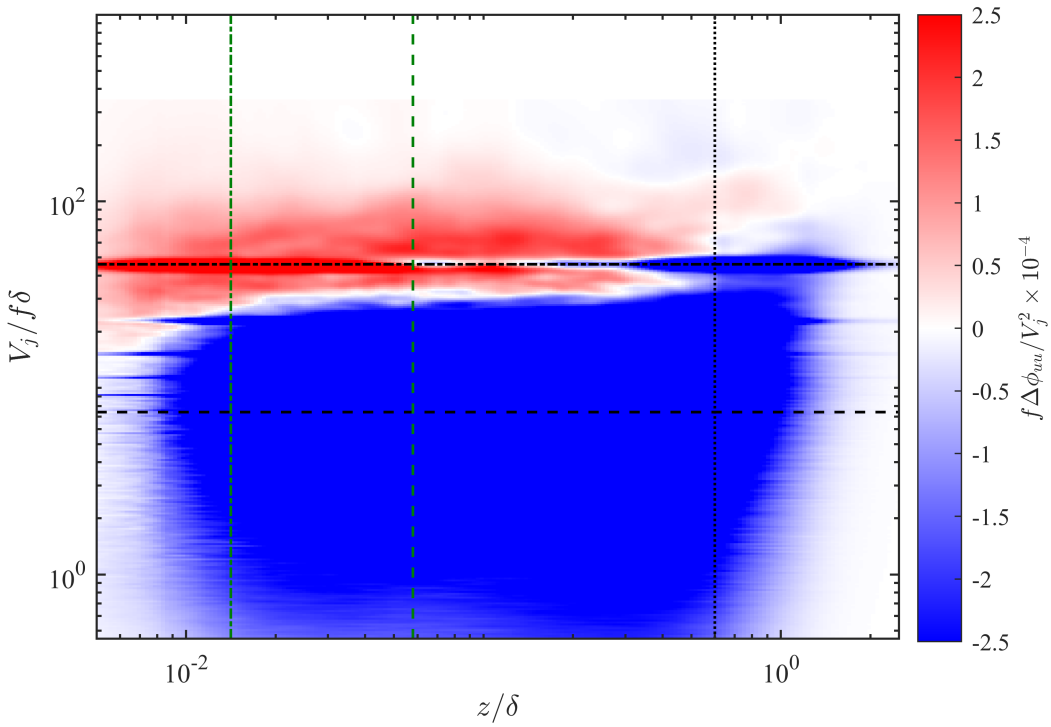

Figure 6.9. Difference of pre-multiplied energy spectra between x/b = 75 and x/b = 50. The vertical lines show the wall-normal locations $z^+ \approx 15$ (–·–·–), $z^+ \approx 60$ (- - - -) and $z \approx 0.6\delta^0$ (·····) respectively at the x/b = 75. The cut-off wavelength $\lambda_c = 2\delta^0$ (- - - -) and the forcing wavelength $\lambda_j/b \approx 500$ for Case A (-----) non-dimensionalized with respect to the outer length scale δ are also shown.

As the flow develops, these energy recipient large-scales λ_x^f grow larger such that the extent of the energy transfer then spans all wall-normal locations. The corresponding contour plots of the difference are shown in Appendix B.

6.3 Summary

It was observed that the PWJ contains naturally energetic large-scales primarily concentrated in the logarithmic region ($0.01\delta^0 \lessapprox z \lessapprox 0.12\delta^0$, λ_{xi}^n) and outer region (around $z \approx 0.6\delta^0$, λ_{xo}^n). As the flow develops, these structures grow larger, which

changes their relative scale with respect to the forcing scale λ_x^f. This relative scale difference leads to some interesting observations, as summarized below.

- Along with the linear forcing response at the fundamental forcing wavelength λ_x^f, several higher harmonics were observed in the flow. More higher harmonics were observed in the wall region ($z^+ \approx 15$ and 60) when compared to the outer region ($z \approx 0.6\delta^0$). With increasing streamwise distance, the energy peak corresponding to the fundamental forcing wavelength and its harmonics reduces in magnitude and eventually disappears at downstream locations. These energy peaks retain their coherence at longer streamwise distances for larger forcing wavelengths.

- Figure 6.10 illustrates key observations regarding energy transfer in the PWJ. At the upstream locations where the forcing scale λ_x^f is larger than λ_{xi}^n and λ_{xo}^n, the forcing energy is primarily transfered to scales smaller than λ_x^f. This mechanism indicates an energy transfer in the manner of a forward cascade. At downstream locations where the forcing scales are smaller than λ_{xi}^n and λ_{xo}^n, the forcing transfers energy to the scales larger than λ_x^f indicating an energy transfer in the manner of an inverse cascade. The scales that are recipients of the forcing energy λ_x^r were observed to primarily reside in the logarithmic region of the flow.

- The forcing reduces the energy of the small-scales in the wall-region. In the outer region at the edge of PWJ, the forcing increases energy of all scales.

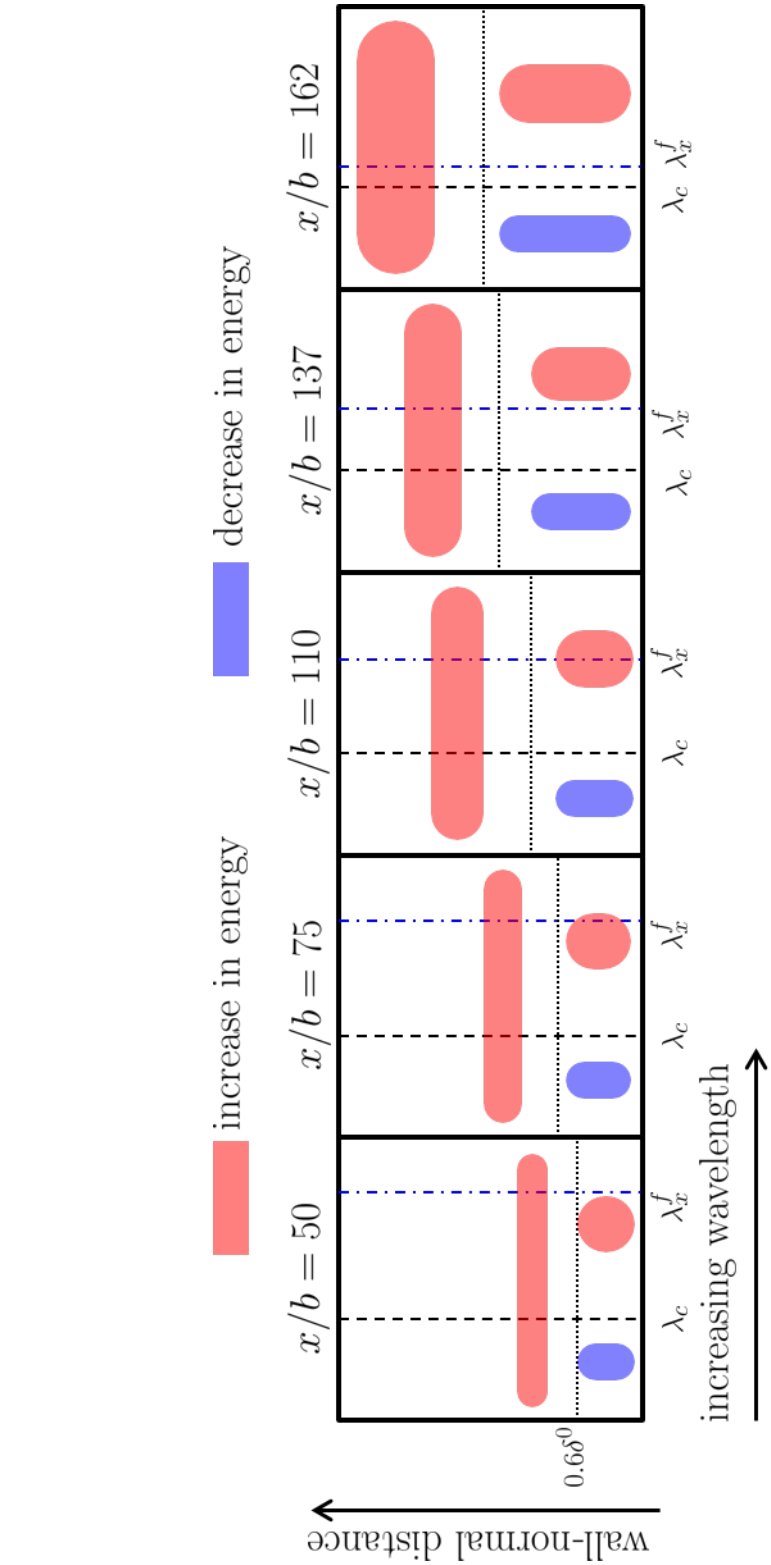

Figure 6.10. A schematic explaining key observation regarding the transfer of energy in the flow. Here, $\lambda_c = 2\delta^0$ and $\lambda_x^f = U_m/f_f\delta$. The colors illustrate the wall-normal location where the change in energy is observed and the corresponding scales experiencing it.

- As the flow develops downstream, the difference of the pre-multiplied energy spectra between two streamwise locations reveals that, the PWJ increases the energy of the large-scales of the flow primarily in the wall region. The forcing appears to enhance this natural behavior of the PWJ.

- It is observed that the forcing increases the energy of the scales that are of the size of naturally energetic large scales in the outer region of the unforced PWJ, i.e. $\lambda_x^r \cong \lambda_{xo}^n$ (see Figure 6.7). However, λ_x^r primarily populates the logarithmic region of the PWJ. This behavior suggests a transport of the energetic large-scales of the outer free-shear layer into the inner region.

These observations show the superpositioning of the outer large-scale energy in the wall region. This superpositioning then appears to enhance the energy transfer between the outer region and inner region as the flow develops. As a result, the energy of the small-scales in the wall region reduces and causes reduction in friction velocity U_τ. This observation points towards strong inner-outer interactions within the PWJ which are discussed in the following chapter.

7. Scale Interactions

The characterization of the PWJ in terms of the mean turbulence statistics and the energy of the flow reveled that forcing targets the large-scales of the flow. The energy of the large-scales of the flow increases upon forcing. Based on the relative size between the forcing wavelength λ_x^f and naturally energetic large-scales of the flow (λ_{xi}^n and λ_{xo}^n), the PWJ exhibits energy transfer in the manner of a forward or an inverse cascade. This increase in energy primarily occurs in the wall region.

It is also observed that the forcing reduces the energy of the small-scales in the near-wall region whereas increases it at the edge of the shear-layer (see previously in Figure 6.10). Recalling that the forcing wavelengths correspond to the large scales of the flow, this simultaneous increase in the energy of the large-scales and the decrease in the energy of the small scales points toward a coupling between the two. Moreover, this coupled energy transfer results in the reduction of the friction velocity U_τ at the wall. This effect establishes a strong interaction between the energetic large-scale structures in the flow and the near-wall small-scale structures.

To understand this interaction, amplitude and frequency modulation of the near-wall small-scale structure is considered. Figure 7.1 shows the streamwise velocity U at a near-wall location $z^+ \approx 6$ decomposed into the large-scale components U_L and small-scale component U_s. Also shown is the large-scale component of the envelop of the small-scale component $E_L(U_s)$. Here, $U = U_L + U_s$. On one hand, it is observed that positive fluctuations of the large-scales increase the frequency and amplitude of

the corresponding small-scales. On the other hand, the negative fluctuations of the large-scales decrease the amplitude and frequency of the corresponding small-scales. This attenuation of the frequency and amplitude appears to be stronger in the case of the forced flow when compared with the unforced flow.

The amplitude modulation of the near-wall small-scale structures is quantified using the amplitude modulation coefficient R_{AM}. The amplitude modulation coefficient R_{AM} is calculated using Equation 2.1 (modified below to use total velocity decomposition instead of streamwise velocity) given by Mathis et al. (2009), i.e.,

$$R_{AM} = \frac{\overline{U_L E_L(U_s)}}{\sqrt{\overline{U_L^2}}\sqrt{\overline{E_L(U_s)^2}}}. \tag{7.1}$$

Where, E_L is calculated using the Hilbert transform.

The cut-off wavelength to discriminate the large-scales from the small-scales is $\lambda_c = 2\delta^0$. The value of R_{AM} varies between -1 and 1. When $R_{AM} \rightarrow 1$ corresponds to high amplitude modulation in the flow. When $R_{AM} = 0$, the flow exhibits no modulation. Whereas, $R_{AM} \rightarrow -1$ suggests that the large-scales and the small-scales are anti-correlated. Figure 7.2 shows the amplitude modulation coefficient R_{AM} using Equation 7.1 at all streamwise locations for all forcing cases.

It is observed that the unforced PWJ exhibits amplitude modulation in the near-wall region as well as the outer region at all streamwise locations considered. This modulation increases in the near-wall region as the flow develops downstream. At $x/b = 50$, R_{AM} is approximately 0.28 at $z^+ \approx 15$ for the unforced PWJ. As the flow

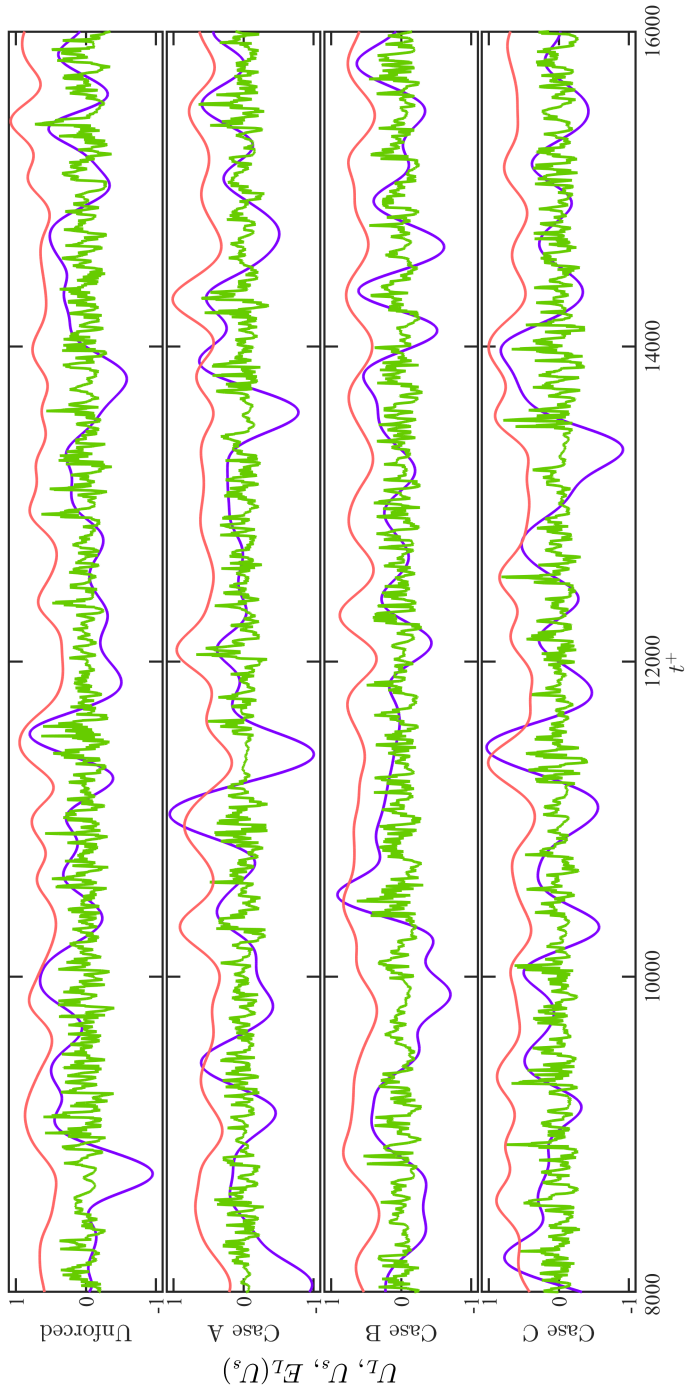

Figure 7.1. Visualization of the amplitude and frequency modulation at a near-wall location ($z^+ \approx 6$) when $x/b = 137$ for unforced flow, Case A, Case B and Case C respectively. The lines represent the larges-scale velocity component U_L (——), the small-scale velocity component U_s (——) and the large-scale component of the envelop of the small-scale component ($E_L(U_s)$) (——). The amplitude of the small-scale signal is attenuated using a constant factor for the purpose of visualization.

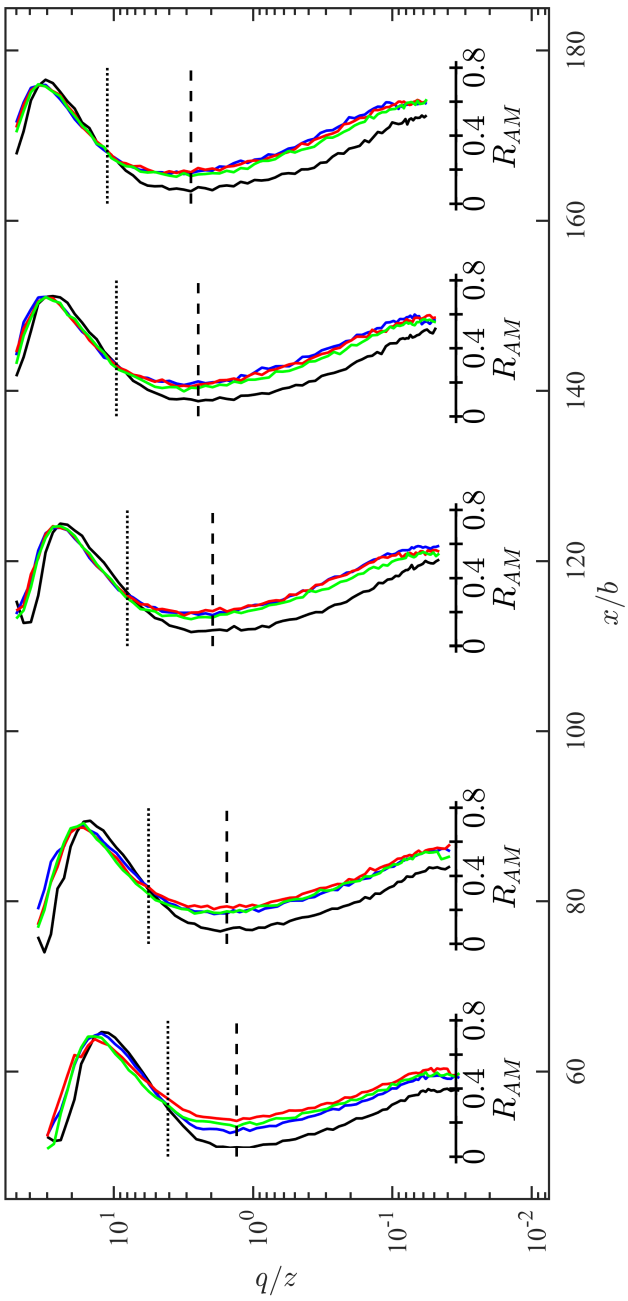

Figure 7.2. A comparison of the amplitude modulation coefficient R_{AM} as given in Equation 7.1 for unforced and forced flows all streamwise locations considered. Here, the cut-off wavelength $\lambda_c = 2\delta^0$. While comparing all forcing conditions, the unforced flow is visualized using black color, the $\lambda_j/b \approx 500$ forcing is visualized using blue color, the $\lambda_j/b \approx 295$ forcing is visualized using red color and the $\lambda_j/b \approx 220$ forcing is visualized using green color. The wall-normal location $z \approx 0.6\delta^0$ (.....) and $z \approx z_m^0$ (- - - -) are also shown.

develops, this value increases and reaches ≈ 0.32 at $x/b = 162$. This result indicates a naturally increasing modulation effect as the flow develops.

Upon forcing, the modulation increases in the region $z \lessapprox 0.6\delta^0$ for all forcing wavelengths at all streamwise locations that were considered. However, it remains relatively unaffected in the outer region ($z \gtrsim 0.6\delta^0$). In Figure 7.2, the line (·····) represents the wall-normal location $z \approx 0.6\delta^0$ at all streamwise locations. At each streamwise location, at $z^+ \approx 15$, the increase in R_{AM} was observed to be $\approx 45.9\%$, $\approx 47.7\%$ and $\approx 35.5\%$ for Case A, B and C, respectively.

It is noted that the increase in the turbulence intensity and the corresponding increase in the turbulence kinetic energy targets the large-scales of the flow primarily in the wall region. This observation is tied to the corresponding increase in R_{AM}. The amplitude modulation coefficient R_{AM} is observed to increase consistently in the wall region upon forcing. This is an indication of strong influence of the energetic large-scales of the flow on the near-wall small-scales. Thus, it is observed that the increase in large-scale energy directly affects the coupling between the scales with a corresponding decrease the friction velocity U_τ at the wall.

8. Conclusions and Recommendations

A novel approach for friction drag reduction was considered. The approach proposed targetting the large-scales of the flow to control the near-wall small scales. To study the non-linear interactions between the large-scales and the small-scales, a model flow field–the plane wall jet (PWJ)–was acoustically forced over a range of forcing wavelengths corresponding to the large-scales of the flow. The resulting scale interactions were characterized in terms of the friction velocity U_τ and the energy transfer between scales. Mean turbulence and spectral analyzes of the forced and the unforced PWJ were carried out to characterize the energy transfer mechanisms corresponding to the scale interactions. The measurements were conducted using the hot-wire anemometry.

The forcing response of the PWJ was characterized through two sets of measurements. First, the near-wall response of the PWJ was analyzed over twenty forcing wavelengths at streamwise locations spanning $x/b = 110 - 162$. Based on this study, a detailed study of the PWJ was carried out at three forcing wavelengths. The key observations and conclusions are summarized below.

8.1 Summary of Observations

1. A reduction of the friction velocity U_τ was observed for all forcing wavelengths considered. This reduction was observed to be maximum for the forcing scale

$\lambda_j/b \approx 295$ corresponding to forcing frequency at f_f = 12 Hz at all streamwise locations considered.

2. The reduction in friction velocity ΔU_τ was scaled using inner, outer and global variables of the flow. The scaling behavior suggested that the PWJ is reacting to the forcing up to x/b = 110 after which the reduction in U_τ, i.e., ΔU_τ exhibit a consistent scaling behavior.

3. The scaling showed a dependence on the inner variables that are of the order $\mathcal{O}(\nu/U_\tau)$. The dependence of ΔU_τ on outer variables was also observed. Together these observations suggested a coupling between the inner-scaled structures and the outer-scaled structures. The scaling also suggested a strong dependence on the global variables (PWJ exit velocity V_j and height b). This lead to the conclusion that an inner-outer interaction along with a dependence on the PWJ exit Reynolds number Re_j governs the flow physics of the forced PWJ.

4. To better characterize these foregoing interactions a second set of the measurements was carried out. In this set, three forcing wavelengths $\lambda_j/b \approx 500$ (Case A, f_f = 7 Hz), 295 (Case B, f_f = 12 Hz) and 220 (Case C, f_f = 16 Hz) were chosen for a detailed study of the forced PWJ spanning streamwise distances $x/b = 50 - 162$. It was observed that, along with the reduction in the inner velocity scale U_τ, the forcing also reduced the outer velocity scale U_m. The

maximum reduction in U_m corresponded to the forcing wavelength that caused the maximum reduction in U_τ, i.e., $\lambda_j/b \approx 295$ (Case B).

5. The forcing was also seen to increase the outer length scale δ of the PWJ such that it increased the rate of spreading $(d\delta/dx)$ of the PWJ. The reduction in U_τ and increase in the outer length-scale (δ) together increased the Reynolds number Re_τ upon forcing.

6. The reduction in U_τ and U_m coupled with the increased spread rate of the PWJ resulted in the reduced skin friction, along with a transfer of momentum from the inner region to the outer region of the flow. The maximum reduction of the momentum in the wall region was observed for Case B, which corresponded to the case with the maximum reduction in U_τ.

7. Following past studies (Hussain and Reynolds, 1970; Duvvuri and McKeon, 2015; McKeon et al., 2018), upon triple decomposition of the velocity signal it was observed that the forcing introduced distinct periodic structures into the flow. In the wall region, these structures were wall-attached and forward leaning similar to those seen in zero pressure gradient boundary layers. Away from the wall these structures were observed to exhibit both forward and backward inclinations based on the streamwise location. As the flow developed, these structures exhibited a phase difference, which suggested that they convect at different convection velocities. These type of forward leaning structure at the wall and backward leaning structures in the outer region have been reported in

the PWJ flow in literature (Banyassady and Piomelli, 2014; Gnanamanickam et al., 2019).

8. The forcing was also observed to increase the turbulence intensity of the flow. This increase was observed to occur primarily in the wall region. The decomposition of the total turbulence intensity into a large-scale component ($\lambda_x \geq 2\delta^0$) and a small-scale component ($\lambda_x < 2\delta^0$) revealed that this increase in turbulence intensity was limited to the large-scales of the flow.

9. To understand the energy distribution within scales, spectral analyses was conducted. It was observed that the relative scale of the forcing wavelength λ_x^f with respect to the naturally energetic large-scales of the flow λ_{xi}^n and λ_{xo}^n plays a deciding role in the transfer of forcing energy. Irrespective of the size of the forcing scales, the primary recipients of the forcing energy were the naturally energetic large-scales of the outer shear layer. At the upstream locations, where the forcing scales λ_x^f were larger than λ_{xi}^n and λ_{xo}^n, the forcing energy primarily transferred to scales smaller than λ_x^f in the manner of a forward cascade. As the flow developed, the naturally energetic large-scales were seen to grow larger. Hence, at downstream locations where the forcing scales were smaller than λ_{xi}^n and λ_{xo}^n, the forcing was observed to transfer energy to the scales larger than λ_x^f in the manner of an inverse cascade. The large-scales that were the recipients of the forcing energy λ_x^r ($\approx \lambda_{xo}^n$) were observed to primarily populate the logarithmic region of the flow. This effect suggested transport of the energetic

large-scales from the outer region to the wall region. This observation is tied to the transport of momentum from the wall region to the outer region.

10. The forcing was also observed to reduce the energy of the small-scales in the wall-region. Away from the wall, at the edge of the PWJ, the forcing was seen to increase the energy of all scales. It was observed that within the unforced PWJ, the energy of the large-scales of the flow increases as a consequence of the spreading of the PWJ. The forcing was seen to enhance this natural behavior of the PWJ.

11. The simultaneous energy transfer of the large-scale and the small-scales pointed towards a coupling between the large-scales and the small-scales of the inner and outer region of the PWJ. This coupling between scales was then quantified using the amplitude modulation coefficient R_{AM} given by Mathis et al. (2009). The forcing was observed to increase R_{AM} in the wall region of the PWJ indicating increased interaction between the outer large-scales and small-scales of the flow.

8.2 Conclusions

It is concluded that the forcing successfully targeted the large-scales of the flow. It redistributed the energy of the flow within scales such that it altered the scale interactions within the flow. The forcing changed the transport of the energetic large-scales between the inner and outer region which resulted in the transport of momentum from the inner region to the outer region. These interactions also result in the reduction of the skin friction.

The current results prove that the near-wall small-scale structures contributing towards the friction drag can be controlled through the large-scale structures away from the wall. This means that a systematic control of the large-scale structures within the flow can result in skin friction drag reduction. Moreover, considering the economical and technological benefit of targeting large-scale structures, the current work forms a basis for the development of an affordable and aerodynamically efficient flow control system.

8.3 Future Work

The current measurements were made with a single-component hot-wire measurements. While providing excellent temporal resolution, the use of single hot-wire anemometry limits the analyses of the energy transfer to that derived from the effective velocity. The energy transfer corresponding to the spanwise and wall-normal velocity components cannot be determined or distinguished using the current measurements. Hence, the current work only assesses the energy transfer in the streamwise–wall-normal plane biased towards the streamwise velocity.

In a recent DNS study of the PWJ, Naqavi et al. (2018) observed that through inner-outer interactions, the energy in the outer region transfers to the spanwise direction in the inner region. Therefore, based on the present work, the energy transfer in the spanwise–wall-normal plane is currently unknown.

Two-component hot-wire and PIV measurements would provide insightful information regarding this energy transfer. Furthermore, the current measurements are

not spatially correlated. The single point analyses limits the current investigations in identifying the presence of different flow structures in the PWJ. Two-point correlation from simultaneous measurements of the flow field would give information regarding the characteristics of the energetic large-scale structures of the flow and the changes to them upon forcing.

REFERENCES

Abe, H., Kawamura, H., and Choi, H. (2004). Very large-scale structures and their effects on the wall shear-stress fluctuations in a turbulent channel flow up to $\mathrm{Re}_\tau = 640$. *Journal of Fluids Engineering*, 126(5):835–843.

Abrahamsson, H., Johansson, B., and Löfdahl, L. (1994). A turbulent plane two-dimensional wall-jet in a quiescent surroundings. *European Journal of Mechanics/B-Fluids*, 13(6).

Adrian, R. J. (2007). Hairpin vortex organization in wall turbulence. *Physics of Fluids*, 19(4):041301.

Adrian, R. J., Meinhart, C. D., and Tomkins, C. D. (2000). Vortex organization in the outer region of the turbulent boundary layer. *Journal of Fluid Mechanics*, 422:1–54.

Ahlman, D., Velter, G., Brethouwer, G., and Johansson, A. V. (2009). Direct numerical simulation of nonisothermal turbulent wall jets. *Physics of Fluids*, 21(3):035101.

Baars, W., Hutchins, N., and Marusic, I. (2017a). Reynolds number trend of hierarchies and scale interactions in turbulent boundary layers. *Philosophical Transactions of the Royal Society A: Mathematical, Physical and Engineering Sciences*, 375(2089):20160077.

Baars, W. J., Hutchins, N., and Marusic, I. (2016). Spectral stochastic estimation of high-reynolds-number wall-bounded turbulence for a refined inner-outer interaction model. *Physical Review Fluids*, 1:054406.

Baars, W. J., Hutchins, N., and Marusic, I. (2017b). Self-similarity of wall-attached turbulence in boundary layers. *Journal of Fluid Mechanics*, 823:R2.

Balakumar, B. and Adrian, R. (2007). Large- and very-large-scale motions in channel and boundary-layer flows. *Philosophical Transactions of the Royal Society A: Mathematical, Physical and Engineering Sciences*, 365(1852):665–681.

Bandyopadhyay, P. R. and Hussain, A. K. M. F. (1984). The coupling between scales in shear flows. *Physics of Fluids*, 27(9):2221–2228.

Banyassady, R. and Piomelli, U. (2014). Turbulent plane wall jets over smooth and rough surfaces. *Journal of Turbulence*, 15(3):186–207.

Banyassady, R. and Piomelli, U. (2015). Interaction of inner and outer layers in plane and radial wall jets. *Journal of Turbulence*, 16(5):460–483.

Batchelor, G. K., Townsend, A. A., and Harold, J. (1949). The nature of turbulent motion at large wave-numbers. *Proceedings of the Royal Society of London. Series A. Mathematical and Physical Sciences*, 199(1057):238–255.

Bergstrom, D. J., Tachie, M. F., and Balachandar, R. (2001). Application of power laws to low reynolds number boundary layers on smooth and rough surfaces. *Physics of Fluids*, 13(11):3277–3284.

Brown, G. and Thomas, A. W. (1977). Large structure in a turbulent boundary layer. *Physics of Fluids*, 20(10):S243–S252.

BTS (2019). Bureau of transportation statistics airline fuel cost and consumption. https://www.transtats.bts.gov/fuel.asp.

Chauhan, K., Monkewitz, P., and Nagib, H, M. (2009). Criteria for assessing experiments in zero pressure gradient boundary layers. *Fluid Dynamics Research*, 41(2):021404.

Chung, D. and McKeon, B. J. (2010). Large-eddy simulation of large-scale structures in long channel flow. *Journal of Fluid Mechanics*, 661:341–364.

Davidson, P. (2015). *Turbulence: an introduction for scientists and engineers*. Oxford University Press.

De Graaff, D. B. and Eaton, J. K. (2000). Reynolds-number scaling of the flat-plate turbulent boundary layer. *Journal of Fluid Mechanics*, 422:319–346.

de Silva, C. M., Philip, J., Hutchins, N., and Marusic, I. (2017). Interfaces of uniform momentum zones in turbulent boundary layers. *Journal of Fluid Mechanics*, 820:451–478.

Dejoan, A. and Leschziner, M. A. (2005). Large eddy simulation of a plane turbulent wall jet. *Physics of Fluids*, 17(2):025102.

Dejoan, A., Wang, C., and Leschziner, M. A. (2006). Assessment of turbulence models for predicting the interaction region in a wall jet by reference to les solution and budgets. *Flow, Turbulence and Combustion*, 77(1-4):229–255.

Dogan, E., Hanson, R. E., and Ganapathisubramani, B. (2016). Interactions of large-scale free-stream turbulence with turbulent boundary layers. *Journal of Fluid Mechanics*, 802:79–107.

Dunham, J. (1968). A theory of circulation control by slot-blowing, applied to a circular cylinder. *Journal of Fluid Mechanics*, 33(3):495–514.

Duvvuri, S. and McKeon, B. J. (2014). Phase relationships in presence of a synthetic large-scale in a turbulent boundary layer. In *44th AIAA Fluid Dynamics Conference*, page 2883.

Duvvuri, S. and McKeon, B. J. (2015). Triadic scale interactions in a turbulent boundary layer. *Journal of Fluid Mechanics*, 767.

Eriksson, J. G., Karlsson, R. I., and Persson, J. (1998). An experimental study of a two-dimensional plane turbulent wall jet. *Experiments in Fluids*, 25(1):50–60.

Falco, R. E. (1977). Coherent motions in the outer region of turbulent boundary layers. *Physics of Fluids*, 20(10):S124–S132.

Filippone, A. (2000). Data and performances of selected aircraft and rotorcraft. *Progress in Aerospace Sciences*, 36(8):629–654.

Francis, H. C. (1954). Turbulent boundary layers in adverse pressure gradients. *Journal of the Aeronautical Sciences*, 21(2):91–108.

Gad-el Hak, M. and Bandyopadhyay, P. R. (1994). Reynolds number effects in wall-bounded turbulent flows. *Applied Mechanics Reviews*, 47(8):307–365.

Ganapathisubramani, B., Hutchins, N., Hambleton, W. T., Longmire, E. K., and Marusic, I. (2005). Investigation of large-scale coherence in a turbulent boundary layer using two-point correlations. *Journal of Fluid Mechanics*, 524:57–80.

Ganapathisubramani, B., Hutchins, N., Monty, J. P., Chung, D., and Marusic, I. (2012). Amplitude and frequency modulation in wall turbulence. *Journal of Fluid Mechanics*, 712:61–91.

Ganapathisubramani, B., Longmire, E. K., and Marusic, I. (2003). Characteristics of vortex packets in turbulent boundary layers. *Journal of Fluid Mechanics*, 478:35–46.

George, W. K., Abrahamsson, H., Eriksson, J., Karlsson, R. I., Löfdahl, L., and Wosnik, M. (2000). A similarity theory for the turbulent plane wall jet without external stream. *Journal of Fluid Mechanics*, 425:367–411.

Glauert, M. B. (1956). The wall jet. *Journal of Fluid Mechanics*, 1(6):625–643.

Gnanamanickam, E. P., Bhatt, S. B., Artham, S. K., and Zhang, Z. (2017). Turbulence control by targeting the large-scale motions within boundary layers.

Gnanamanickam, E. P., Bhatt, S. B., Artham, S. K., and Zhang, Z. (2019). Large-scale motions in a plane wall jet. Under review.

Guala, M., Hommema, S. E., and Adrian, R. J. (2006). Large-scale and very-large-scale motions in turbulent pipe flow. *Journal of Fluid Mechanics*, 554:521–542.

Guala, M., Metzger, M., and McKeon, B. (2011). Interactions within the turbulent boundary layer at high reynolds number. *Journal of Fluid Mechanics*, 666:573–604.

Guerra, D. R. S., Su, J., and Freire, A. P. S. (2005). The near wall behavior of an impinging jet. *International Journal of Heat and Mass Transfer*, 48(14):2829 – 2840.

Guitton, D. E. and Newman, B. G. (1977). Self-preserving turbulent wall jets over convex surfaces. *Journal of Fluid Mechanics*, 81(1):155–185.

Hamilton, J. M., Kim, J., and Waleffe, F. (1995). Regeneration mechanisms of near-wall turbulence structures. *Journal of Fluid Mechanics*, 287:317–348.

Harun, Z., Monty, J. P., Mathis, R., and Marusic, I. (2013). Pressure gradient effects on the large-scale structure of turbulent boundary layers. *Journal of Fluid Mechanics*, 715:477–498.

Head, M. R. and Bandyopadhyay, P. (1981). New aspects of turbulent boundary-layer structure. *Journal of Fluid Mechanics*, 107:297–338.

Hoyas, S. and Jiménez, J. (2006). Scaling of the velocity fluctuations in turbulent channels up to $re_\tau = 2003$. *Physics of Fluids*, 18(1):011702.

Hussain, A. K. M. F. and Reynolds, W. C. (1970). The mechanics of an organized wave in turbulent shear flow. *Journal of Fluid Mechanics*, 41(2):241–258.

Hutchins, N., Chauhan, K., Marusic, I., Monty, J., and Klewicki, J. (2012). Towards reconciling the large-scale structure of turbulent boundary layers in the atmosphere and laboratory. *Boundary-Layer Meteorology*, 145(2):273–306.

Hutchins, N. and Choi, K.-S. (2002). Accurate measurements of local skin friction coefficient using hot-wire anemometry. *Progress in Aerospace Sciences*, 38(4-5):421–446.

Hutchins, N. and Marusic, I. (2007a). Evidence of very long meandering features in the logarithmic region of turbulent boundary layers. *Journal of Fluid Mechanics*, 579:1–28.

Hutchins, N. and Marusic, I. (2007b). Large-scale influences in near-wall turbulence. *Philosophical Transactions of the Royal Society A: Mathematical, Physical and Engineering Sciences*, 365(1852):647–664.

Hutchins, N., Monty, J. P., Ganapathisubramani, B., Ng, H. C. H., and Marusic, I. (2011). Three-dimensional conditional structure of a high-reynolds-number turbulent boundary layer. *Journal of Fluid Mechanics*, 673:255–285.

Hutchins, N., Nickels, T. B., Marusic, I., and Chong, M. (2009). Hot-wire spatial resolution issues in wall-bounded turbulence. *Journal of Fluid Mechanics*, 635:103–136.

Irwin, H. P. A. H. (1973). Measurements in a self-preserving plane wall jet in a positive pressure gradient. *Journal of Fluid Mechanics*, 61(1):33–63.

Jacobi, I. and McKeon, B. (2013). Phase relationships between large and small scales in the turbulent boundary layer. *Experiments in Fluids*, 54(3):1481.

Jeong, J., Hussain, F., Schoppa, W., and Kim, J. (1997). Coherent structures near the wall in a turbulent channel flow. *Journal of Fluid Mechanics*, 332:185–214.

Jiménez, J. (1994). On the structure and control of near wall turbulence. *Physics of Fluids*, 6(2):944–953.

Jiménez, J. (2018). Coherent structures in wall-bounded turbulence. *Journal of Fluid Mechanics*, 842:P1.

Jiménez, J. and Moin, P. (1991). The minimal flow unit in near-wall turbulence. *Journal of Fluid Mechanics*, 225:213–240.

Jiménez, J. and Pinelli, A. (1999). The autonomous cycle of near-wall turbulence. *Journal of Fluid Mechanics*, 389:335–359.

Karlsson, R. I., Eriksson, J., and Persson, J. (1992). LDV measurements in a plane wall jet in a large enclosure. Technical report, Royal Inst of Tech Stockholm (Sweden).

Kasagi, N., Suzuki, Y., and Fukagata, K. (2009). Microelectromechanical systems–based feedback control of turbulence for skin friction reduction. *Annual Review of Fluid Mechanics*, 41:231–251.

Katz, Y., Horev, E., and Wygnanski, I. (1992). The forced turbulent wall jet. *Journal of Fluid Mechanics*, 242:577–609.

Kim, K. C. and Adrian, R. J. (1999). Very large-scale motion in the outer layer. *Physics of Fluids*, 11(2):417–422.

Klewicki, J. C. (2007). *Springer handbook of experimental fluid mechanics, section 12.2*, volume 1. Springer Science & Business Media. Edited by Tropea, Cameron and Yarin, Alexander L.

Klewicki, J. C. (2010). Reynolds number dependence, scaling, and dynamics of turbulent boundary layers. *Journal of Fluids Engineering*, 132:094001–094001–48.

Kline, S. J., Reynolds, W. C., Schraub, F. A., and Runstadler, P. W. (1967). The structure of turbulent boundary layers. *Journal of Fluid Mechanics*, 30(4):741–773.

Kolmogorov, A. N. (1962). A refinement of previous hypotheses concerning the local structure of turbulence in a viscous incompressible fluid at high reynolds number. *Journal of Fluid Mechanics*, 13(1):82–85.

Kulandaivelu, V. (2011). *Evolution and structure of zero pressure gradient turbulent boundary layer*. PhD thesis, Department of Mechanical Engineering, University of Melbourne, Australia.

Launder, B. E. and Rodi, W. (1981). The turbulent wall jet. *Progress in Aerospace Sciences*, 19:81–128.

Launder, B. E. and Rodi, W. (1983). The turbulent wall jet measurements and modeling. *Annual Review of Fluid Mechanics*, 15(1):429–459.

Lee, M. and Moser, R. D. (2015). Direct numerical simulation of turbulent channel flow up to $\mathrm{Re}_\tau \approx 5200$. *Journal of Fluid Mechanics*, 774:395–415.

Lee, M. and Moser, R. D. (2019). Spectral analysis of the budget equation in turbulent channel flows at high reynolds number. *Journal of Fluid Mechanics*, 860:886–938.

Lozano-Durán, A., Flores, O., and Jiménez, J. (2012). The three-dimensional structure of momentum transfer in turbulent channels. *Journal of Fluid Mechanics*, 694:100–130.

Lu, S. S. and Willmarth, W. W. (1973). Measurements of the structure of the reynolds stress in a turbulent boundary layer. *Journal of Fluid Mechanics*, 60(3):481–511.

Marusic, I., Baars, W. J., and Hutchins, N. (2017). Scaling of the streamwise turbulence intensity in the context of inner-outer interactions in wall turbulence. *Physical Review Fluids*, 2(10):100502.

Marusic, I., Hutchins, N., and Mathis, R. (2010a). High reynolds number effects in wall turbulence. In *TSFP Digital Library Online*. Begel House Inc.

Marusic, I. and Kunkel, G. J. (2003). Streamwise turbulence intensity formulation for flat-plate boundary layers. *Physics of Fluids*, 15(8):2461–2464.

Marusic, I. and Kunkel, G. J. (2004). Turbulence intensity similarity laws for turbulent boundary layers. In *IUTAM Symposium on Reynolds Number Scaling in Turbulent Flow*, pages 17–22. Springer.

Marusic, I., McKeon, B. J., Monkewitz, P. A., Nagib, H. M., Smits, A. J., and Sreenivasan, K. R. (2010). Wall-bounded turbulent flows at high reynolds numbers: recent advances and key issues. *Physics of Fluids*, 22(6):065103.

Mathis, R., Hutchins, N., and Marusic, I. (2009). Large-scale amplitude modulation of the small-scale structures in turbulent boundary layers. *Journal of Fluid Mechanics*, 628:311–337.

Mathis, R., Hutchins, N., and Marusic, I. (2011). A predictive inner–outer model for streamwise turbulence statistics in wall-bounded flows. *Journal of Fluid Mechanics*, 681:537–566.

Mathis, R., Marusic, I., Chernyshenko, S. I., and Hutchins, N. (2013). Estimating wall-shear-stress fluctuations given an outer region input. *Journal of Fluid Mechanics*, 715:163–180.

McKeon, B., Jacobi, I., and Duvvuri, S. (2018). Dynamic roughness for manipulation and control of turbulent boundary layers: An overview. *AIAA Journal*, 56(6):2178–2193.

McKeon, B. J. (2017). The engine behind (wall) turbulence: perspectives on scale interactions. *Journal of Fluid Mechanics*, 817:P1.

Meinhart, C. and Adrian, R. (1995). On the existence of uniform momentum zones in a turbulent boundary layer. *Physics of Fluids*, 7(4):694–696.

Metzger, M. M. and Klewicki, J. C. (2001). A comparative study of near-wall turbulence in high and low reynolds number boundary layers. *Physics of Fluids*, 13(3):692–701.

Monty, J. P., Hutchins, N., Ng, H. C. H., Marusic, I., and Chong, M. S. (2009). A comparison of turbulent pipe, channel and boundary layer flows. *Journal of Fluid Mechanics*, 632:431–442.

Monty, J. P., Stewart, J. A., Williams, R. C., and Chong, M. S. (2007). Large-scale features in turbulent pipe and channel flows. *Journal of Fluid Mechanics*, 589:147–156.

Naqavi, I. Z., Tyacke, J. C., and Tucker, P. G. (2018). Direct numerical simulation of a wall jet: flow physics. *Journal of Fluid Mechanics*, 852:507–542.

Naseem, U., Sven, O., Bernhard, W., and Bassam, A. (2009). Large-eddy simulations and heat-flux modeling in a turbulent impinging jet. *Numerical Heat Transfer, Part A: Applications*, 55(10):906–930.

Nugroho, B., Hutchins, N., and Monty, J. P. (2013). Large-scale spanwise periodicity in a turbulent boundary layer induced by highly ordered and directional surface roughness. *International Journal of Heat and Fluid Flow*, 41:90–102.

Örlü, R. and Schlatter, P. (2013). Comparison of experiments and simulations for zero pressure gradient turbulent boundary layers at moderate reynolds numbers. *Experiments in Fluids*, 54(6):1547.

Panton, R. L. (2001). Overview of the self-sustaining mechanisms of wall turbulence. *Progress in Aerospace Sciences*, 37(4):341–383.

Rao, K. N., Narasimha, R., and Narayanan, M. A. B. (1971). The 'bursting' phenomenon in a turbulent boundary layer. *Journal of Fluid Mechanics*, 48(2):339–352.

Rauleder, J. and Leishman, J. G. (2014). Particle–fluid interactions in rotor-generated vortex flows. *Experiments in Fluids*, 55(3):1689.

Robinson, S. K., Kline, S. J., and Spalart, P. (1989). A review of quasi-coherent structures in a numerically simulated turbulent boundary layer. Dubrovnik, Yugoslavia. NASA.

Rostamy, N., Bergstrom, D. J., Sumner, D., and Bugg, J. D. (2011a). The effect of surface roughness on the turbulence structure of a plane wall jet. *Physics of Fluids*, 23(8):085103.

Rostamy, N., Bergstrom, D. J., Sumner, D., and Bugg, J. D. (2011b). An experimental study of a turbulent wall jet on smooth and transitionally rough surfaces. *Journal of Fluids Engineering*, 133(11):111207.

Samie, M., Marusic, I., Hutchins, N., Fu, M. K., Fan, Y., Hultmark, M., and Smits, A. J. (2018). Fully resolved measurements of turbulent boundary layer flows up to Re_τ= 20,000. *Journal of Fluid Mechanics*, 851:391–415.

Schober, M. and Fernholz, H.-H. (2000). Turbulence control in wall jets. *European Journal of Mechanics-B/Fluids*, 19(4):503–528.

Schoppa, W. (1997). Genesis and dynamics of coherent structures in near-wall turbulence. *Self-Sustaining Mechanisms of Wall Turbulence*.

Schoppa, W. and Hussain, F. (2002). Coherent structure generation in near-wall turbulence. *Journal of Fluid Mechanics*, 453:57–108.

Sharp, N. S., Neuscamman, S., and Warhaft, Z. (2009). Effects of large-scale free stream turbulence on a turbulent boundary layer. *Physics of Fluids*, 21(9):095105.

Sillero, J. A., Jiménez, J., and Moser, R. (2013). One-point statistics for turbulent wall-bounded flows at reynolds numbers up to $\delta^+ \approx 2000$. *Physics of Fluids*, 25(10):105102.

Smith, B. S. (2008). *Wall jet boundary layer flows over smooth and rough surfaces*. PhD thesis, Virginia Tech.

Smits, A. J., McKeon, B. J., and Marusic, I. (2011). High–reynolds number wall turbulence. *Annual Review of Fluid Mechanics*, 43(1):353–375.

Stenzel, V., Wilke, Y., and Hage, W. (2011). Drag-reducing paints for the reduction of fuel consumption in aviation and shipping. *Progress in Organic Coatings*, 70(4):224–229.

Tachie, M., Balachandar, R., and Bergstrom, D. (2002). Scaling the inner region of turbulent plane wall jets. *Experiments in Fluids*, 33(2):351–354.

Tachie, M. F., Balachandar, R., and Bergstrom, D. J. (2004). Roughness effects on turbulent plane wall jets in an open channel. *Experiments in Fluids*, 37(2):281–292.

Tailland, A. (1967). Jet parietal. *J. Mecanique*, 6:103–131.

Talluru, M. K. (2014). *Manipulating large-scale structures in a turbulent boundary layer using a wall-normal jet*. PhD thesis, Department of Mechanical Engineering, University of Melbourne, Australia.

Tomkins, C. D. and Adrian, R. J. (2003). Spanwise structure and scale growth in turbulent boundary layers. *Journal of Fluid Mechanics*, 490:37–74.

Vallikivi, M., Ganapathisubramani, B., and Smits, A. J. (2015). Spectral scaling in boundary layers and pipes at very high reynolds numbers. *Journal of Fluid Mechanics*, 771:303–326.

Waleffe, F. (2001). Exact coherent structures in channel flow. *Journal of Fluid Mechanics*, 435:93–102.

Waleffe, F. and Kim, J. (1998). How streamwise rolls and streaks self-sustain in a shear flow. ii. In *29th AIAA, Fluid Dynamics Conference*, page 2997. American Institute of Aeronautics and Astronautics.

Wallace, J. M., Eckelmann, H., and Brodkey, R. S. (1972). The wall region in turbulent shear flow. *Journal of Fluid Mechanics*, 54(1):39–48.

Wilkinson, S. P. (1990). Interactive wall turbulence control. *Viscous Drag Reduction in Boundary Layers*, 123:0–930403.

Wygnanski, I., Katz, Y., and Horev, E. (1992). On the applicability of various scaling laws to the turbulent wall jet. *Journal of Fluid Mechanics*, 234:669–690.

Zhou, J., Adrian, R. J., Balachandar, S., and Kendall, T. M. (1999). Mechanisms for generating coherent packets of hairpin vortices in channel flow. *Journal of Fluid Mechanics*, 387:353–396.

Zhou, M. D., Heine, C., and Wygnanski, I. (1996). The effects of excitation on the coherent and random motion in a plane wall jet. *Journal of Fluid Mechanics*, 310:1–37.

A. Appendix A

This chapter discusses specifics of the calibration jet used for calibration of the hot-wire sensors. Figure A.1 shows a schematic of the calibration jet used for the current measurements. The jet settling chamber diameter was 4.5 inch. The jet exit nozzle diameter was 0.2 inch. The jet was powered using pressurized air. The exit velocity was controlled using a manual valve. A four inch long honeycomb and a series of screens and cloths were used to ensure the turbulence intensity was below 1%. The jet exit velocity was calculated across the nozzle contraction using

$$A_1 V_1 = A_2 V_2, \tag{A.1}$$

and Bernoulli's equation

$$p_1 + \frac{1}{2}\rho V_1^2 = p_2 + \frac{1}{2}\rho V_2^2. \tag{A.2}$$

Here, A is cross-section area, V is velocity, p is static pressure and ρ is density (constant in current work). The subscript 1 and 2 represents before and after the nozzle contraction. respectively. Using equation A.1 and A.2, the velocity at the jet exit can be determined as,

$$V_2 = \frac{A_1/A_2}{\sqrt{A_1^2/A_2^2 - 1}} \sqrt{\frac{2(p_1 - p_2)}{\rho}}. \tag{A.3}$$

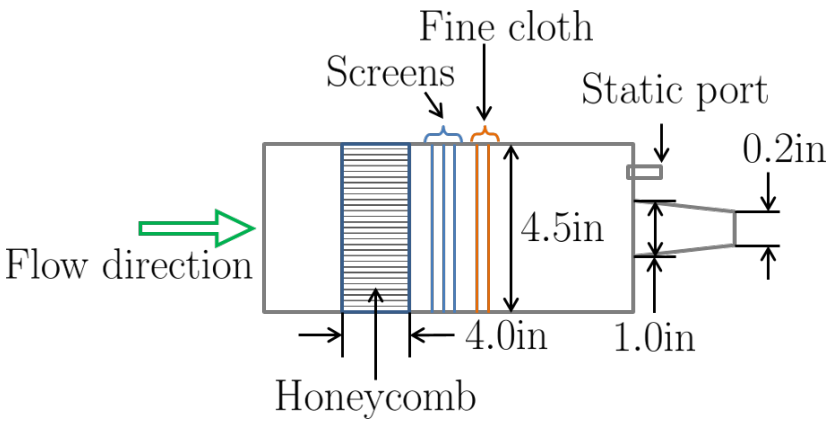

Figure A.1. Schematic of the jet used for the calibrations of the hot-wire sensors.

Calibrations were carried out before and after each run by aligning the centerline of the calibration jet with the centerline of the PWJ. Figure A.2 shows the turbulence intensity at jet exit. Figure A.3 shows a typical calibration before and after a run.

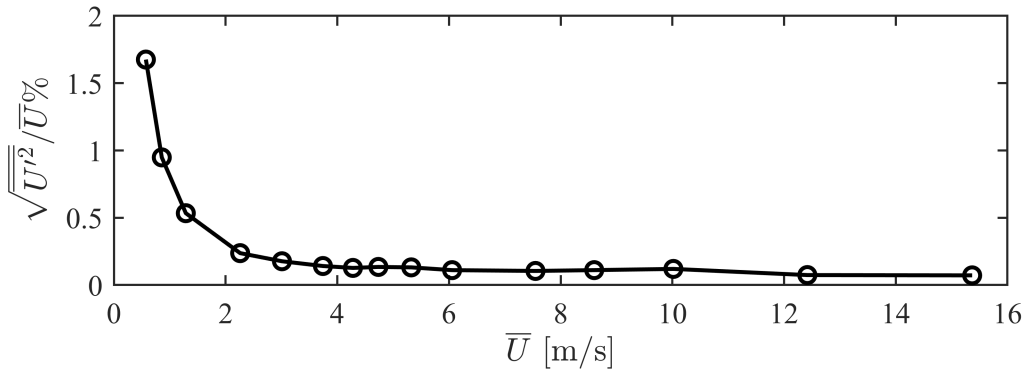

Figure A.2. Turbulence intensity at calibration jet exit.

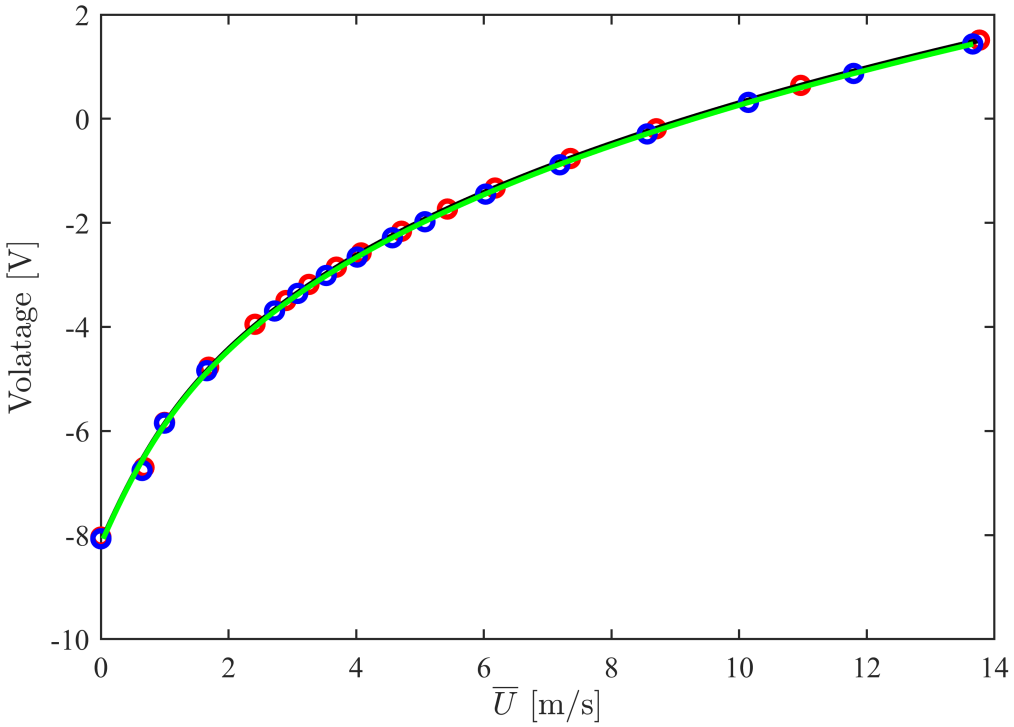

Figure A.3. Typical calibration before and after a run. The symbols ○ and ○ represent calibration velocity for before and after a run respectively and the lines —— and —— represent the corresponding third order polynomial.

B. Appendix B

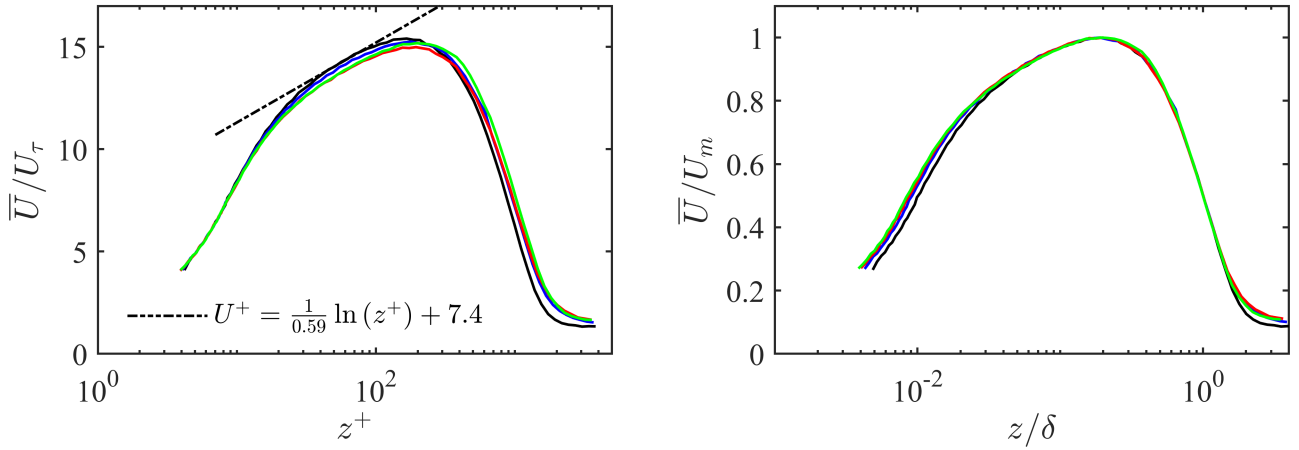

Figure B.1. Scaling of the streamwise velocity in wall-normal logarithmic coordinates for x/b = 50 with respect to the inner (left) and the outer (right) variables. The lines correspond to the unforced flow (——), Case A (——), Case B (——) and Case C (——) conditions respectively.

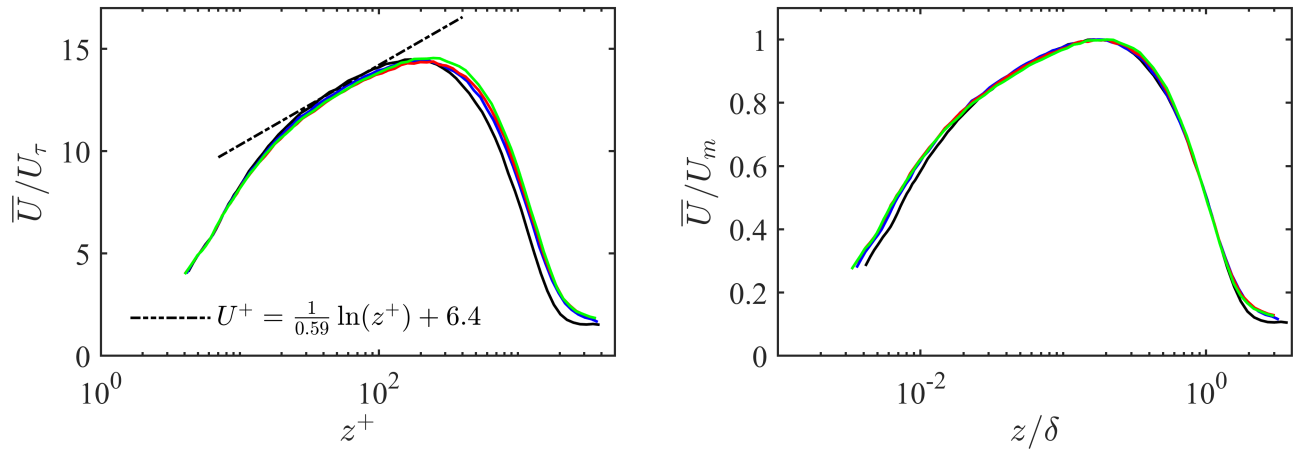

Figure B.2. Scaling of the streamwise velocity in wall-normal logarithmic coordinates for x/b = 75 with respect to the inner (left) and the outer (right) variables. The lines correspond to the unforced flow (——), Case A (——), Case B (——) and Case C (——) conditions respectively.

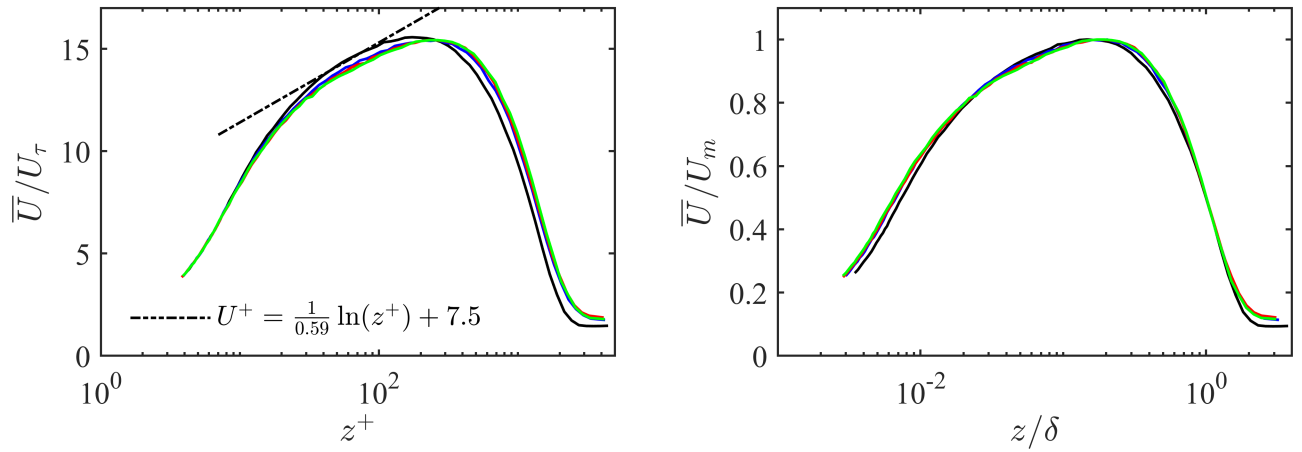

Figure B.3. Scaling of the streamwise velocity in wall-normal logarithmic coordinates for x/b = 110 with respect to the inner (left) and the outer (right) variables. The lines correspond to the unforced flow (——), Case A (——), Case B (——) and Case C (——) conditions respectively.

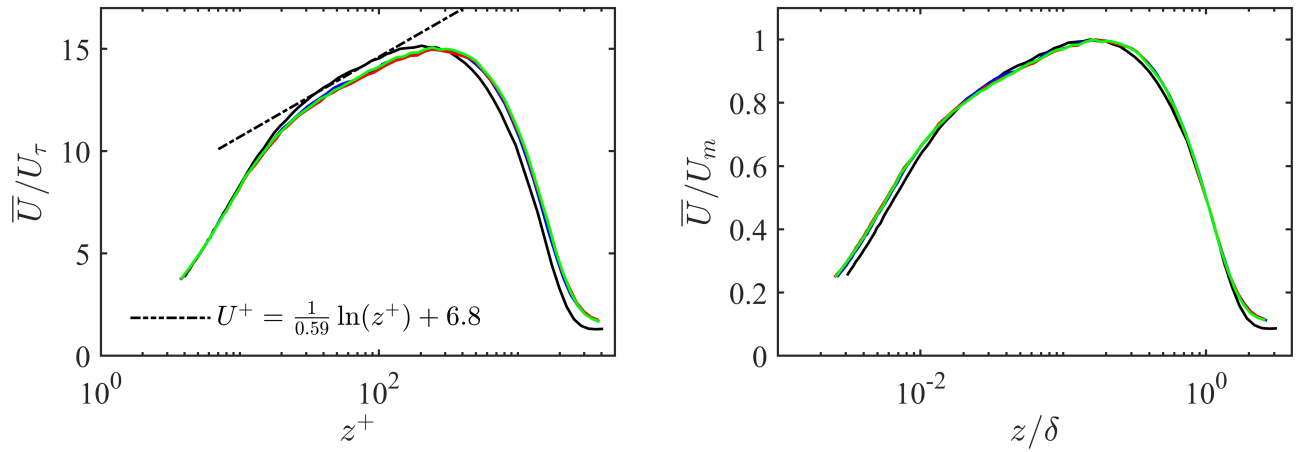

Figure B.4. Scaling of the streamwise velocity in wall-normal logarithmic coordinates for x/b = 137 with respect to the inner (left) and the outer (right) variables. The lines correspond to the unforced flow (——), Case A (——), Case B (——) and Case C (——) conditions respectively.

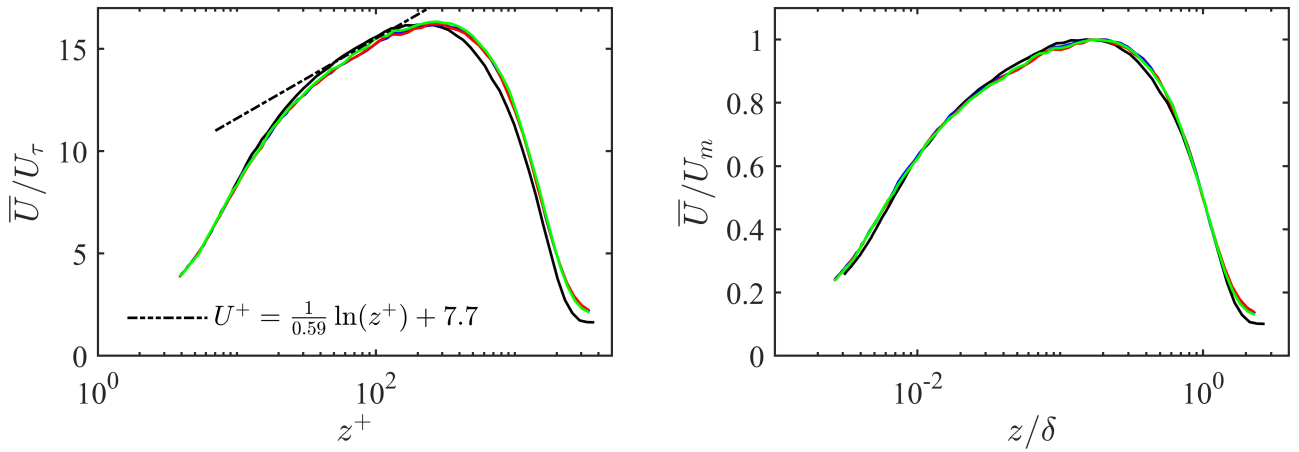

Figure B.5. Scaling of the streamwise velocity in wall-normal logarithmic coordinates for x/b = 162 with respect to the inner (left) and the outer (right) variables. The lines correspond to the unforced flow (——), Case A (——), Case B (——) and Case C (——) conditions respectively.

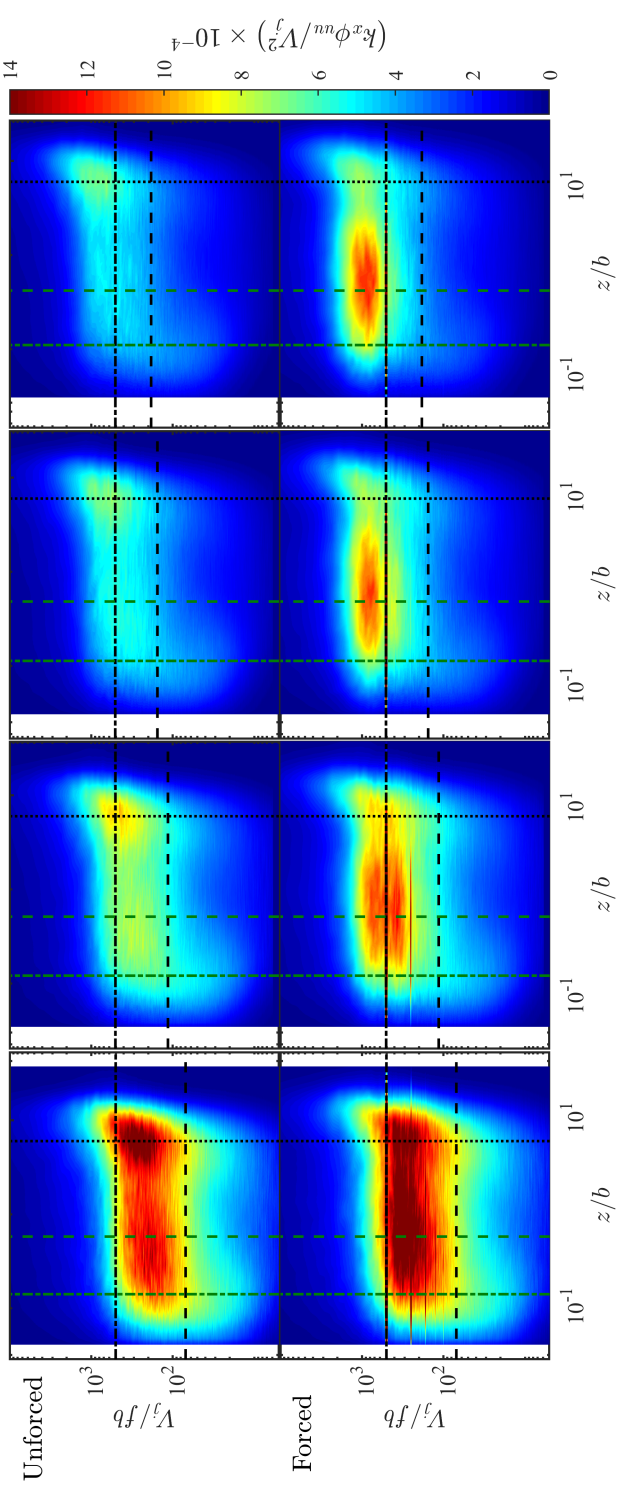

Figure B.6. Comparison of contour maps of the stream-wise pre-multiplied energy spectra $k_x\phi_{uu}/V_j^2$ for the unforced (top) and Case A (bottom) conditions. The streamwise distance increases moving from left to right. The vertical lines show the wall-normal locations $z^+ \approx 15$ (-·-·-), $z^+ \approx 60$ (- - - -) and $z \approx 0.6\delta^0$ (.....) respectively. The horizontal lines show the cut-off wavelength $\lambda_c = 2\delta^0$ (-----) and the forcing wavelength $\lambda_j/b \approx 500$ for Case B (-----) respectively.

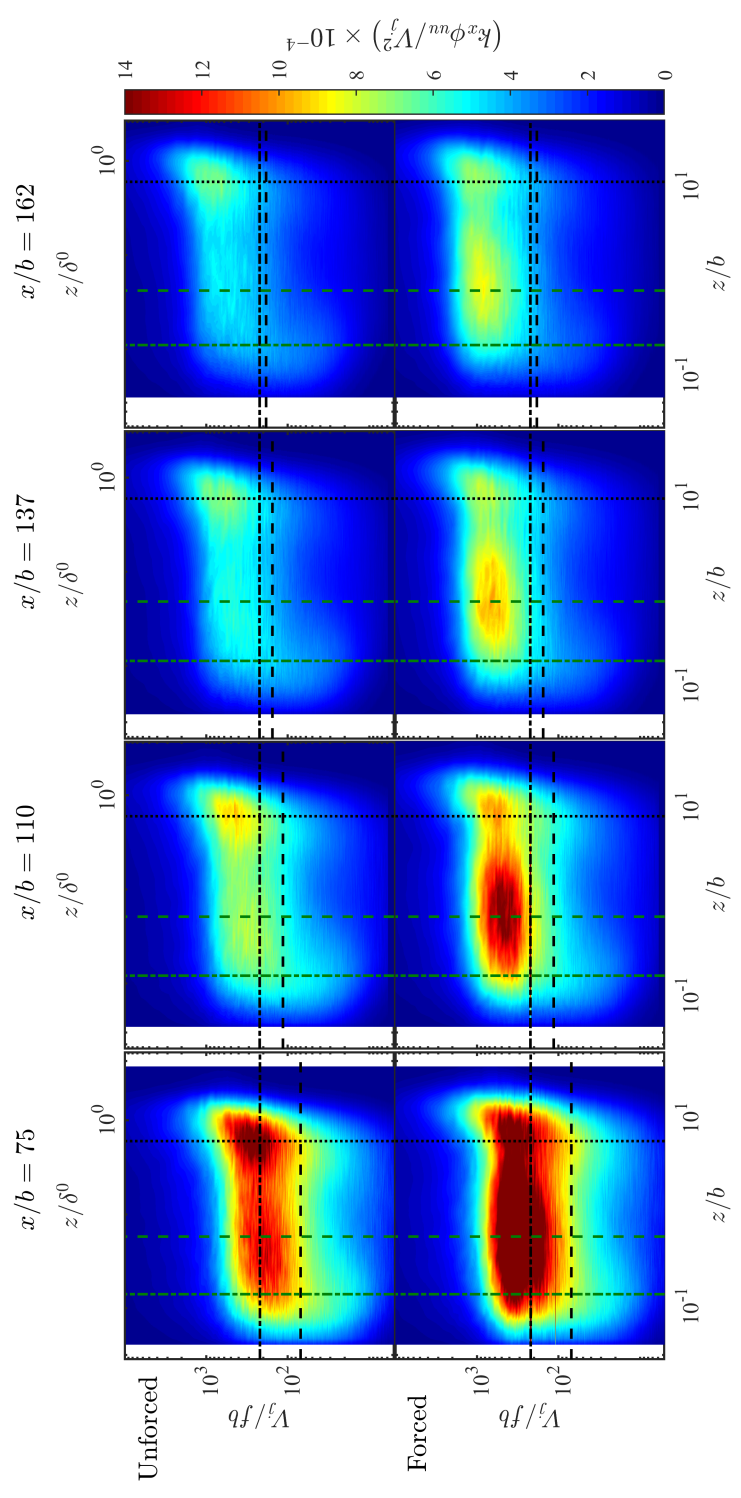

Figure B.7. Comparison of contour maps of the stream-wise pre-multiplied energy spectra $k_x\phi_{uu}/V_j^2$ for the unforced (top) and Case B (bottom) conditions. The streamwise distance increases moving from left to right. The vertical lines show the wall-normal locations $z^+ \approx 15$ (-·-·-), $z^+ \approx 60$ (- - - -) and $z \approx 0.6\delta^0$ (.....) respectively. The horizontal lines show the cut-off wavelength $\lambda_c = 2\delta^0$ (-----) and the forcing wavelength $\lambda_j/b \approx 295$ for Case B (-----) respectively.

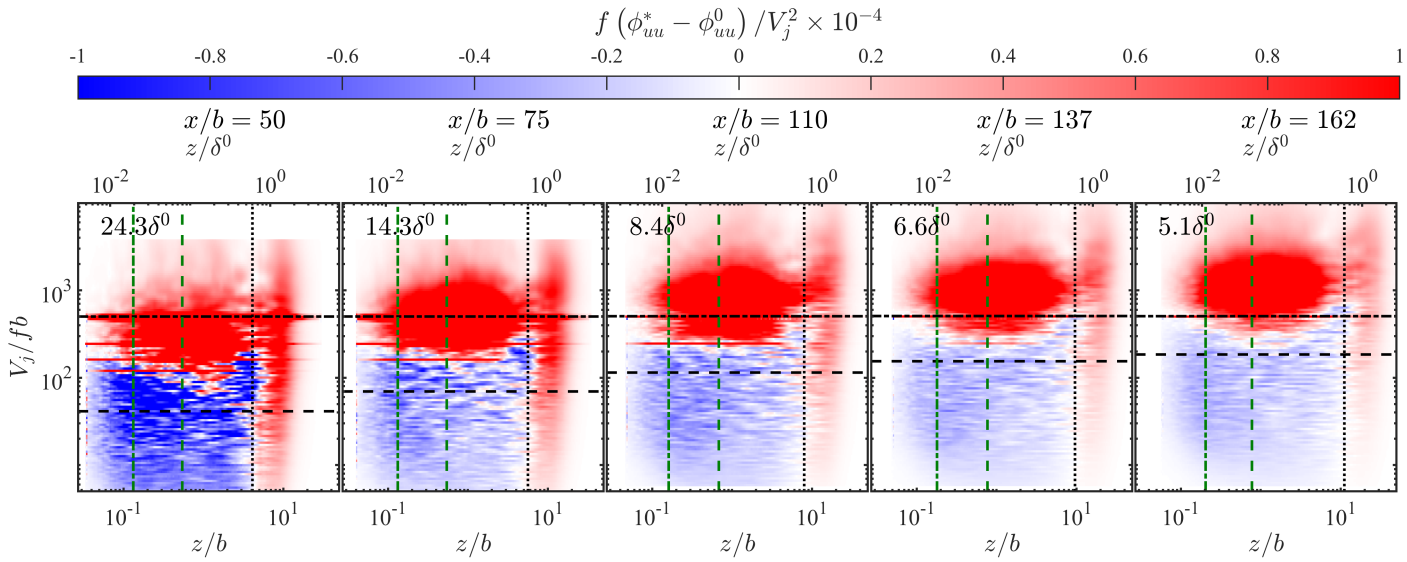

Figure B.8. Change in pre-multiplied energy spectra ($f\left(\phi^*_{uu}-\phi^0_{uu}\right)/V_j^2$) for Case A ($\lambda_j/b\approx500$) as the flow develops downstream. The vertical lines show the wall-normal locations $z^+\approx15$ (—·—·), $z^+\approx60$ (- - - -) and $z\approx0.6\delta^0$ (·····) respectively. The cut-off wavelength $\lambda_c=2\delta^0$ (- - - -) and the forcing wavelength $\lambda_j/b\approx500$ for Case A (-----) are also shown. The number on the top left corner indicates corresponding forcing wavelength non-dimensionalized with respect to the outer unforced variables (λ_x^f) at each streamwise location.

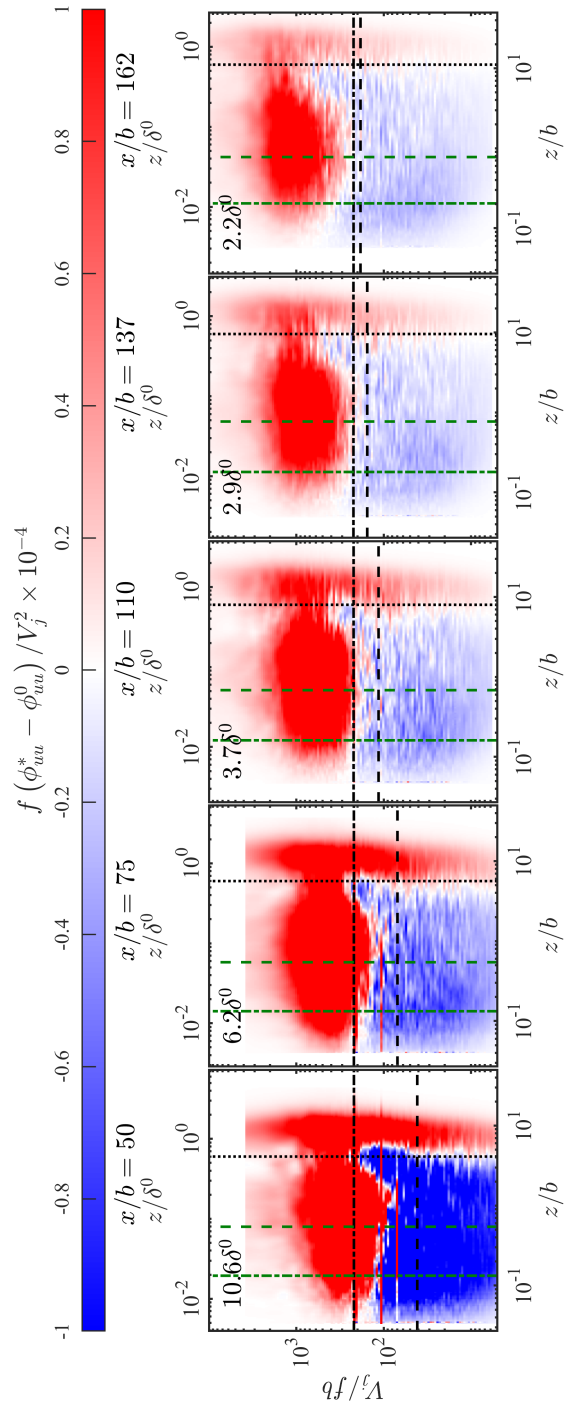

Figure B.9. Change in pre-multiplied energy spectra ($f\left(\phi^*_{uu}-\phi^0_{uu}\right)/V_j^2$) for Case C ($\lambda_j/b \approx 220$) as the flow develops downstream. The vertical lines show the wall-normal locations $z^+ \approx 15$ (—·—·), $z^+ \approx 60$ (- - -) and $z \approx 0.6\delta^0$ (·····) respectively. The cut-off wavelength $\lambda_c = 2\delta^0$ (- - -) and the forcing wavelength $\lambda_j/b \approx 220$ for Case C (———) are also shown. The number on the top left corner indicates corresponding forcing wavelength non-dimensionalized with respect to the outer unforced variables (λ_x^f) at each streamwise location.

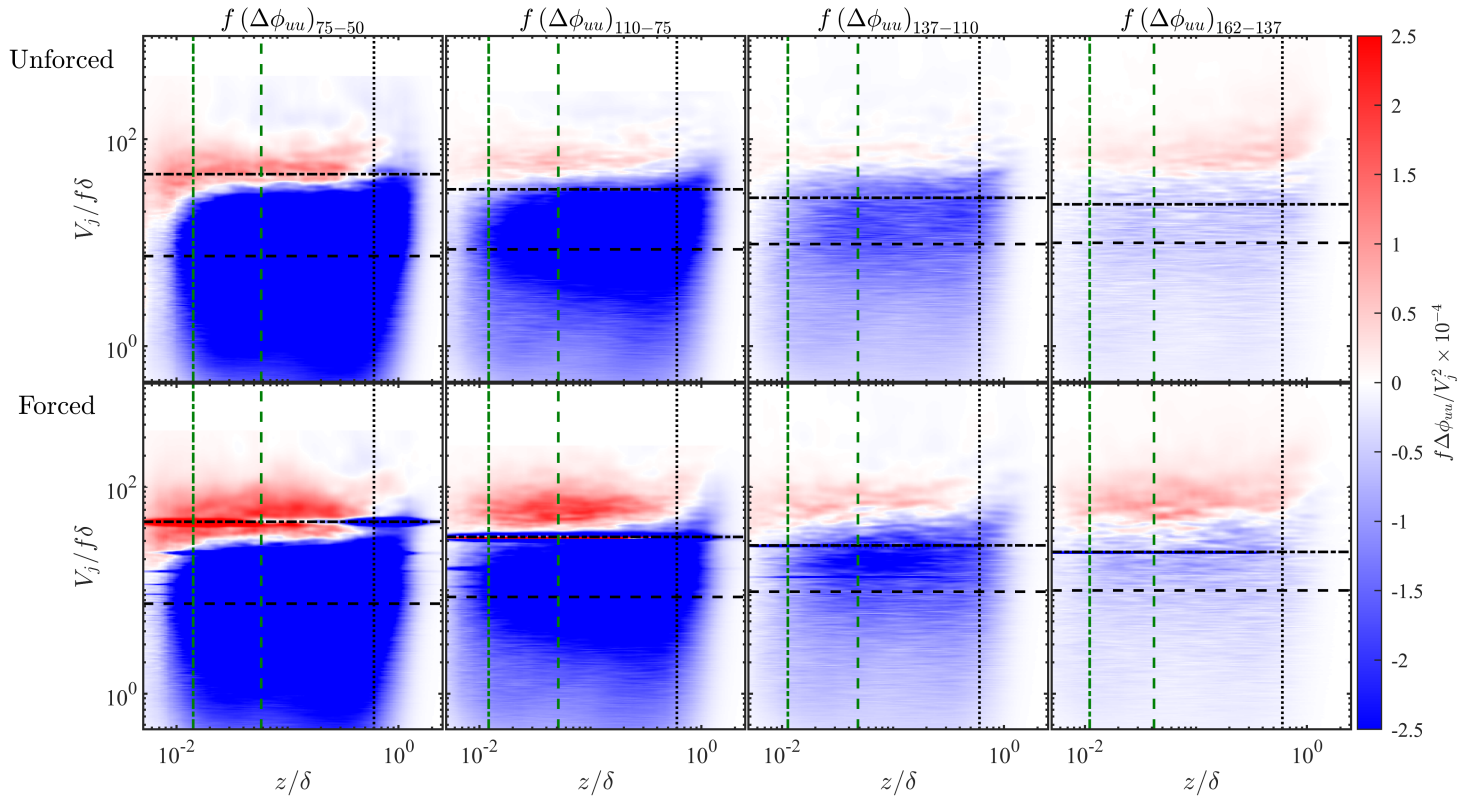

Figure B.10. Difference of the pre-multiplied energy spectra between a streamwise location (n) and the immediate upstream location ($n-1$). Here, n represents n^{th} streamwise location where $n = 1 \implies x/b = 75$. The top figures represent unforced flow and the bottom figures represent forced flow for Case A conditions. The vertical lines show the wall-normal locations $z^+ \approx 15$ (—·—), $z^+ \approx 60$ (- - - -) and $z \approx 0.6\delta^0$ (·····) respectively at the n^{th} location. The cut-off wavelength $\lambda_c = 2\delta^0$ (- - - -) and the forcing wavelength $\lambda_j/b \approx 500$ for Case A (-----) non-dimensionalized with respect to the outer length scale δ are also shown.

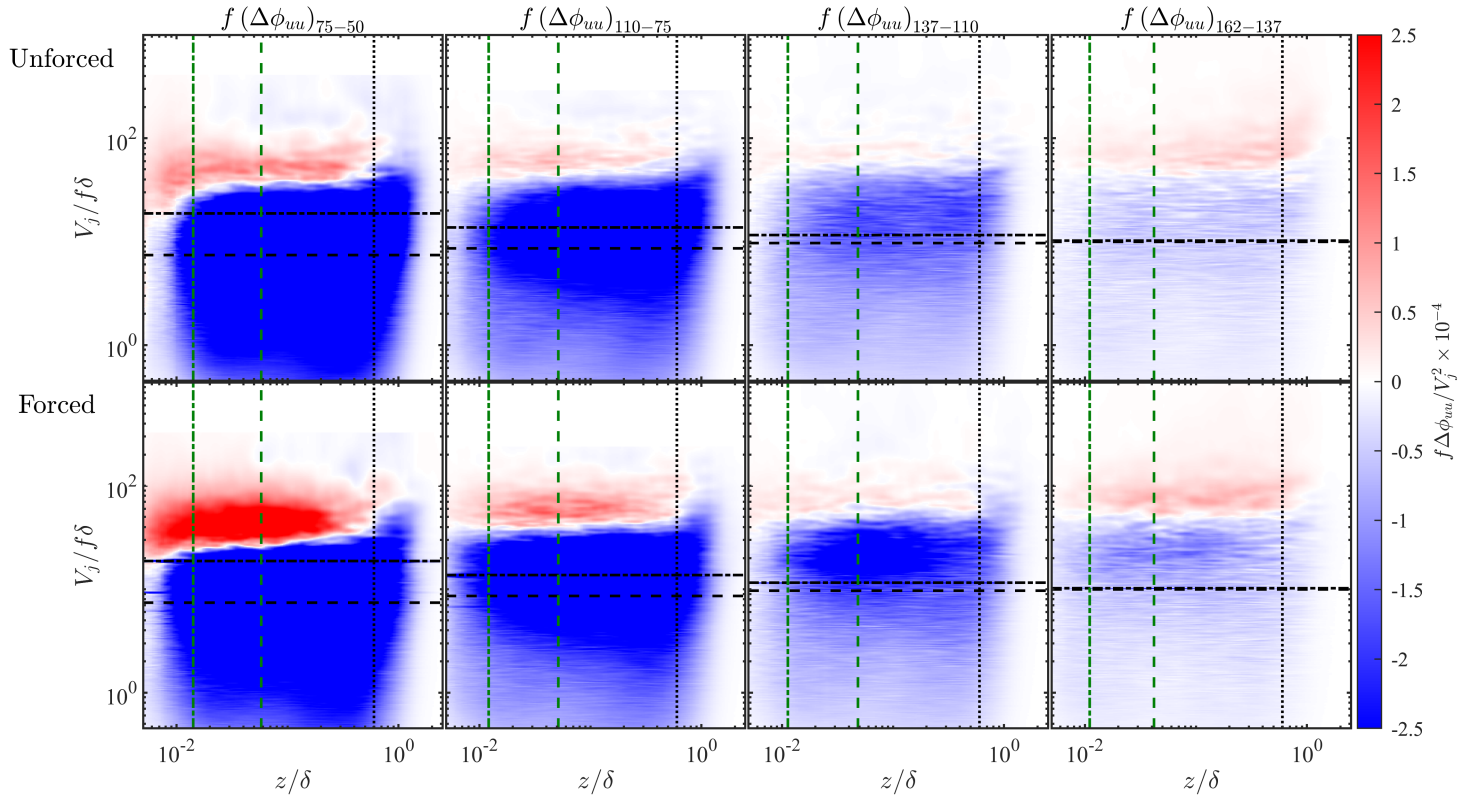

Figure B.11. Difference of the pre-multiplied energy spectra between a streamwise location (n) and the immediate upstream location ($n-1$). Here, n represents n^{th} streamwise location where $n = 1 \implies x/b = 75$. The top figures represent unforced flow and the bottom figures represent forced flow for Case C conditions. The vertical lines show the wall-normal locations $z^+ \approx 15$ (—·—·), $z^+ \approx 60$ (- - - -) and $z \approx 0.6\delta^0$ (·····) respectively at the n^{th} location. The cut-off wavelength $\lambda_c = 2\delta^0$ (- - - -) and the forcing wavelength $\lambda_j/b \approx 220$ for Case C (-----) non-dimensionalized with respect to the outer length scale δ are also shown.

C. Appendix C

This chapter provides the details of the parametric study conducted to ensure constant energy at PWJ exit upon forcing. The energy of the forced flow at the PWJ exit was assumed to be a 2^{nd} order polynomial of the forcing frequency f_f and a 3^{rd} order polynomial of the forcing amplitude V. The relation between the energy, frequency and amplitude was assumed to be,

$$En = A_1 f_f^2 + A_2 f_f + A_3 V^3 + A_4 V^2 + A_5 V + A_6 V f_f + A_7 \tag{C.1}$$

Rewriting the equation in the matrix form yields,

$$\begin{bmatrix} En \end{bmatrix} = \begin{bmatrix} f^2 \\ f \\ V^3 \\ V^2 \\ V \\ Vf \\ 1 \end{bmatrix} \begin{bmatrix} A_1 \\ A_2 \\ A_3 \\ A_4 \\ A_5 \\ A_6 \\ A_7 \end{bmatrix}$$

$$\begin{bmatrix} En \end{bmatrix} = \begin{bmatrix} Vfs \end{bmatrix} \begin{bmatrix} As \end{bmatrix}$$

Multiplying both sides with $[Vfs]'$ yields,

$$\begin{bmatrix} Vfs \end{bmatrix}' \begin{bmatrix} En \end{bmatrix} = \begin{bmatrix} Vfs \end{bmatrix}' \begin{bmatrix} Vfs \end{bmatrix} \begin{bmatrix} As \end{bmatrix}$$

Rearranging the sides to obtain the values of $[As]$ leads to,

$$[\ As\ ] = \left([\ Vfs\ ]'[\ Vfs\ ]^{-1}\right)[\ Vfs\ ]'[\ En\ ] \tag{C.2}$$

Equation C.2 was solved using the experimental values from the parametric study to obtain $[As]$ coefficients. These coefficients were then used in equation C.1 to obtain corresponding voltage values for 1–20 Hz frequencies and constant energy. For the purpose of current work, this value was chosen to be $\sim 8.78. \times 10^{8}$ $\mathrm{Jkg^{-1}}$.

D. Appendix D

The current measurements used a 60 grit sandpaper at the PWJ exit to trip the flow. The sandpaper was used to ensure that the inner viscous shear-layer transitions to turbulence without the influence of the acoustic forcing. A comparison of the energy spectra of the PWJ before and after the sandpaper installation is shown in Figure D.1. Here the comparison is shown between streamwise locations with similar local Reynolds number,

$$Re_m = \frac{\delta U_m}{\nu} \approx 2.1 \times 10^4. \tag{D.1}$$

For the flow without sandpaper, the PWJ achieves this Reynolds number at x/b = 137. Whereas, with sandpaper, the PWJ reaches this Reynolds number at x/b = 150. The figure also compares the pre-multiplied energy spectra at three wall-normal locations ($z^+ \approx 15$, 60 and $z \approx 0.6\delta$). It is noted that for this comparison, only the unforced quantities are considered. As seen in this figure, the PWJ exhibits no significant change in energy upon the sandpaper installation.

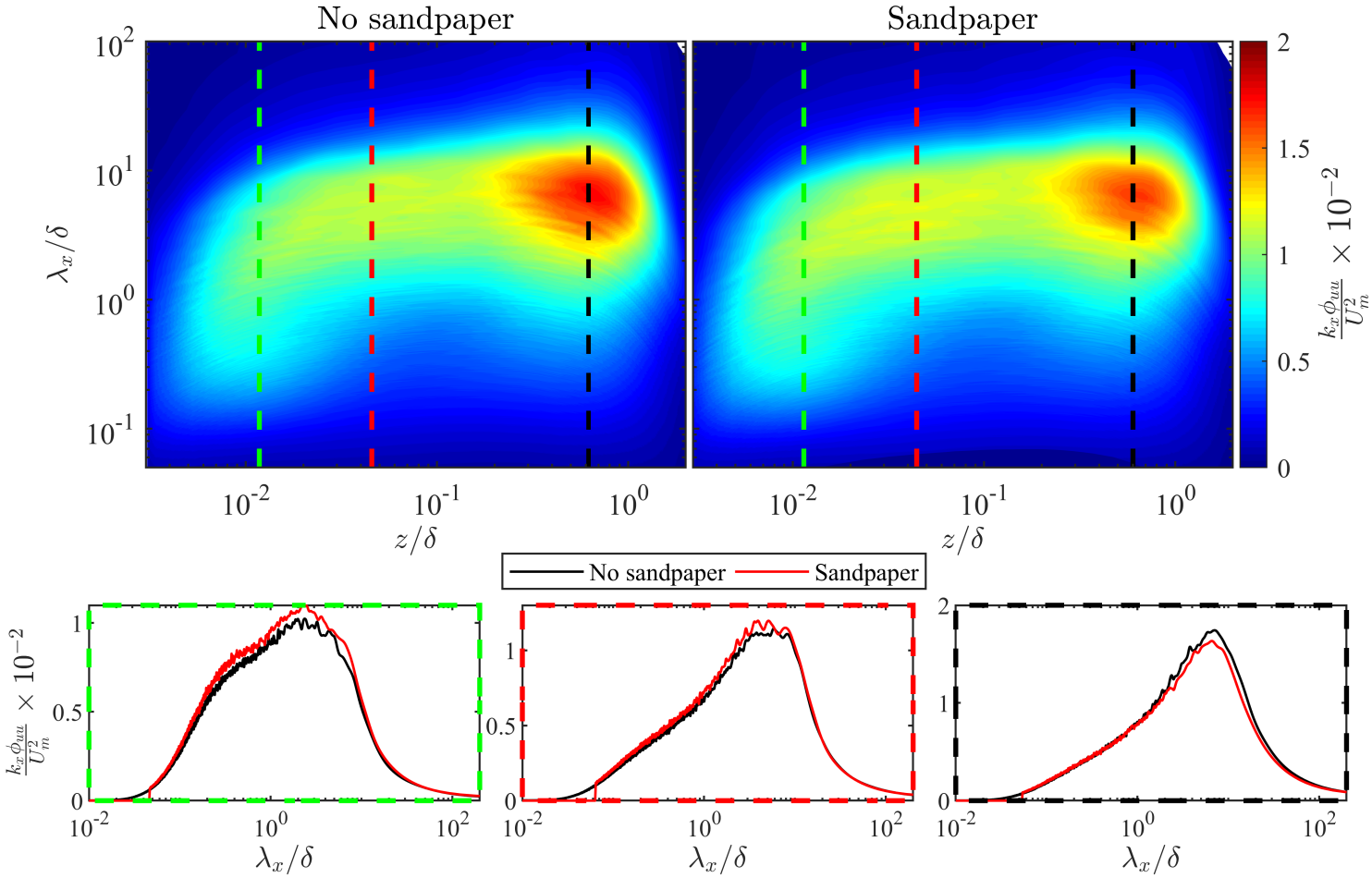

Figure D.1. Comparison of the pre-multiplied energy spectra of the PWJ before and after the installation of the sandpaper. Here, Re_m = 20943 and 21005 for the No-sandpaper and Sandpaper cases respectively. Top figures compares the contour plots where the vertical lines in the contour plot shows wall-normal locations $z^+ \approx 15$ (- - - -), 60 (- - - -) and $z \approx 0.6\delta$ (- - - -). Bottom figures show comparison of the spectra at these wall-normal locations.

E. Appendix E

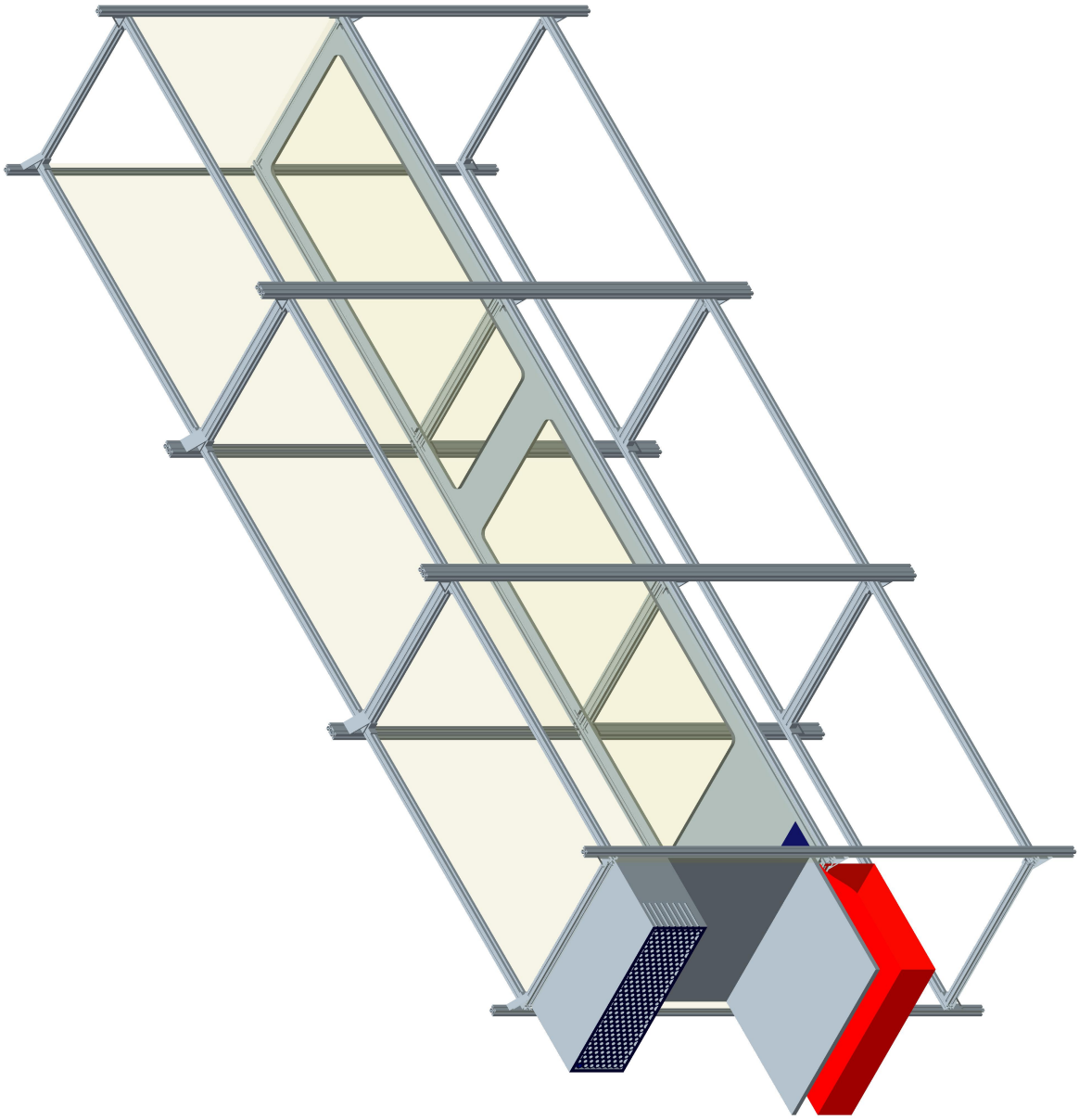
SCALE 0.050

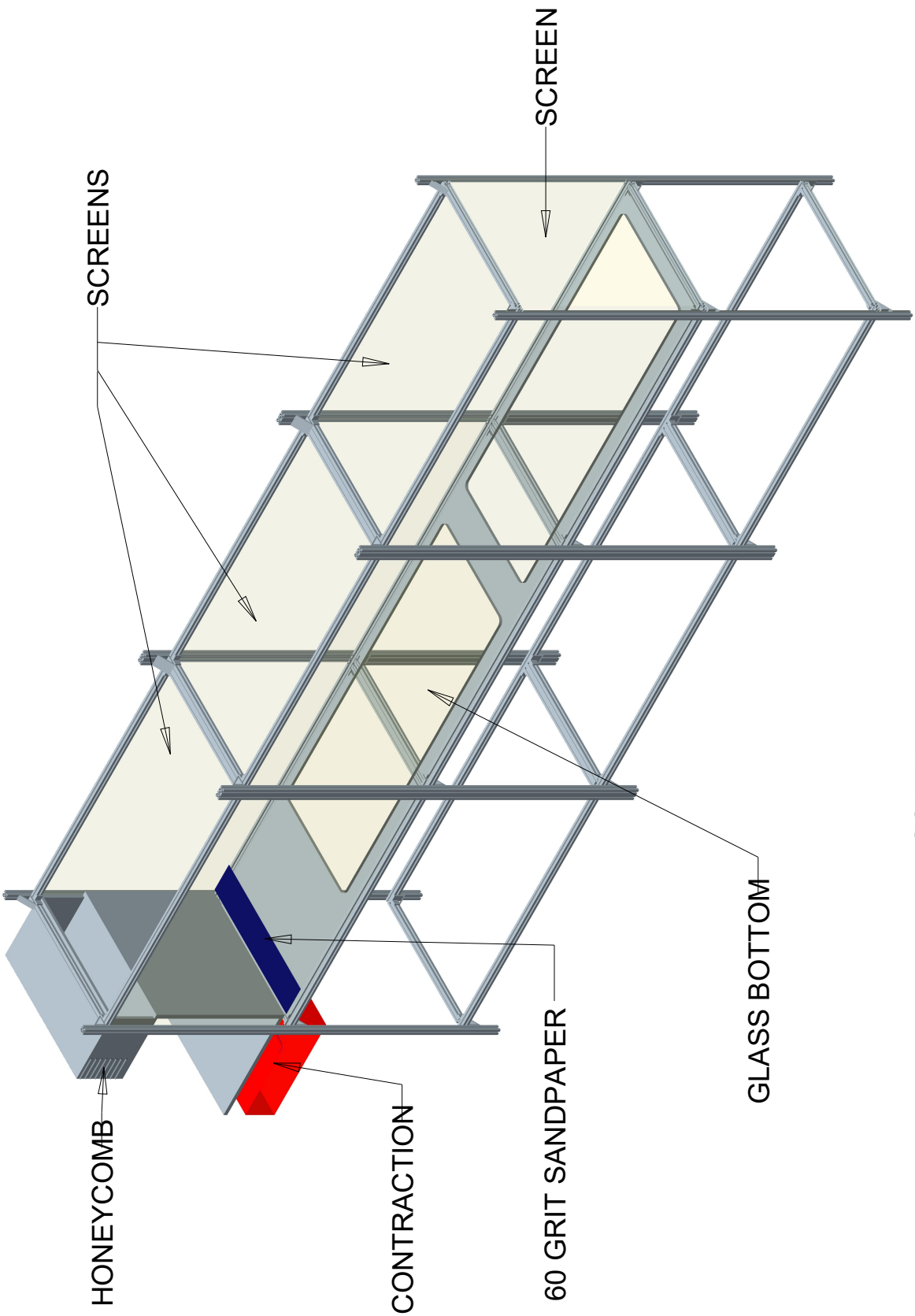
SCREEN
SCREENS
HONEYCOMB
CONTRACTION
60 GRIT SANDPAPER
GLASS BOTTOM
SCALE 0.050

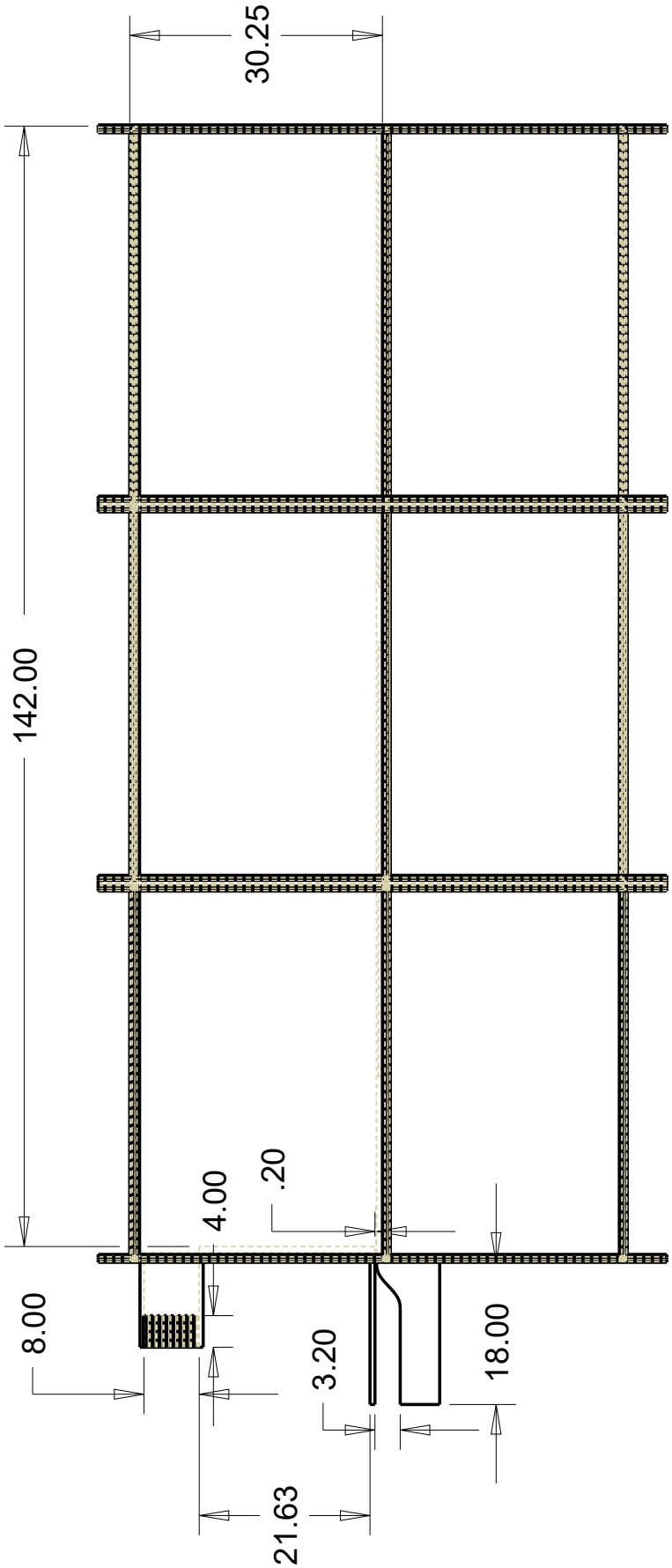
30.25
142.00
4.00
.20
8.00
3.20
18.00
21.63
SCALE 0.050
ALL DIMENSIONS ARE IN INCHES

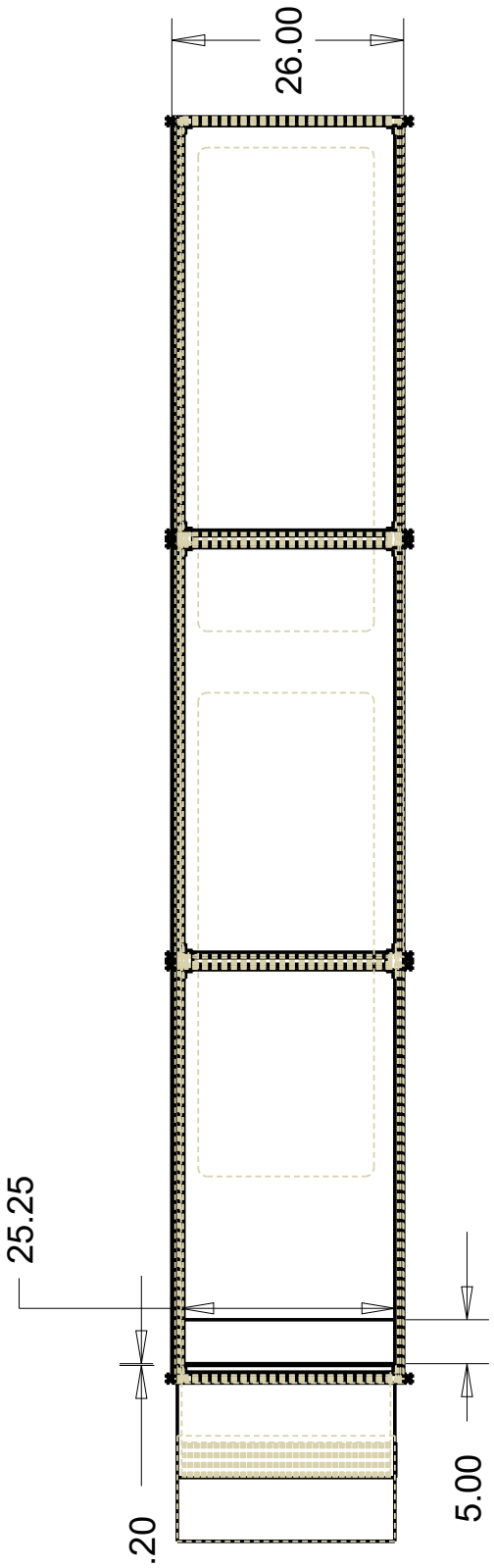

SCALE 0.050

ALL DIMENSIONS ARE IN INCHES